Electronic Supplementary Material (ESI) for Physical Chemistry Chemical Physics.
This journal is © the Owner Societies 2015

Electronic Supplementary Information (ESI) to accompany:

Separation of Benzene from Mixtures with Water, Methanol, Ethanol, and Acetone: Highlighting Hydrogen Bonding and Molecular Clustering Influences in CuBTC

Juan José Gutiérrez-Sevillano,[†] Sofia Calero,[†] and Rajamani Krishna[‡]

[†]Department of Physical, Chemical and Natural Systems

University Pablo de Olavide

Ctra. Utrera km. 1, 41013 Sevilla, Spain

[‡] Van 't Hoff Institute for Molecular Sciences, University of Amsterdam, Science Park 904,

1098 XH Amsterdam, The Netherlands

Table of Contents

1. Preamble

This ESI accompanying our manuscript *Separation of Benzene from Mixtures with Water, Methanol, Ethanol, and Acetone: Highlighting Hydrogen Bonding and Molecular Clustering Influences in CuBTC* provides (a) structural details of CuBTC, (b) Configurational-Bias Monte Carlo (CBMC) and Molecular Dynamics (MD) simulation methodologies with specification of force fields, (c) snapshots showing the location of adsorbed molecules within CuBTC framework, (d) 2-site and 3-site Langmuir-Freundlich fit parameters for unary isotherms, (e) data on radial distribution functions (RDF) to confirm H-bonding effects, (f) details of the methodology used to calculate activity coefficients from CBMC mixture simulations, and (g) details of IAST and RAST calculation procedures.

For ease of reading, this ESI is written as a stand-alone document. As a consequence, there is some overlap of material with the main manuscript. Researchers who are interested in specific sections can use the Table of Contents to skip to that specific section, without the need to wade through the entire material that is presented here.

2. CBMC simulation methodology

The CuBTC (= $Cu_3(BTC)_2$ with BTC = 1,3,5-benzenetricarboxylate, also known as HKUST-1) framework is composed of copper atoms connected by benzene-1,3,5-tricarboxylate (BTC) linkers, which form a characteristic paddle-wheel structure: two copper atoms bonded to the oxygen atoms of four BTC linkers, generating four-connected square-planar vertexes; see Figure 1. The framework contains two types of large cavities (9 Å diameter) and small cavities (of 5 Å diameter). The larger cavities (L_2 and L_3) are similar in size and shape but as a result of the paddle-wheel, the copper atoms are only accessible from the L_3 cages. L_2 and L_3 cavities are connected through triangular-shaped windows. The small cavities (T_1) are tetrahedral pockets enclosed by the benzene rings; these are connected to L_3 cages by small triangular windows (3.5 Å in size), as shown in Figure 2.

Benzene is modeled using the full atom rigid model proposed by Rai and Siepmann.[1] In this model carbon and hydrogen atoms are considered as single Lennard-Jones interaction centers with partial charges.

Water is modeled using TIP5P-E[2] which has proven to be the most suitable model for water in Cu-BTC.[3] Furthermore, recently, Peng *et al*.[4] have found that at least a four sites model is needed to reproduce the right orientation of the water molecules in metal organic frameworks containing open metal sites.

Methanol, ethanol, and acetone molecules are modeled using TraPPE.[5, 6]

The Cu-BTC framework is modeled as a rigid structure based on the crystal structure of Chui *et al*.[7] with the atoms fixed in their crystallographic position. We removed the axial oxygen atoms weakly bonded to the copper atoms that correspond to water ligands. Lennard Jones parameters for the atoms were taken from DREIDING[8] force field except these for copper atoms that were taken from UFF[9] force field; see Table 1. Additionally partial charges from Castillo *et al*.[3] were added to the model. The unit cell of our model is a cubic cell of $a = b = c = 26.34$ Å. The computed helium void fraction is of 0.76, the pore volume 0.85 cm^3/g and the surface area 2100 m^2/g. The framework density, $\rho = 879$ kg m^{-3}.

Monte Carlo (MC) simulations were performed in the Grand Canonical (GC) Ensemble and Configurational Bias Monte Carlo (CBMC) technique was used for the insertion and deletion of molecules in and from the system. We used Lennard-Jones and electrostatic cutoffs of 12.0 Å. Coulombic interactions were computed using the Ewald summation technique with a relative precision of 10^{-6} and using the same cut-off.

All guest molecules, with the exception of benzene, are able to access the tetrahedral cages. In practice the tetrahedral cages are inaccessible to benzene molecules because the narrow 3.5 Å windows do not allow entry of benzene molecules that have a kinetic diameter of 5.85 Å. To prevent the insertion of benzene molecules into the tetrahedral cages, we need to block such non-permissible MC moves. Toward this end, spherical blocks are placed in the center of these cavities. Hard spheres do not interact

with water, acetone, and alcohols molecules in such a way that the spherical blocks do not affect the adsorption of these guest molecules.

Simulations were performed using the RASPA code developed by D. Dubbeldam, S. Calero, D. E. Ellis, and R.Q. Snurr. The code and most of the force fields and models used in this work have been extensively tested and validated with a large number of experimental and simulation data.[10-12]

3. Vapor and liquid phase transitions

It is essential to gain an understanding of vapor/liquid phase transitions for water, alcohols, and benzene. Figure 3a presents calculations of the molar densities of water, methanol, ethanol, and benzene as a function of the bulk fluid phase fugacity using the Peng-Robinson equation of state. For fugacities below about 100 kPa, each of the components is in the gaseous phase. For fugacities in excess of 2 MPa, each of the substances water, methanol, ethanol, and benzene is predominantly in the liquid state with molar densities in the range of 20 – 55 mol L^{-1}. For fugacities in the range of 700 kPa to 2 MPa, both vapor and liquid phases co-exist. A similar scenario holds for equimolar ethanol/benzene mixtures; see Figure 3b.

The important message we wish to draw from the calculations in Figure 3 is that care needs to be taken when interpreting unary isotherms of water, alcohols, and benzene to be presented later. In our molecular simulations, we consistently use fugacities rather than "pressures" when plotting unary adsorption isotherms. This is vital because the bulk fluid phase could be either in the vapor phase, in the liquid phase, or a mixture of vapor and liquid phases.

4. Unary isotherms in CuBTC

Let us first consider the adsorption isotherms for water, plotted as a function of the fluid phase fugacity ranging to 10 MPa; see Figure 4.

The pure component isotherm data for water show marked inflections. The reason for these inflections can be traced to the location of water molecules within the tetrahedral pockets, and within the larger

cages. In order to correctly capture these inflections the unary isotherm data of water were fitted with the 3-site Langmuir-Freundlich model:

$$q^0 = q_{A,sat}\frac{b_A f^{\nu_A}}{1+b_A f^{\nu_A}} + q_{B,sat}\frac{b_B f^{\nu_B}}{1+b_B f^{\nu_B}} + q_{c,sat}\frac{b_C f^{\nu_C}}{1+b_C f^{\nu_C}} \quad (1)$$

The saturation capacities q_{sat}, Langmuir constants b, and the Freundlich exponents ν, are provided in Table 3. The superscript 0 emphasizes that the loadings are for pure component water.

Figure 4 presents a comparison of the CBMC simulations for water adsorption in CuBTC with 3-site Langmuir-Freundlich model. Also shown are the experimental isotherm data of Zhao et al.,[13] Yazaydin et al.,[14] and Küsgens et al.[15] measured at 298 K. Our CBMC simulations are in reasonable agreement with the experimental data; in particular, the steep portion of the isotherm is correctly reproduced. This corresponds to the filling up of the larger cages of CuBTC.

The unary isotherms for methanol, ethanol, acetone, and benzene were fitted with good accuracy with the dual-Langmuir-Freundlich model

$$q^0 = q_{A,sat}\frac{b_A f^{\nu_A}}{1+b_A f^{\nu_A}} + q_{B,sat}\frac{b_B f^{\nu_B}}{1+b_B f^{\nu_B}} \quad (2)$$

with the fits parameters as specified in Table 4.

Figure 5 provides a comparison of the CBMC simulated isotherms for water, methanol, ethanol, acetone, and benzene with 3-site, and 2-site Langmuir-Freundlich fits. The accuracy of the fits is excellent for all five guest molecules. Particularly noteworthy are the differences in the saturation capacities, $q_{sat} = q_{A,sat} + q_{B,sat} + q_{C,sat}$, of the various guest molecules: water = 54 mol kg^{-1}; methanol = 19.9 mol kg^{-1}; ethanol = 13 mol kg^{-1}; acetone = 9.9 mol kg^{-1}; benzene = 6.7 mol kg^{-1}.

For comparison purposes, the corresponding saturation capacities in TetZB are: water = 21 mol kg^{-1}; methanol = 10.6 mol kg^{-1}; ethanol = 6.8 mol kg^{-1}; acetone = 5.6 mol kg^{-1}; benzene = 3.3 mol kg^{-1}. The point we wish to stress here is that CuBTC has higher saturation capacities, a desirable feature for use in fixed-bed adsorber separations.

Let us define the fractional occupancy within the pores, θ_i, for each of the five guest molecules

$$\theta_i = \frac{q^0}{q_{sat}} \tag{3}$$

where q^0 is the molar loading of species *i* that is determined from the multi-site Langmuir-Freundlich fits. The variation of the pore occupancies with bulk fluid phase fugacity, f_i, are shown in Figure 6. We note that the pore occupancies are close to unity for operation at ambient conditions of 100 kPa and 298 K.

Most commonly, industrial separations are anticipated to operate with bulk liquid mixtures; this ensures that pore saturation conditions are reached.[16] This is an important aspect of this work, because the separations are dictated by molecular packing effects that manifest at pore saturation conditions.

An important feature of the unary isotherms for water, methanol, ethanol, acetone, and benzene is the steep increase in the loadings; this suggests the formation of molecular clustering as a consequence of hydrogen bonding effects.[17-19] In order to explore cluster formation in more detail, we determine the inverse thermodynamic factor, $1/\Gamma_i$, defined by

$$\frac{1}{\Gamma_i} \equiv \frac{\partial \ln q_i}{\partial \ln f_i} = \frac{f_i}{q_i}\frac{\partial q_i}{\partial f_i} \tag{4}$$

by analytic differentiation of eq. (1). The data for $1/\Gamma_i$ are presented in Figure 7. We prefer to plot $1/\Gamma_i$ instead of Γ_i because the latter has the undesirable property of approaching infinity as saturation loading is approached; this makes the data less easy to interpret when plotted in graphical form. For a single-site Langmuir isotherm, we have $1/\Gamma_i = (1-\theta_i) = (1 - q_i/q_{i,sat})$, i.e. the fractional vacancy. In previous work we had argued that the condition $1/\Gamma_i > 1$ implies the increase of fractional vacancy beyond unity and this is physically rationalized if we allow for molecular clustering[17-21] We note from Figure 7 that $1/\Gamma_i$ exceeds unity for a certain range of pore occupancies below about 0.5.

Experimental confirmation of clustering effects is provided by the experimental data of Tsotsalas et al.[22] Figure 8 compares the $1/\Gamma_i$ values obtained by Tsotsalas et al.[22] for methanol by numerical piece-wise differentiation of their experimental isotherms, with the values obtained from dual-Langmuir-Freundlich fits of CBMC simulated isotherms. There is reasonably good qualitative agreement with the two sets of data.

5. CBMC simulations of mixture adsorption

Figure 9, panels a, b, c, d, and e, present the results for CBMC simulations of the component loadings for adsorption of equimolar water/benzene, methanol/benzene, ethanol/benzene, methanol/ethanol, and acetone/benzene mixtures in CuBTC at 298 K. The data for methanol/ethanol mixtures that is presented here is the same as that reported in our earlier work;[23] it is included here for comparison purposes. Figure 9f presents the calculations of the corresponding adsorption selectivties for the five equimolar binary mixtures in CuBTC. In all cases, we note a reversal in the hierarchy of component loadings as conditions approach pore saturation. In all cases, we note that at conditions close to pore saturation, the adsorption is in favor of the component with the higher saturation capacity. For water/benzene mixtures, the selectivity is in favor of water at fugacities f_t > 10 kPa. For methanol/benzene and ethanol/benzene mixtures, the selectivity is in favor of the alcohol as pore saturation conditions are approached. For methanol/ethanol mixtures, the adsorption is in favor of the shorter alcohol as pore saturation is approached. For acetone/benzene mixtures, the selectivity is in favor of acetone as pore saturation conditions are approached.

For mixture adsorption, let us define the fractional occupancy within the pores, θ_t

$$\theta_t = \sum_{i=1}^{n} \frac{q_i}{q_{i,sat}} \tag{5}$$

where q_i is the molar loading of species i in the mixture, and $q_{i,sat}$ is its saturation capacity. Figure 10 shows the fractional pore occupancy θ_t for adsorption of equimolar water/benzene, methanol/benzene, ethanol/benzene, acetone/benzene, and methanol/ethanol mixtures as a function of the bulk fluid phase

fugacity, f_t. We note that the pores are nearly saturated when the bulk fluid phase fugacity exceeds about 10 kPa.

From the data in Figure 9 we conclude that CuBTC has the potential of separation of separating binary mixtures of benzene with water, methanol, ethanol, and acetone. For operation at pore saturation the selectivity is in favor of the smaller partner molecule in the mixture. Figure 11 presents the CBMC simulations for equimolar quaternary water/methanol/ethanol/benzene mixtures in CuBTC at 298 K. These results clearly indicate that water can be selectively adsorbed from a mixture containing alcohols, and benzene provided the operation is close to pore saturation conditions. Operation at 298 K, and $f_t >$ 10 kPa ensures pore saturation.

Figure 12, 13, 14, 15, and 16 present snapshots showing the average occupation profiles of constituents in, respectively, water/benzene, methanol/benzene, ethanol/benzene, acetone/benzene, and water/methanol/ethanol/benzene mixtures in CuBTC at 298 K. The large cages become increasing populated with increasing total fugacity.

6. Unary vs Mixture Adsorption: Entropy effects, H-bonding effects

To get a feel for molecular packing effects, also called entropy effects, we can compare the loadings of pure components with the loadings in mixtures at the same partial fugacity in the bulk fluid phase. Figure 17a compares CBMC simulations of adsorption of adsorption of pure water with CBMC simulations of adsorption of mixtures containing water; we have included also the CBMC mixture simulations that were reported in our previous work.[23] For all aqueous mixtures, entropy effects favor water for partial fugacities exceeds 1 kPa. Figure 17b presents the same set of data plotted in Figure 17a in a different manner; herein we divide the loadings of water in the mixture by the loadings of pure water, both compared at the same partial fugacity in the bulk fluid phase. The "enhancement" factor of water reaches a value of 8; see the shaded region. The most likely reason for this enhancement is hydrogen bonding between water and partner molecules; the partner molecules "drag" water into CuBTC. Hydrogen bonding between water and benzene is negligible, and therefore there is no enhancement of water ingress..

Figure 18 compares CBMC simulations of adsorption of adsorption of pure methanol with CBMC simulations of adsorption of mixtures containing methanol. For water/methanol mixtures, entropy effects favor water in this range of partial fugacities indicated by the arrow. For other mixtures, entropy effects favor methanol.

Figure 19 compares CBMC simulations of adsorption of adsorption of pure ethanol with CBMC simulations of adsorption of mixtures containing ethanol. For ethanol/benzene mixtures, entropy effects favor ethanol in this range of partial fugacities indicated by the arrow. For other mixtures, entropy effects cause the ethanol loading in the mixture to reduce in favor of partner molecules.

Figure 20 compares CBMC simulations of adsorption of adsorption of pure 1-propanol with CBMC simulations of adsorption of mixtures containing 1-propanol. For the range of partial fugacities indicated by the arrow, entropy effects disfavors 1-propanol adsorption in mixtures. This is due to the lower saturation capacity of 1-propanol compared to partner molecules.

Figure 21 compares CBMC simulations of adsorption of adsorption of pure benzene with CBMC simulations of adsorption of mixtures containing benzene. For the range of partial fugacities indicated by the arrow, entropy effects disfavors benzene adsorption in mixtures. This is due to the lower saturation capacity of benzene compared to partner molecules.

Let us now investigate whether IAST calculations are able to model entropy effects.

7. Summary of IAST calculation methodology

Briefly, the basic equation of Ideal Adsorbed Solution Theory (IAST) theory of Myers and Prausnitz[24] is the analogue of Raoult's law for vapor-liquid equilibrium, i.e.

$$f_i = P_i^0 x_i; \quad i = 1,2,...n \tag{6}$$

where x_i is the mole fraction in the adsorbed phase

$$x_i = \frac{q_i}{q_1 + q_2 + ...q_n} \tag{7}$$

and P_i^0 is the pressure for sorption of every component *i*, which yields the same spreading pressure, π for each of the pure components, as that for the mixture:

$$\frac{\pi A}{RT} = \int_0^{P_1^0} \frac{q_1^0(f)}{f} df = \int_0^{P_2^0} \frac{q_2^0(f)}{f} df = \int_0^{P_3^0} \frac{q_3^0(f)}{f} df = ... \quad (8)$$

where *R* is the gas constant (= 8.314 J mol^{-1} K^{-1}), and $q_i^0(f)$ is the *pure* component adsorption isotherm given by Equations (1) or Equation (2). The molar loadings $q_i^0(f)$ are expressed in the units of moles adsorbed per kg of framework, i.e. mol kg^{-1}. The units of the spreading pressure π is the same as that for surface tension, i.e. N m^{-1}; indeed the spreading pressure is the negative of the surface tension.[24] The quantity *A* on the left side of Equation (8) is the surface area per kg of framework, with units of m^2 kg^{-1}. The units of $\frac{\pi A}{RT}$, also called the adsorption potential,[25] are mol kg^{-1}.

Each of the integrals in Equation (8) can be evaluated analytically. For the 3-site Langmuir-Freundlich isotherm, the integration yields

$$\int_{f=0}^{P} \frac{q^0(f)}{f} df = \frac{q_{A,sat}}{\nu_A} \ln\left(1 + b_A P^{\nu_A}\right) + \frac{q_{B,sat}}{\nu_B} \ln\left(1 + b_B P^{\nu_B}\right) + \frac{q_{c,sat}}{\nu_C} \ln\left(1 + b_C P^{\nu_C}\right) \quad (9)$$

The right hand side of equation (9) is a function of *P*. For multicomponent mixture adsorption, each of the equalities on the right hand side of Equation (8) must satisfied. These constraints may be solved using a suitable root-finder, to yield the set of values of P_1^0, P_2^0, P_3^0,.. P_n^0, all of which satisfy Equation (8). The corresponding values of the integrals using these as upper limits of integration must yield the same value of $\frac{\pi A}{RT}$ for each component; this ensures that the obtained solution is the correct one.

The adsorbed phase mole fractions x_i are then determined from

$$x_i = \frac{f_i}{P_i^0}; \quad i = 1,2,...n \quad (10)$$

The total amount adsorbed is calculated from

$$q_t \equiv q_1 + q_2 ... + q_n = \frac{1}{\frac{x_1}{q_1^0(P_1^0)} + \frac{x_2}{q_2^0(P_2^0)} + ... + \frac{x_n}{q_n^0(P_n^0)}} \tag{11}$$

The set of equations (1), (2), (6), (7), (8) (9), and (11) need to be solved numerically to obtain the loadings, q_i of the individual components in the mixture.

8. Mixture adsorption equilibrium: CBMC vs IAST

Figures 22 and 23 compare the IAST calculations with CBMC simulations of component loadings of equimolar (a) water/benzene, (b) methanol/benzene, (c) ethanol/benzene, (d) methanol/ethanol, (e) acetone/benzene, and (f) water/methanol/ethanol/benzene mixtures in CuBTC at 298 K.

The same data is plotted in Figures 22 and 23, using linear *y*-axes, and logarithmic *y*-axes, respectively. In all cases, the IAST correctly anticipates that the adsorption is favorable to the component with the higher saturation capacity as saturation conditions are approached. However, the quantitative agreement between the CBMC mixtures simulations and IAST is not of sufficient accuracy near saturation conditions. For water/benzene, methanol/benzene, ethanol/benzene, acetone/benzene, and water/methanol/ethanol/benzene mixtures, the agreement between the IAST and CBMC simulations is good in the Henry regime at total fluid phase fugacities below about 10 Pa. For methanol/ethanol mixtures, the agreement between the IAST and CBMC simulations is excellent for $f_t < 1$ kPa. For f_t higher than the values indicated in the foregoing, there are significant quantitative departures between CBMC simulations and IAST predictions. The reasons for the deviations are most likely attributed to the influence of molecular clustering engendered by hydrogen bonding effects, as explained in detail in our earlier work.[17]

The separation performance anticipated by IAST calculations is overly optimistic; this is demonstrated by the comparisons presented in Figure 24 for adsorption selectivties for equimolar water/benzene, methanol/benzene, ethanol/benzene, and methanol/ethanol, and acetone/benzene mixtures in CuBTC at 298 K determined from (a) CBMC mixture simulations, and (b) IAST

calculations. Typically, at pore saturation, the selectivities estimated by IAST are about an order of magnitude higher than those determined from CBMC mixture simulations.

A different way to highlight the inadequacies of IAST, is to compare the data on the enhancement of water ingress in mixtures, as presented in Figure 17b, with the corresponding IAST calculations. Figure 25 presents such comparisons for (a) water/methanol, (b) water/ethanol, (c) water/1-propanol, (d) water/benzene, (e) water/methanol/ethanol/1-propanol, and (f) water/methanol/ethanol/benzene mixtures. In all six mixtures, the CBMC simulations show larger enhancement of water ingress in CuBTC than predicted by IAST calculations. This enhancement of water ingress for mixture adsorption is most likely attributable to H-bonding, as we shall demonstrate in the section below.

Figure 26 presents calculations of the adsorption selectivties for equimolar water/benzene, methanol/benzene, ethanol/benzene, and methanol/ethanol, and acetone/benzene mixtures in TetZB at 298 K determined from IAST calculations using the pure component isotherm data fit parameters presented in Table 5. For all these mixtures, the component with the higher saturation capacity is preferentially adsorbed from the mixture.

For a total fluid phase fugacity f_t = 100 kPa, the adsorption selectivities with CuBTC are comparable to the corresponding IAST-calculated selectivities obtained with TetZB, as presented in Figure 26. It must be remarked here that the IAST estimates for TetZB are most likely to be optimistic with regard to the magnitudes of the selectivities.

9. Radial distribution functions, and evidence of H-bonding effects

We now demonstrate the manifestation of molecular clustering effects induced by hydrogen bonding. For this purpose, we determined the radial distribution functions (RDFs) for distances between all combinations of O and H atoms of molecule pairs. Figure 27, panels a, b, c, and d, presents a comparison of the RDFs for $H_{benzene}$-$O_{molecule}$ and $H_{molecule}$-$O_{molecule}$ distances for water/benzene, methanol/benzene, ethanol/benzene, and water/methanol/ethanol/benzene mixtures in CuBTC at 298 K and total fluid fugacity of 1000 Pa. We note that the RDFs for H_{water}-O_{water}, $H_{methanol}$-$O_{methanol}$, and $H_{ethanol}$-$O_{ethanol}$ pairs each exhibit a first peak at an intermolecular distance of 2 Å, that is characteristic

of hydrogen bonding.[17, 26] The results presented in Figure 27d show that H-bonding between alcohol/alcohol pairs are stronger than the bonding between water/water pairs.

Remarkably, the corresponding values for $H_{benzene}$-O_{water}, $H_{benzene}$-$O_{methanol}$, and $H_{benzene}$-$O_{ethanol}$ do not display any peaks in the RDFs. This would indicate that guest molecules do not form clusters with benzene molecules, and clustering effects are restricted to water/water, methanol/methanol, and ethanol/ethanol pairs. In order for further verify this finding we determined the RDFs for $H_{benzene}$-$O_{molecule}$ distances for (a) water/benzene, (b) methanol/benzene, (c) ethanol/benzene, and (d) acetone/benzene mixtures in CuBTC at 298 K and five different total fluid fugacity values; see Figure 28. For the wide range of fugacties, f_t = 40 Pa – 10000 Pa, no peaks are observed at any molecule-benzene distance, confirming that the benzene does not form clusters with partner molecules.

Figure 29 presents the data of Krishna and van Baten[17] for RDF of H_{water}-O_{water}, $H_{methanol}$-$O_{methanol}$, and $H_{ethanol}$-$O_{ethanol}$ distances for (a) water, (b) methanol, and (c) ethanol at 300 K in ZIF-8, LTA, FAU, DDR, and MFI. These data indicate that cluster formation due to hydrogen bonding occurs in other host materials.

10. Calculation of activity coefficients using CBMC mixture simulations

It is clear from the results presented in Figures 22, 23, 24, and 25 that the assumption of an *ideal* adsorbed phase breaks down as saturation conditions are approached. Let us quantify these deviations by introducing activity coefficients following Myers and Prausnitz.[24]

To account for non-ideality effects in mixture adsorption, we introduce activity coefficients γ_i into Equation (6).

$$f_i = P_i^0 x_i \gamma_i \tag{12}$$

The CBMC mixture simulations provide information on the mole fractions of the adsorbed phase, x_i, but the activity coefficients γ_i are not known *a priori*.

We discuss a procedure by which the activity coefficients γ_i can be determined using as data inputs, the CBMC simulated component loadings in the mixture as a function of the partial fugacities, f_i, in the

bulk fluid phase. We illustrate this procedure for binary ethanol/benzene mixture. This procedure is exactly the same as the one that we had used in our earlier work.[23]

Using the Gibbs adsorption equation for mixture adsorption as starting point (cf. Equations (3.52) of Ruthven[27]), we can write the differential of the spreading pressure as

$$\frac{Ad\pi}{RT} = q_1 d\ln f_1 + q_2 d\ln f_2 \tag{13}$$

Integrating equation (13) from 0 to f_1, and f_2

$$\frac{\pi A}{RT} = \int_0^{f_1,f_2} \left(q_1 d\ln f_1 + q_2 d\ln f_2\right) = \int_0^{f_t} \left(q_1 + q_2\right) d\ln f_t \tag{14}$$

The integral in equation (14) can be determined using an appropriate quadrature formula. The approach we use here is to fit the loadings q_1, for the component 1 with the higher saturation capacity, and the total mixture loading $q_t = q_1 + q_2$ as functions, respectively, of the partial fugacities, f_1, and total mixture fugacity f_t.

The P_i^0 can be determined for each of the two components by setting the equalities:

$$\frac{\pi A}{RT} = \int_0^{f_t} \left(q_1 + q_2\right) d\ln f_t = \int_0^{P_1^0} \frac{q_1^0(f)}{f} df = \int_0^{P_2^0} \frac{q_2^0(f)}{f} df \tag{15}$$

Equation (15) can be solved to determine P_1^0, and P_2^0 as a function of the total mixture fugacity f_t. Combining the obtained values of P_1^0, and P_2^0 with Equation (12), we can determine the activity coefficients γ_i as a function of the total mixture fugacity, f_t. The adopted procedure is illustrated, step-by-step, for the CBMC ethanol/benzene mixture data reported in Figure 9c.

Step 1. We first fit the component ethanol loadings q_1, and the total mixture loading $q_t = q_1 + q_2$ as functions, respectively, of the partial fugacities, f_1, and total fugacity f_t using the Dual-Langmuir-Freundlich model. The fit parameters are specified in Table **6**. To demonstrate the goodness of the fits,

Figure **30** compares the CBMC mixture simulation data with the fits for water loadings q_1, and the total mixture loading $q_t = q_1 + q_2$ with fitted model. The fits are of excellent accuracy.

From these fits, we can determine the mole fraction of ethanol in the adsorbed phase, x_1, from the DLF fits of CBMC data using the parameter values listed, for example, in Table **6**:

$$x_1 = \frac{q_1}{q_t} \tag{16}$$

The mole fraction of benzene in the adsorbed phase, $x_2 = 1 - x_1$.

Step 2. We determine the value of $\frac{\pi A}{RT}$ by analytic integration of the first right member of Equation (15). The formula for analytic integration is as follows

$$\frac{\pi A}{RT} = \int_0^{f_t} (q_1 + q_2) d \ln f_t = \frac{q_{A,sat}}{\nu_A} \ln\left(1 + b_A f_t^{\nu_A}\right) + \frac{q_{B,sat}}{\nu_B} \ln\left(1 + b_B f_t^{\nu_B}\right) \tag{17}$$

In determining the right member of equation (17) we use the DLF fit parameters for the mixture loadings as specified in Table **6**.

Step 3. We determine P_1^0, and P_2^0 as a function of f_t by solving Equation (12) an appropriate root-finder routine.

Step 4. The activity coefficient of ethanol in the adsorbed phase is calculated from

$$\gamma_1 = \frac{f_1}{P_i^0 x_1} \tag{18}$$

The value of x_1 used in the calculations is from equation (16). The activity coefficient of benzene in the adsorbed phase is calculated from

$$\gamma_2 = \frac{f_2}{P_2^0 (1 - x_1)} \tag{19}$$

Figure 31 presents the activity coefficients γ_i for equimolar (a) water/benzene, (b) methanol/benzene, (c) ethanol/benzene, (d) methanol/ethanol, and (e) acetone/benzene mixtures in CuBTC at 298 K. For

values of the total bulk fluid phase fugacity $f_t = f_1 + f_2$ lower than about 100 Pa, the activity coefficients are practically unity. In other words, non-ideality effects come into play as the pores become increasingly occupied. For all mixtures, the activity coefficient of the component 2 with the lower saturation capacity, γ_2, reduces significantly below unity as pore saturation is approached. Concomitantly, the activity coefficient of the component 1 with the higher saturation capacity, γ_1, increases to values slightly exceeding unity.

The deviations of activity coefficients from unity values are most likely correlated with the hydrogen bonding effects.[17]

11. Modelling non-ideality effects for binary mixture adsorption

For quantifying non-ideality effects we need to model the excess Gibbs free energy

$$\frac{G^{excess}}{RT} = x_1 \ln(\gamma_1) + x_2 \ln(\gamma_2) \tag{20}$$

We extend the approaches of Talu and Myers[28, 29] and Siperstein and Myers[25] by adopting the Wilson model for the activity coefficients, along with the correction factor $\left(1-\exp\left(-C\frac{\pi A}{RT}\right)\right)$ where C is a constant to be determined from data fitting.

$$\frac{G^{excess}}{RT} = \left[-x_1 \ln(x_1 + x_2\Lambda_{12}) - x_2 \ln(x_2 + x_1\Lambda_{21})\right]\left(1-\exp\left(-C\frac{\pi A}{RT}\right)\right) \tag{21}$$

The activity coefficients are given by

$$\begin{aligned}
\ln(\gamma_1) &= \left(1 - \ln(x_1 + x_2\Lambda_{12}) - \frac{x_1}{x_1 + x_2\Lambda_{12}} - \frac{x_2\Lambda_{21}}{x_2 + x_1\Lambda_{21}}\right)\left(1-\exp\left(-C\frac{\pi A}{RT}\right)\right) \\
\ln(\gamma_2) &= \left(1 - \ln(x_2 + x_1\Lambda_{21}) - \frac{x_2}{x_2 + x_1\Lambda_{21}} - \frac{x_1\Lambda_{12}}{x_1 + x_2\Lambda_{12}}\right)\left(1-\exp\left(-C\frac{\pi A}{RT}\right)\right)
\end{aligned} \tag{22}$$

The choice of $\Lambda_{12} = \Lambda_{21} = 1$ in Equation (22) yields unity values for the activity coefficients.

The introduction of $\left(1-\exp\left(-C\frac{\pi A}{RT}\right)\right)$ imparts the correct limiting behaviors $\gamma_i \to 1; \quad f_t \to 0$ for the activity coefficients in the Henry regime. As pore saturation conditions are approached, this correction factor tends to unity $\left(1-\exp\left(-C\frac{\pi A}{RT}\right)\right)\to 1$. To illustrate this, we present calculations of the correction factor for ethanol/benzene mixtures; see Figure **32**. These calculations are based on the calculations taking $\Lambda_{12} = 1$; $\Lambda_{21}= 3.6$; $C = 0.12$ kg mol^{-1}; these values are reasonable representations of the CBMC mixture simulations for ethanol/benzene mixture.

The excess reciprocal loading for the mixture can be defined as

$$\frac{1}{q^{excess}} = \frac{1}{q_t} - \left(\frac{x_1}{q_1^0(P_1^0)} + \frac{x_2}{q_2^0(P_2^0)}\right) \tag{23}$$

The excess reciprocal loading for the mixture can be related to the partial derivative of the Gibbs free energy with respect to the adsorption potential at constant composition

$$\frac{1}{q^{excess}} = \left.\frac{\partial\left(\frac{G^{excess}}{RT}\right)}{\partial\left(\frac{\pi A}{RT}\right)}\right|_{T,x} = \left[-x_1\ln(x_1+x_2\Lambda_{12}) - x_2\ln\left(x_2+x_1\Lambda_{21}\right)\right]C\exp\left(-C\frac{\pi A}{RT}\right) \tag{24}$$

For calculation of the total mixture loading we need to replace Equation (11) by

$$q_t \equiv q_1 + q_2 = \frac{1}{\frac{x_1}{q_1^0(P_1^0)} + \frac{x_2}{q_2^0(P_2^0)} + \left[-x_1\ln(x_1+x_2\Lambda_{12}) - x_2\ln\left(x_2+x_1\Lambda_{21}\right)\right]C\exp\left(-C\frac{\pi A}{RT}\right)} \tag{25}$$

The parameters Λ_{12}, Λ_{21}, and C can be fitted to match the CBMC mixture simulations. Table 13 lists the parameter values for methanol/ethanol and ethanol/benzene mixtures obtained in this manner.

Figures 33a,b compare the RAST estimations with CBMC simulations of component loadings of the (a) ethanol/benzene, and (b) methanol/ethanol mixtures. We see that the RAST calculations offer only slight improvement over the corresponding IAST calculations. It is not possible to obtain good

agreement with CBMC mixture calculations for total fugacities significantly higher than 10 kPa. The corresponding RAST calculations of the activity coefficients are shown in Figures 33c,d. While the correct qualitative trends in γ_i are captured by the Wilson model, a good quantitative fit was not achievable, irrespective of the choice of the three parameters Λ_{12}, Λ_{21}, and C. Similarly, the RAST model for water/benzene, methanol/benzene, and acetone/benzene mixtures did not offer any significant advantage over the IAST. There appears to be a need for development of models to describe mixture adsorption taking explicit account of molecular clustering effects.

12. Non-ideality effects for mixture adsorption in FAU zeolite

Using published data on CBMC mixture simulations we shall examine the non-ideality effects for mixture adsorption in four different zeolites, FAU, DDR, MFI, and CHA.

Let us consider the adsorption of water/methanol, and water/ethanol mixtures in all-silica FAU zeolite that consists of 786 $Å^3$ cages, that are separated by 7.3 Å size windows. Figure 34 shows CBMC simulations of Krishna and van Baten[17] for pure component adsorption isotherms for water, methanol, and ethanol in all-silica FAU zeolite at 300 K. Above fluid phase fugacities of 10^4 Pa, pore saturation is reached and the hierarchy of saturation capacities water >> methanol > ethanol is a reflection of the size of the molecules.

Figure 35a presents CBMC simulations for adsorption of equimolar (partial fugacities $f_1=f_2$) water/methanol mixtures in FAU zeolite at 300 K. In the Henry regime of adsorption, the water loading is significantly below that of the alcohol. However, we note that at partial fluid phase fugacities, $f_i > 5\times10^3$ Pa, the adsorption is in favor of water, a consequence of entropy effects. The continuous solid lines are the IAST calculations using the pure component isotherm fits. IAST calculations are able to provide a reasonably good description of mixture adsorption equilibrium for partial fugacities $f_i < 1\times10^3$ Pa. For $f_i > 2\times10^3$ Pa, there are significant quantitative deviations between IAST calculations and CBMC simulations of water loadings.

Figure 35b and Figure 35c present CBMC simulations of the enhancement of (b) water, and (c) methanol ingress in FAU. The enhancement factor is defined as the loading of a component in the mixture divided by the loadings of that pure component determined at the same partial fugacity of that component in the bulk fluid phase. The CBMC data show enhancements ranging to 5 or 10, significantly higher than the corresponding enhancements calculated from IAST. This suggests that H-bonding and clustering effects are in play. Such clustering effects have the effect of dragging water molecules into the FAU framework.

The departures of CBMC simulations from IAST get reflected in the values of activity coefficients that depart from unity. Figure 35d presents the calculations of the activity coefficients γ_i, of individual components in the mixture as a function of the total fluid phase fugacity, f_1+f_2. We note that in the range of fugacities wherein enhancements are higher than unity, the activity coefficients are lower than unity.

Figure 36a presents CBMC simulations for adsorption of water/methanol mixtures in FAU zeolite at 300 K at a constant total fugacity of 1000 Pa. The continuous solid lines are the IAST calculations using the pure component fits in Table **7**. The agreement between the IAST calculations and CBMC mixture simulations is not perfect. To quantify the deviations from IAST, Figures 36b, and 36c present values of the enhancement factors for water and methanol ingress, both from CBMC simulations and from IAST. The enhancement factors determined from CBMC simulations are higher than the predictions of IAST. The IAST predicts enhancement of water and methanol ingress to be both unity, whereas CBMC simulations show enhancements higher than unity. Values of enhancement factor larger than unity also get reflected in activity coefficients, γ_i, that are lower than unity; see Figure 36d.

Figure 37a presents CBMC simulations for adsorption of equimolar (partial fugacities $f_1=f_2$) water/ethanol mixture in FAU zeolite at 300 K. In the Henry regime of adsorption, the water loading is significantly below that of the alcohol. However, we note that at partial phase fugacities, $f_i > 8\times10^3$ Pa, the adsorption is in favor of water, a consequence of entropy effects. The continuous solid lines are the IAST calculations using the pure component isotherm fits. IAST calculations are able to provide a reasonably good description of mixture adsorption equilibrium for $f_i < 3\times10^2$ Pa. For $f_i > 3\times10^2$ Pa, there

are significant quantitative deviations between IAST calculations and CBMC simulations of water loadings.

Figure 37b and Figure 37c present CBMC simulations of the enhancement of (b) water, and (c) ethanol ingress in FAU. The enhancement factor is defined as the loading of a component in the mixture divided by the loadings of that pure component determined at the same partial fugacity of that component in the bulk fluid phase. The enhancement factor for ethanol is close to unity for the entire range of fugacities.The CBMC data for water show enhancements ranging to 8, significantly higher than the enhancements calculated from IAST. This suggests that H-bonding and clustering effects are in play; water is dragged into the FAU framework due to clustering with partner ethanol molecules.

For water, the departures of CBMC simulations from IAST get reflected in the values of activity coefficients that depart from unity. Figure 37d presents the calculations of the activity coefficients γ_i, of individual components in the mixture as a function of the total fluid phase fugacity, f_1+f_2. We note that in the range of fugacities wherein enhancements of water ingress are higher than unity, the activity coefficients for water are lower than unity.

13. Non-ideality effects for mixture adsorption in DDR zeolite

Consider the adsorption of water/methanol, and water/ethanol mixtures in all-silica DDR zeolite that consists of 278 $Å^3$ cages, that are separated by 3.65 Å × 4.37 Å size windows. Figure 38 shows CBMC simulations of Krishna and van Baten[17] for pure component adsorption isotherms for water, methanol, and ethanol in DDR at 300 K. Above fluid phase fugacities of 10^5 Pa, pore saturation is reached and the hierarchy of saturation capacities water >> methanol > ethanol is a reflection of the size of the molecules.

Figure 39a presents CBMC simulations for adsorption of equimolar (partial fugacities $f_1=f_2$) water/methanol mixture in DDR zeolite at 300 K. In the Henry regime of adsorption, the water loading is significantly below that of methanol. However, we note that at partial fugacities, $f_i > 8\times10^3$ Pa, the adsorption is in favor of water, a consequence of entropy effects. The continuous solid lines are the IAST calculations using pure component isotherm fits. IAST calculations are able to provide a

reasonably good description of mixture adsorption equilibrium for $f_i < 20$ Pa. For $f_i > 20$ Pa, there are significant quantitative deviations between IAST calculations and CBMC simulations of water loadings in the mixture.

Figure 39b and Figure 39c present CBMC simulations of the enhancement of (b) water, and (c) methanol ingress in DDR. The enhancement factor is defined as the loading of a component in the mixture divided by the loadings of that pure component determined at the same partial fugacity of that component in the bulk fluid phase. The CBMC data show enhancements ranging to 20 for water, significantly higher than the enhancements calculated from IAST. This suggests that H-bonding and clustering effects are in play; water ingress is much more significantly influenced than methanol ingress.

The departures of CBMC simulations from IAST get reflected in the values of activity coefficients that depart from unity Figure 39d presents the calculations of the activity coefficients γ_i, of individual components in the mixture as a function of the total fluid phase fugacity, f_1+f_2. We note that the activity coefficient for water is significantly lower than unity in the range of fugacities for which the enhancement in water ingress exceeds unity.

Figure 40a presents CBMC simulations for adsorption of equimolar (partial fugacities $f_1=f_2$) water/ethanol mixture in DDR zeolite at 300 K. In the Henry regime of adsorption, the water loading is significantly below that of ethanol. However, we note that at partial fugacities, $f_i = 8\times10^3$ Pa, the loading of water equals that of ethanol. The continuous solid lines are the IAST calculations using pure component isotherm fits. IAST calculations are able to provide a reasonably good description of mixture adsorption equilibrium for $f_i < 10$ Pa. For $f_i > 10$ Pa, there are significant quantitative deviations between IAST calculations and CBMC simulations of water loadings in the mixture.

Figure 40b and Figure 40c present CBMC simulations of the enhancement of (b) water, and (c) ethanol ingress in DDR. The enhancement factor is defined as the loading of a component in the mixture divided by the loadings of that pure component determined at the same partial fugacity of that component in the bulk fluid phase. The CBMC data show enhancements ranging to 40 for water,

significantly higher than the enhancements calculated from IAST. This suggests that H-bonding and clustering effects are in play; water ingress is much more significantly influenced than ethanol ingress.

The departures of CBMC simulations from IAST get reflected in the values of activity coefficients that depart from unity Figure 40d presents the calculations of the activity coefficients γ_i, of individual components in the mixture as a function of the total fluid phase fugacity, f_1+f_2. We note that the activity coefficient for water is significantly lower than unity in the range of fugacities for which the enhancement in water ingress exceeds unity.

14. Non-ideality effects for mixture adsorption in MFI zeolite

Consider the adsorption of water/methanol, and water/ethanol mixtures in all-silica MFI zeolite that consists of intersecting channels of 5.5 Å. Figure 41 shows CBMC simulations of Krishna and van Baten[17] for pure component adsorption isotherms for water, methanol, and ethanol in MFI at 300 K. Above fluid phase fugacities of 10^5 Pa, pore saturation is reached and the hierarchy of saturation capacities water >> methanol > ethanol is a reflection of the size of the molecules.

Figure 42a presents CBMC simulations for adsorption of equimolar (partial fugacities $f_1=f_2$) water/methanol mixture in MFI zeolite at 300 K. In the Henry regime of adsorption, the water loading is significantly below that of methanol. However, we note that at partial fugacities, $f_i > 2\times10^4$ Pa, the adsorption is in favor of water, a consequence of entropy effects. The continuous solid lines are the IAST calculations using pure component isotherm fits. IAST calculations are able to provide a reasonably good description of mixture adsorption equilibrium for $f_i < 10$ Pa. For $f_i > 10$ Pa, there are significant quantitative deviations between IAST calculations and CBMC simulations of water loadings in the mixture.

Figure 42b and Figure 42c present CBMC simulations of the enhancement of (b) water, and (c) methanol ingress in MFI. The enhancement factor is defined as the loading of a component in the mixture divided by the loadings of that pure component determined at the same partial fugacity of that component in the bulk fluid phase. For 10 Pa $< f_i <$ 100 Pa, the CBMC data show enhancements ranging to 8 for water, significantly higher than the enhancements calculated from IAST. This suggests that H-

bonding and clustering effects are in play; water ingress is much more significantly influenced than methanol ingress.

Figure 43a presents CBMC simulations for adsorption of equimolar (partial fugacities $f_1=f_2$) water/ethanol mixture in MFI zeolite at 300 K. In the Henry regime of adsorption, the water loading is significantly below that of ethanol.

Figures 43b and 43c present CBMC simulations of the enhancement of (b) water, and (c) ethanol ingress in MFI. The enhancement factor is defined as the loading of a component in the mixture divided by the loadings of that pure component determined at the same partial fugacity of that component in the bulk fluid phase. For 10 Pa < f_i < 50 Pa, the CBMC data show enhancements ranging to 12 for water, significantly higher than the enhancements calculated from IAST. This suggests that H-bonding and clustering effects are in play at For f_i > 10 Pa; water ingress is much more significantly influenced than ethanol ingress.

Experimental evidence of the enhancement of water ingress into MFI zeolite due to H-bonding effects with partner alcohol molecules can be inferred from the experimental data of Farzaneh et al.[30] for water/butanol mixture adsorption in all-silica MFI zeolite at 308 K. The set of three experimental data points for butanol/water and water/butanol selectivities are plotted in Figures 44a, and 44b. Comparisons with IAST calculations using unary isotherm fits (unary isotherm fit parameters reported in Table 10), clearly demonstrate that the water/butanol selectivity is significantly higher in the experiments than predicted by IAST calculations. This is indicative of enhanced water ingress into MFI due to H-bonding with butanol molecules. It must be stressed that these conclusions are based on our interpretation of the Farzaneh et al.[30] experiments; these authors do not draw such conclusions and no IAST calculations were presented by them.

15. Non-ideality effects for mixture adsorption in CHA zeolite

Let us examine the data on the pure component isotherms for a series of 1-alcohols in CHA, which is a cage type zeolite that consists of 316 Å^3 sized cages separated by 3.8 Å × 4.2 Å sized windows. CBMC simulations of pure component 1-alcohols with C atoms in the 1 – 6 range in CHA at 300 K, as

reported in the work of Krishna and van Baten,[31] are shown in Figure **45**a. The continuous solid lines in Figure **45**a are fits using the dual-Langmuir-Freundlich model with parameters as specified in Table 12. The saturation capacities, $\Theta_{i,sat}$, decreases from 5.4 molecules per cage for methanol to 1 molecule per cage for 1-hexanol; see data in Figure **45**b. Figure **45**c presents snapshots of the location, and conformations, of the 1-alcohols within the cages of CHA at saturation conditions. Except for methanol, the saturation cage capacity has an integer value because 1-alcohol molecules cannot locate at the window regions.

Consider adsorption of binary equimolar fluid mixtures of methanol and ethanol in CHA. The saturation capacities are 5.5 and 4 molecules per cage, respectively. CBMC simulations on the component loadings in equilibrium with an equimolar methanol-ethanol mixture is shown in Figure 46a for varying partial fluid phase fugacities, f_i.

At $f_i < 5$ kPa, the selectivity is in favor of the component with the longer chain length, ethanol; this is "normal" behavior for mixture adsorption. However, for $f_i > 5$ kPa selectivity reversal occurs and methanol is preferentially adsorbed due to its higher packing efficiency. The IAST calculations are shown by the continuous solid lines. For partial fugacities, $f_i < 10$ kPa, the IAST calculations are in good agreement with CBMC mixture simulations.

In order to quantify the deviations between CBMC and IAST, we calculate the enhancement factors for methanol and ethanol; see Figures 46b, and 46c. The deviations between the two sets become increasingly significant for $f_i > 10$ kPa. Correspondingly, the activity coefficients are lowered below unity for $f_t > 20$ kPa; see Figure 46d.

The CBMC simulations for ethanol - 1-propanol mixtures are shown in Figure 47a. For total fluid phase fugacities, $f_t < 300$ kPa, the adsorption selectivity is strongly in favor of the longer 1-propanol molecule. However, when the total fluid phase fugacity f_t exceeds 600 kPa, we find a reversal of selectivity. This selectivity reversal is entropy-based and is ascribable to the significantly higher saturation capacity of ethanol (4 molecules per cage) in comparison to that of 1-propanol (2 molecules per cage).

The CBMC simulations for ethanol - 1-hexanol mixtures are shown in Figure 47b. For total fluid phase fugacities, f_t < 100 kPa, the adsorption selectivity is strongly in favor of the longer 1-hexanol molecule. However, when the total fluid phase fugacities, f_t exceed 200 kPa, we find a reversal of selectivity. This selectivity is entropy-based and is ascribable to the significantly higher saturation capacity of ethanol (4 molecules per cage) in comparison to that of 1-hexanol (1 molecule per cage).

The continuous solid lines in Figures 47a,b are the predictions of the Ideal Adsorbed Solution Theory (IAST) of Myers and Prausnitz[24] using pure component isotherm fits. The IAST calculations have been presented here to demonstrate that selectivity reversal is not an unexpected phenomenon, but is a natural result that is obtained for a mixture of two species having (1) lower adsorption strength, but higher saturation capacity, and (2) higher adsorption strength, but lower saturation capacity. When saturation conditions are approached the component with the higher saturation capacity is invariably preferred. This is due to the fact that vacant "sites" are more easily filled by the smaller molecule at near-saturation conditions. Though the predictions of the IAST are in general qualitative agreement with CBMC simulations, the agreement is not quantitatively perfect. Figures 47c,d present the calculations of the activity coefficient. The trends in the values of activity coefficients γ_i are similar to that observed for methanol/ethanol mixtures in CHA.

16. MD simulation methodology

Diffusion is simulated using Newton's equations of motion until the system properties, on average, no longer change in time. The Verlet algorithm is used for time integration. A time step of 1 fs was used in all simulations. For each simulation, *initializing* CBMC moves are used to place the molecules in the domain, minimizing the energy. Next, follows an *equilibration* stage. These are essentially the same as the production cycles, only the statistics are not yet taken into account. This removes any initial large disturbances in the system that do not affect statistics on molecular displacements. After a fixed number of initialization and equilibrium steps, the MD simulation *production* cycles start. For every cycle, the statistics for determining the mean square displacements (MSDs) are updated. The MSDs are determined for time intervals ranging from 2 fs to 1 ns. In order to do this, an order-*N* algorithm, as

detailed in Chapter 4 of Frenkel and Smit [32] is implemented. The Nosé-Hoover thermostat is applied to all the diffusing particles.

The self-diffusivities $D_{\text{i,self}}$ for species i are computed from MD simulations by analyzing the mean square displacement for each coordinate direction

$$D_{i,self} = \frac{1}{2n_i} \lim_{\Delta t \to \infty} \frac{1}{\Delta t} \left\langle \left(\sum_{l=1}^{n_i} \left(\mathbf{r}_{l,i}(t + \Delta t) - \mathbf{r}_{l,i}(t) \right)^2 \right) \right\rangle \tag{26}$$

CuBTC is isotropic, and the mean-square-displacements can be averaged over the three coordinate directions. Figures 48, 49, 50, and 51 present plots of the mean-square-deviations $\frac{1}{n_i} \left\langle \left(\sum_{l=1}^{n_i} \left(\mathbf{r}_{l,i}(t + \Delta t) - \mathbf{r}_{l,i}(t) \right)^2 \right) \right\rangle$, for diffusion of water, methanol, ethanol, and benzene in CuBTC at 298 K. For the calculation of the $D_{\text{i,self}}$ using Equation (27), the slopes of the MSD vs time plots were determined for the time interval t = 100 ps to t = 1000 ps; in this time interval the plots are linear.

For single component diffusion, the Maxwell-Stefan diffusivity can be determined for each of the coordinate directions from

$$Đ_i = \frac{1}{2} \lim_{\Delta t \to \infty} \frac{1}{n_i} \frac{1}{\Delta t} \left\langle \left(\sum_{l=1}^{n_i} \left(\mathbf{r}_{l,i}(t + \Delta t) - \mathbf{r}_{l,i}(t) \right) \right)^2 \right\rangle \tag{27}$$

If we define the self-exchange coefficient $Đ_{\text{ii}}$ as a diffusivity characteristic of molecule-molecule interactions, we get the interpolation formula for self-diffusivity

$$1/D_{i,self} = 1/Đ_i + 1/Đ_{ii} \tag{28}$$

Equation (28), formally valid for *both* micro- and meso-porous materials, will be derived in a later section starting with the M-S equations for binary mixture diffusion for identical species, tagged, and un-tagged. At any loading $D_{\text{i,self}} \le Đ_{\text{i}}$; this is because individual jumps of molecules are *correlated* due to re-visitation of sites that have been recently abandoned. The $Đ_{\text{i}}$, reflecting *collective* motion of molecules is free from such correlation effects; it is for this reason that the $Đ_{\text{i}}$ are amenable to simpler interpretation, and modeling, than the $D_{\text{i,self}}$.

In this work, we determined only the self-diffusivities of water, methanol, ethanol, and benzene in CuBTC at 298 K; the data are summarized in Figure 52.

17. Loading dependence of unary diffusivities in CuBTC

The simplest model to describe the occupancy dependence of the Maxwell-Stefan diffusivity is

$$Đ_i = Đ_i(0)(1-\theta_i) \tag{29}$$

where $Đ_i(0)$ is the diffusivity in the limiting case of vanishingly small *fractional occupancy*, defined by

$$\theta_i \equiv c_i / c_{i,sat} \tag{30}$$

The key to the quantification of the concentration dependence of $Đ_i$ is to determine how the vacancy $(1-\theta_i)$ changes with increased pore concentration. This information is contained in the *inverse thermodynamic factor* $1/\Gamma_i$. If the adsorbed phase concentration follows a single-site Langmuir isotherm

$$c_i = c_{i,sat}\frac{b_i f_i}{1+b_i f_i} \tag{31}$$

we obtain from eqn (4)

$$1/\Gamma_i = (1-c_i/c_{i,sat}) = (1-\theta_i) \tag{32}$$

Equation (32) shows that inverse thermodynamic factor, $1/\Gamma_i$, equals the fractional *vacancy* $(1-\theta_i)$. In the general case where the component adsorption exhibits inflection behavior, due perhaps to second-order phase transitions, $1/\Gamma_i$ provides a good indicator of how the availability of adsorption sites changes with increased bulk fluid phase fugacity. We can generalize eqn (29) to cater for more complex adsorption isotherm characteristics by writing

$$Đ_i = Đ_i(0)\frac{1}{\Gamma_i} \tag{33}$$

Equation (**33**) would lead us to expect that that the sharp peak in the loading dependence of $1/\Gamma_i$ would cause a corresponding peak in the loading dependence of $Đ_i$. This expectation is fulfilled for the

experimental data of Chmelik et al.[33], obtained by transient uptake within crystals of CuBTC using Infrared Microscopy (IRM), of n-butane (nC4, T_c = 425 K), iso-butane (iC4, T_c = 408 K), neopentane (neo-P, T_c = 434 K), and 2-methylbutane (2MB, T_c = 460 K) at T = 298 K, significantly lower than the critical temperatures of each of the four guest species; see Figure 53. The observed behaviors of $1/\Gamma_i$ and $Đ_i$ for loadings Θ_i < 8 molecules per unit cell needs special attention and explanation. The CuBTC structure consists of two types of "cages" and two types of "windows" separating these cages. Large cages are inter-connected by 9 Å windows of square cross-section. The large cages are also connected to tetrahedral-shaped pockets of ca. 6 Å size through triangular-shaped windows of ca. 4.6 Å size. There are 8 tetrahedral pockets per unit cell, and these are preferred locations of molecules at low loadings. Each pocket can accommodate only one of nC4, iC4, neo-P or 2MB; this is illustrated by the snapshot in Figure 54 for neo-P adsorbed in CuBTC. For loadings Θ_i < 8 molecules per unit cell, the alkanes prefer location in the pockets, and the diffusion characteristics are dictated by hops across triangular windows of 4.6 Å. Consequently, the diffusivities tend to be low. The diffusivities of molecules inhabiting the larger cages are about an order of magnitude higher because they correspond to hops across larger 9 Å windows. As the molecules begin to populate the larger cages, the $Đ_i$ increase sharply till a maximum is reached.

With the above background information using experimental data from the literature, let us analyze the characteristics of self-diffusivities of water, methanol, ethanol, and benzene in CuBTC at 298 K presented in Figure 52.

The tetrahedral pockets can accommodate about 9 molecules of water (see Table 2), and this explains the low diffusivity values for occupancies below about 0.2.

Compared at the same fractional pore occupancy, it is interesting to note that the diffusivities of benzene are higher than those for either methanol or ethanol. The most likely reason for this is the molecular clustering effects are practically non-existent for benzene molecules. Methanol, and ethanol, on the other hand experience strong clustering, and this explains the lower diffusivity values. The molecular clustering effects for methanol are stronger than for ethanol; for this reason, the methanol

diffusivities are slightly lower than that of ethanol, when compared at the same value of pore occupancy.

In order to rationalize the loading dependences of the diffusivities, let us compare $D_{i,self}$ vs q_i data with $1/\Gamma_i$ vs. q_i data. Figure 55 present plots of MD simulations of the self-diffusivities $D_{i,self}$, and the inverse thermodynamic factor $1/\Gamma_i$ in CuBTC of (a) water, (b) methanol, (c) ethanol, and (d) benzene as a function of the component loading, q_i. Figure 56 presents the corresponding plots using the fractional pore occupancy, θ_i, on the x-axis.

The characteristics of the $D_{i,self}$ vs q_i are largely derived from the corresponding characteristics of $1/\Gamma_i$ vs. q_i data. This finding is in agreement with the corresponding observation made in respect of the $Đ_i$ vs, q_i data for n-butane, iso-butane, neopentane, and 2-methylbutane in CuBTC.[33, 34]

A further point to note is that the $D_{i,self}$ vs θ_i data for methanol displays a step-wise characteristic; the diffusivity values in the range $0.6 < \theta_i < 0.8$ are practically the same. Experimental data of Tsotsalas et al.[22] for transient desorption profiles for methanol in CuBTC at 298 K was found to display step-wise characteristics; see Figure 57a. The explanation for the step-wise desorption is clearly to be found in the correspond loading dependence of the diffusivities that is strongly influenced by molecular clustering; this conclusion is re-enforced in Figure 57b that presents a comparison of the experimental transient desorption profile with the loading dependence of the self-diffusivity.

18. Notation

A	surface area per kg of framework, $m^2\ kg^{-1}$
b_A	Langmuir-Freundlich constant for adsorption site A, $Pa^{-\nu_A}$
b_B	Langmuir-Freundlich constant for adsorption site B, $Pa^{-\nu_B}$
b_C	Langmuir-Freundlich constant for adsorption site C, $Pa^{-\nu_C}$
C	constant used in equation (22), $kg\ mol^{-1}$
$Đ_i$	Maxwell-Stefan diffusivity, $m^2\ s^{-1}$
D_i	Fick diffusivity of species i, $m^2\ s^{-1}$
$D_{i,self}$	self-diffusivity of species i, $m^2\ s^{-1}$
f_i	partial fugacity of species i, Pa
f_t	total fugacity of bulk fluid mixture, Pa
n	number of species in the mixture, dimensionless
P_i^0	sorption pressure, Pa
q_i	component molar loading of species i, $mol\ kg^{-1}$
q_t	total molar loading for mixture adsorption, $mol\ kg^{-1}$
$q_{i,sat}$	molar loading of species i at saturation, $mol\ kg^{-1}$
Q_{st}	isosteric heat of adsorption, $J\ mol^{-1}$
$\mathbf{r}_{l,i}(t)$	position vector for molecule l of species i at any time t, m
R	gas constant, 8.314 $J\ mol^{-1}\ K^{-1}$
t	time, s
T	absolute temperature, K
V_p	pore volume, $m^3\ kg^{-1}$

Greek letters

γ_i	activity coefficient of component i in adsorbed phase, dimensionless
Γ_i	thermodynamic factor, dimensionless

ν	exponent in multi-site-Langmuir-Freundlich isotherm, dimensionless
π	spreading pressure, N m^{-1}
Λ_{ij}	Wilson parameters, dimensionless
θ_i	fractional occupancy of component *i*, dimensionless
θ_t	fractional occupancy for mixture adsorption, dimensionless

Subscripts

i	referring to component *i*
t	referring to total mixture

Table 1. Lennard Jones parameters and point charges for the Cu-BTC and adsorbates.

Atom types	Epsilon/k_B (K)	Sigma (Å)	Charge (*e*)
Adsorbates			
CH_3_C_ol	98.0	3.75	-
CH_3_O_ol	98.0	3.75	0.265
CH_2_C_ol	46.0	3.95	-
CH_2_O_ol	46.0	3.95	0.265
CH_3_C_ke	98.0	3.75	
C_O_ke	40.0	3.82	0.424
O_ke	79.0	3.05	-0.424
O_ol	93.0	3.02	-0.7
H_ol	-	-	0.435
O_water	89.516	3.097	-
H_water	-	-	0.241
Dummy_water	-	-	-0.241
C_benzene	30.7	3.6	-0.095
H_benzene	25.45	2.36	0.095
Cu-BTC			
MOF-Cu	2.518	3.114	1.248
MOF-O	48.19	3.03	-0.624
MOF-C1	47.86	3,47	0.494
MOF-C2	47.86	3.47	0.13
MOF-C3	47.86	3.47	-0.156
MOF-H	7.65	2.85	0.156

Table 2. Number of molecules that can be located in the tetrahedral pockets.

	f kPa	Loading /molec uc^{-1}	Loading in T1 cages/ molec uc^{-1}	Tetrahedral cages molec/T1 cage
Methanol	10000	202	29	3-4
Ethanol	50	125	21	2-3
1-Propanol	30000	98	8	1
Water	30000	512	72	9

No benzene mlecules can be located within the tetrahedral cages.

Table 3. 3-site Langmuir-Freundlich isotherm fits for adsorption of water in CuBTC at 298 K.

	Site A			Site B			Site C		
	$q_{A,sat}$ / mol kg^{-1}	b_A / Pa$^{-\nu_{iA}}$	ν_A	$q_{B,sat}$ / mol kg^{-1}	b_B / Pa$^{-\nu_{iB}}$	ν_B	$q_{C,sat}$ / mol kg^{-1}	b_C / Pa$^{-\nu_C}$	ν_C
water	22	5.48 $\times 10^{-4}$	1	22	6.24 $\times 10^{-32}$	10	10	2.51 $\times 10^{-4}$	0.6

Table 4. Dual-site Langmuir-Freundlich parameters for adsorption of methanol, ethanol, acetone, and benzene at 298 K in CuBTC.

Adsorbate	Site A			Site B		
	$q_{A,sat}$ mol kg^{-1}	b_{A0} Pa$^{-\nu_A}$	ν_A dimensionless	$q_{B,sat}$ mol kg^{-1}	b_{B0} Pa$^{-\nu_B}$	ν_B dimensionless
methanol	8.4	3.82×10^{-4}	1.03	11.5	9.3×10^{-16}	6.5
ethanol	5	2.29×10^{-3}	0.97	8	6.41×10^{-7}	3.2
acetone	5	4.83×10^{-17}	7.5	4.9	1.39×10^{-2}	0.7
benzene	4.6	2.76×10^{-6}	3.1	2.1	3.96×10^{-3}	1

Table 5. Dual-site Langmuir-Freundlich parameters for adsorption of water, methanol, ethanol, 1-propanol, 2-propanol, chloroform, benzene, and acetone at 298 K in TetZB. These fits are for the "adsorption" branch of the isotherms. The data are from Motkuri et al.[35]

Adsorbate	Site A			Site B		
	$q_{A,sat}$ mol kg^{-1}	b_{A0} $Pa^{-\nu_A}$	ν_A dimensionless	$q_{B,sat}$ mol kg^{-1}	b_{B0} $Pa^{-\nu_B}$	ν_B dimensionless
water	3	4.01×10^{-5}	0.94	18	3.02×10^{-46}	13
methanol	4.6	1.28×10^{-36}	10	6	5.08×10^{-3}	0.62
ethanol	3.6	3.97×10^{-38}	12	3.2	8.4×10^{-3}	0.7
1-propanol	2.7	5.92×10^{-35}	12.5	2.5	2.79×10^{-2}	0.6
2-propanol	2.7	4.83×10^{-27}	7.8	1.7	4.43×10^{-2}	0.6
chloroform	1.75	1.22×10^{-39}	13.2	2.7	4.76×10^{-2}	0.4
benzene	1.6	1×10^{-36}	17.5	17	2.97×10^{-2}	0.12
acetone	3	6.48×10^{-14}	4	2.6	2.49×10^{-1}	0.2

Table 6. Dual-site Langmuir-Freundlich parameters for ethanol/benzene mixture adsorption at 298 K in CuBTC.

Adsorbate	Site A			Site B		
	$q_{A,sat}$ mol kg^{-1}	b_{A0} $Pa^{-\nu_A}$	ν_A dimensionless	$q_{B,sat}$ mol kg^{-1}	b_{B0} $Pa^{-\nu_B}$	ν_B dimensionless
ethanol	4.5	2.57×10^{-3}	0.9	4.7	2.04×10^{-5}	2.8
Total loading of ethanol and benzene	4.4	2.1×10^{-3}	1.1	7.5	2.33×10^{-14}	8

Table 7. Dual-site Langmuir-Freundlich parameters for adsorption of water, methanol, and ethanol at 300 K in all-silica FAU zeolite. The fit parameters are based on the CBMC simulations of pure component isotherms presented in earlier work.[17]

Adsorbate	Site A			Site B		
	$q_{A,sat}$ mol kg^{-1}	b_{A0} Pa$^{-\nu_A}$	ν_A dimensionless	$q_{B,sat}$ mol kg^{-1}	b_{B0} Pa$^{-\nu_B}$	ν_B dimensionless
water	16	1.54×10^{-121}	33	4.6	624×10^{-5}	1
methanol	3.4	6.36×10^{-16}	4.6	5.8	1.68×10^{-4}	1
ethanol	2.5	3.19×10^{-13}	4.9	2.9	1×10^{-3}	1.05

Table 8. Dual-site Langmuir-Freundlich parameters for pure component water, methanol, and ethanol at 300 K in all-silica DDR zeolite. The fit parameters are based on the CBMC simulations of pure component isotherms presented in earlier work.[17] Note that the saturation capacities are specified in molecules per cage; multiply these by 0.832157 to obtain the values in mol per kg framework.

	Site A			Site B		
	$\Theta_{i,A,sat}$ Molecules cage^{-1}	$b_{i,A}$ $Pa^{-\nu_i}$	$\nu_{i,A}$ dimensionless	$\Theta_{i,B,sat}$ molecules cage^{-1}	$b_{i,B}$ $Pa^{-\nu_i}$	$\nu_{i,B}$ dimensionless
water	8.083	3.85×10^{-16}	4	2.667	1.73×10^{-5}	1
methanol	2.1667	1.49×10^{-4}	1.25	1.9167	6×10^{-4}	0.77
ethanol	1.8167	7.66×10^{-3}	1	0.775	8.59×10^{-6}	1

Table 9. Dual-site Langmuir-Freundlich parameters for adsorption of water, methanol, and ethanol at 300 K in all-silica MFI zeolite. The fit parameters are based on CBMC simulations of Krishna and van Baten.[17]

Adsorbate	Site A			Site B		
	$q_{A,sat}$ mol kg^{-1}	b_{A0} Pa$^{-\nu_A}$	ν_A dimensionless	$q_{B,sat}$ mol kg^{-1}	b_{B0} Pa$^{-\nu_B}$	ν_B dimensionless
water	6.7	6.37×10^{-24}	6.2	3.6	1.09×10^{-5}	1.04
methanol	2.4	1×10^{-4}	1.64	1.4	1.92×10^{-3}	0.7
ethanol	1.1	2.82×10^{-4}	2.7	1.7	1.91×10^{-2}	0.9

Table 10. Dual-site Langmuir parameters for adsorption of water, and butanol at 308 K in all-silica MFI zeolite. The parameter values are from Table 1 of Farzaneh et al.[30]

Adsorbate	Site A		Site B	
	$q_{A,sat}$ mol kg^{-1}	b_{A0} Pa^{-1}	$q_{B,sat}$ mol kg^{-1}	b_{B0} Pa^{-1}
water	0.23	48.38×10^{-3}	2.96	0.17×10^{-3}
butanol	1.8	860×10^{-3}		

Table 11. Experimental data of Farzaneh et al.[30] for water(1)/butanol(2) mixture adsorption in all-silica MFI zeolite, along with comparisons with IAST calculations using the unary isotherm fit parameters in Table 10.

Vapor phase partial pressures		Vapor phase mole fraction of butanol	Experimental data		IAST calculations	
f_1/ kPa	f_2/ kPa	y_2	Butanol/ Water selectivity Experiment	Water/ Butanol selectivity Experiment	Butanol/ Water selectivity IAST	Water/ Butanol selectivity IAST
2.04	0.35	0.146	107	264.7	0.009345794	0.003778191
2.03	0.57	0.219	84	218.5	0.011904762	0.00457721
1.8	0.7	0.28	62	199.5	0.016129032	0.005013702

Table 12. Dual-site Langmuir-Freundlich parameters for pure component water, and 1-alcohols in CHA at 300 K. The fit parameters are based on the CBMC simulations of pure component isotherms presented in earlier work.[31] Note that the saturation capacities are specified in molecules per cage; multiply these by 1.387 to obtain the values in mol per kg framework.

$$\Theta_i = \Theta_{i,A,sat}\frac{b_{i,A}f_i^{\nu_{i,A}}}{1+b_{i,A}f_i^{\nu_{i,A}}} + \Theta_{i,B,sat}\frac{b_{i,B}f_i^{\nu_{i,B}}}{1+b_{i,B}f_i^{\nu_{i,B}}}$$

	Site A			Site B		
	$\Theta_{i,A,sat}$ Molecules cage^{-1}	$b_{i,A}$ $Pa^{-\nu_i}$	$\nu_{i,A}$ dimensionless	$\Theta_{i,B,sat}$ molecules cage^{-1}	$b_{i,B}$ $Pa^{-\nu_i}$	$\nu_{i,B}$ dimensionless
methanol	12	7.86×10^{-59}	17	9	8.32×10^{-6}	1
methanol	2.7	6.77×10^{-11}	3.3	2.7	4.45×10^{-4}	1
ethanol	2	7.93×10^{-5}	0.87	2	3.6×10^{-3}	1.14
1-propanol	1	1.28×10^{-2}	1.8	1	9.11×10^{-2}	1
1-butanol	1	0.231	1.46	1	0.5066	1
1-pentanol	0.5	19.26	1.72	0.5	6.91	1
1-hexanol	0.5	2561	2.4	0.5	24.8	1

Table 13. Wilson non-ideality parameters for binary mixtures in CuBTC at 298 K.

	Λ_{12}	Λ_{21}	C
methanol/ethanol	1.1	3.5	0.028
ethanol/benzene	1	3.6	0.12

19. References

(1) Rai, N.; Siepmann, J. I. Transferable Potentials for Phase Equilibria. 9. Explicit Hydrogen Description of Benzene and Five-membered and Six-membered Heterocyclic Aromatic Compounds, *J. Phys. Chem. B* **2007**, *111*, 10790-10799.

(2) Rick, S. W. A Reoptimization of the Five-site Water Potential (TIP5P) for use with Ewald Sums, *J. Chem. Phys.* **2004**, *120*, 6085-6093.

(3) Castillo, J. M.; Vlugt, T. J. H.; Calero, S. Understanding Water Adsorption in Cu-BTC Metal-Organic Frameworks, *J. Phys. Chem. C* **2008**, *112*, 15934-15939.

(4) Peng, X.; Lin, L.-C.; Sun, W.; Smit, B. Water Adsorption in Metal–Organic Frameworks with Open-Metal Sites, *A.I.Ch.E.J.* **2015**, *61*, 677-687.

(5) Chen, B.; Potoff, J. J.; Siepmann, J. I. Monte Carlo Calculations for Alcohols and Their Mixtures with Alkanes. Transferable Potentials for Phase Equilibria. 5. United-Atom Description of Primary, Secondary, and Tertiary Alcohols, *J. Phys. Chem. B* **2001**, *105*, 3093-3104.

(6) Stubbs, J. M.; Potoff, J. J.; Siepmann, J. I. Transferable potentials for phase equilibria. 6. United-atom description for ethers, glycols, ketones, and aldehydes, *J. Phys. Chem. B* **2004**, *108*, 17596-17605.

(7) Chui, S. S. Y.; Lo, S. M. F.; Charmant, J. P. H.; Orpen, A. G.; Williams, I. D. A Chemically Functionalizable Nanoporous Material $[Cu_3(TMA)_2(H2O)_3]_n$, *Science* **1999**, *283*, 1148-1150.

(8) Mayo, S. L.; Olafson, B. D.; Goddard, W. A. DREIDING: A Generic Force Field for Molecular Simulations, *J. Phys. Chem.* **1990**, *94*, 8897-8909.

(9) Rappé, A. K.; Casewit, C. J.; Colwel, K. S.; Goddard, W. A.; Skiff, W. M. UFF, A Full Periodic Table Force Field for Molecular Mechanics and Molecular Dynamics Simulations, *J. Am. Chem. Soc.* **1992**, *114*, 10024-10035.

(10) Gutierrez-Sevillano, J. J.; Dubbeldam, D.; Bellarosa, L.; Lopez, N.; Liu, X.; Calero, S. Strategies to Simultaneously Enhance the Hydrostability and the Alcohol-Water Separation Behavior of Cu-BTC, *J. Phys. Chem. C* **2013**, *117*, 20706-20714.

(11) Gutierrez-Sevillano, J. J.; Vincent-Luna, J. M.; Dubbeldam, D.; Calero, S. Molecular Mechanisms for Adsorption in Cu-BTC Metal Organic Framework, *J. Phys. Chem. C* **2013**, *117*, 11357-11366.

(12) Calero, S.; Gómez-Álvarez, P. Insights into the Adsorption of Water and Small Alcohols on the Open-Metal Sites of Cu-BTC via molecular simulation, *J. Phys. Chem. C* **2015**, *119*, 467-472.

(13) Zhao, Z.; Wang, S.; Yang, Y.; Li, X.; Li, J.; Li, Z. Competitive Adsorption and Selectivity of Benzene and Water Vapor on the Microporous Metal Organic Frameworks (HKUST-1), *Chem. Eng. J.* **2015**, *259*, 79-89.

(14) Yazaydın, A. Ö.; Benin, A. I.; Faheem, S. A.; Jakubczak, P.; Low, J. J.; Willis, R. R.; Snurr, R. Q. Enhanced CO_2 Adsorption in Metal-Organic Frameworks via Occupation of Open-Metal Sites by Coordinated Water Molecules, *Chem. Mater.* **2009**, *21*, 1425-1430.

(15) Küsgens, P.; Rose, M.; Senkovska, I.; Fröde, H.; Henschel, A.; Siegle, S. Characterization of Metal-Organic Frameworks by Water Adsorption, *Microporous Mesoporous Mater.* **2009**, *120*, 325-330.

(16) Krishna, R. Separating Mixtures by Exploiting Molecular Packing Effects in Microporous Materials, *Phys. Chem. Chem. Phys.* **2015**, *17*, 39-59.

(17) Krishna, R.; van Baten, J. M. Hydrogen Bonding Effects in Adsorption of Water-alcohol Mixtures in Zeolites and the Consequences for the Characteristics of the Maxwell-Stefan Diffusivities, *Langmuir* **2010**, *26*, 10854-10867.

(18) Krishna, R.; van Baten, J. M. Highlighting Pitfalls in the Maxwell-Stefan Modeling of Water-Alcohol Mixture Permeation across Pervaporation Membranes, *J. Membr. Sci.* **2010**, *360*, 476-482.

(19) Krishna, R.; van Baten, J. M. Influence of Adsorption Thermodynamics on Guest Diffusivities in Nanoporous Crystalline Materials, *Phys. Chem. Chem. Phys.* **2013**, *15*, 7994-8016.

(20) Krishna, R.; van Baten, J. M. Investigating cluster formation in adsorption of CO_2, CH_4, and Ar in zeolites and metal organic frameworks at sub-critical temperatures, *Langmuir* **2010**, *26*, 3981-3992.

(21) Krishna, R.; van Baten, J. M. Highlighting a variety of unusual characteristics of adsorption and diffusion in microporous materials induced by clustering of guest molecules, *Langmuir* **2010**, *26*, 8450-8463.

(22) Tsotsalas, M.; Hejcik, P.; Sumida, K.; Kalay, Z.; Furukawa, S.; Kitagawa, S. Impact of Molecular Clustering inside Nanopores on Desorption Processes, *J. Am. Chem. Soc.* **2013**, *135*, 4608-4611.

(23) Gutierrez-Sevillano, J. J.; Calero, S.; Krishna, R. Selective Adsorption of Water from Mixtures with 1-Alcohols by Exploitation of Molecular Packing Effects in CuBTC, *J. Phys. Chem. C* **2015**, *119*, 3658-3666.

(24) Myers, A. L.; Prausnitz, J. M. Thermodynamics of Mixed Gas Adsorption, *A.I.Ch.E.J.* **1965**, *11*, 121-130.

(25) Siperstein, F. R.; Myers, A. L. Mixed-Gas Adsorption, *A.I.Ch.E.J.* **2001**, *47*, 1141-1159.

(26) Zhang, C.; Yang, X. Molecular dynamics simulation of ethanol/water mixtures for structure and diffusion properties, *Fluid Phase Equilib.* **2005**, *231*, 1-10.

(27) Ruthven, D. M. Principles of Adsorption and Adsorption Processes; John Wiley: New York, 1984.

(28) Talu, O.; Myers, A. L. Rigorous Thermodynamic Treatment of Gas-Adsorption, *A.I.Ch.E.J.* **1988**, *34*, 1887-1893.

(29) Talu, O.; Myers, A. L. Multicomponent Adsorption Equilibria of Nonideal Mixtures, *A.I.Ch.E.J.* **1986**, *32*, 1263-1276.

(30) Farzaneh, A.; Zhou, M.; Potapova, E.; Bacsik, Z.; Ohlin, L.; Holmgren, A.; Hedlund, J.; Grahn, M. Adsorption of Water and Butanol in Silicalite-1 Film Studied with *in Situ* Attenuated Total Reflectance−Fourier Transform Infrared Spectroscopy, *Langmuir* **2015**, *31*, 4887-4894.

(31) Krishna, R.; van Baten, J. M. Entropy-based Separation of Linear Chain Molecules by Exploiting Differences in the Saturation Capacities in Cage-type Zeolites, *Sep. Purif. Technol.* **2011**, *76*, 325-330.

(32) Frenkel, D.; Smit, B. Understanding Molecular Simulations: From Algorithms to Applications; 2nd Edition, Academic Press: San Diego, 2002.

(33) Chmelik, C.; Kärger, J.; Wiebcke, M.; Caro, J.; van Baten, J. M.; Krishna, R. Adsorption and Diffusion of Alkanes in CuBTC Crystals Investigated Using Infrared Microscopy and Molecular Simulations, *Microporous Mesoporous Mater.* **2009**, *117*, 22-32.

(34) Krishna, R. Diffusion in Porous Crystalline Materials, *Chem. Soc. Rev.* **2012**, *41*, 3099-3118.

(35) Motkuri, R. K.; Thallapally, P. K.; Annapureddy, H. V. R.; Dang, L.; Krishna, R.; Nune, S. K.; Fernandes, C. A.; Liu, J.; McGrail, B. P. Separation of Polar Compounds using a Flexible Metal-Organic Framework, *Chem. Commun.* **2015**, *51*, 8421-8424.

20. Caption for Figures

Figure 1. Paddle-wheel chemical structure of CuBTC.

Figure 2. Cage connectivity of CuBTC framework.

Figure 3. (a) Molar densities of pure water, methanol, ethanol, and 1-propanol as a function of the bulk fluid phase fugacities. (b) Molar densities of equimolar water/ethanol mixtures as a function of the bulk fluid phase fugacity, f_t. These calculations are based on the Peng-Robinson equation of state.

Figure 4. Comparison of the CBMC simulations for water adsorption in CuBTC with 3-site Langmuir-Freundlich model. Also shown are the experimental isotherm data of Zhao et al.,[13] Yazaydin et al.,[14] and Küsgens et al.[15] measured at 298 K.

Figure 5. (a) Comparison of the CBMC simulations for adsorption of water, methanol, ethanol, acetone, and benzene in CuBTC with multi-site-Langmuir-Freundlich model.

Figure 6. The fractional occupancy within the pores, θ_i, for guest molecules as a function of the bulk fluid phase fugacity, f_i.

Figure 7. The inverse thermodynamic factor, $1/\Gamma_i$, plotted as a function of the (a) molar loading, and (b) fractional pore occupancy for water, methanol, ethanol, acetone, and benzene in CuBTC at 298 K. The $1/\Gamma_i$ are calculated by differentiation of multi-site-Langmuir-Freundlich fits of the isotherms.

Figure 8. Variation of the inverse thermodynamic correction factor with fractional occupancy for methanol in CuBTC at 298 K. The experimental data of Tsotsalas et al.[22] are compared with the $1/\Gamma_i$ obtained from dual-Langmuir-Freundlich fits of the CBMC simulated isotherms.

Figure 9. CBMC simulations for equimolar (a) water/benzene, (b) methanol/benzene, (c) ethanol/benzene, (d) methanol/ethanol, and (e) acetone/benzene mixtures in CuBTC at 298 K. The CBMC simulations for equimolar methanol/ethanol mixtures, already reported in earlier work,[23] are also included here for comparison purposes. (f) Adsorption selectivties for equimolar water/benzene, methanol/benzene, ethanol/benzene, and methanol/ethanol, and acetone/benzene mixtures in CuBTC at 298 K.

Figure 10. Calculations of total pore occupancy, θ_t, for adsorption of equimolar water/benzene, methanol/benzene, ethanol/benzene, acetone/benzene and methanol/ethanol mixtures in CuBTC at 298 K.

Figure 11. CBMC simulations for equimolar water/methanol/ethanol/benzene mixtures in CuBTC at 298 K.

Figure 12. Average occupation profiles of water (top) and benzene (bottom) in the binarywater/benzene mixture.

Figure 13. Average occupation profiles of methanol (top) and benzene (bottom) in the binary methanol/benzene mixture.

Figure 14. Average occupation profiles of ethanol (top) and benzene (bottom) in the binary ethanol/benzene mixture.

Figure 15. Average occupation profiles of acetone (top) and benzene (bottom) in the binary acetone/benzene mixture.

Figure 16. Average occupation profiles of benzene, methanol, ethanol, and water in the quaternary mixture.

Figure 17. (a) CBMC simulations of adsorption of adsorption of pure water with CBMC simulations of adsorption of mixtures containing water. The comparisons are on the basis of the same partial fugacity of water in the bulk fluid phase. (b) CBMC simulations of the enhancement of water ingress in CuBTC. The enhancement factor is defined as the loading of water in the mixture divided by the loadings of pure water.

Figure 18. CBMC simulations of adsorption of adsorption of pure methanol with CBMC simulations of adsorption of mixtures containing methanol. The comparisons are on the basis of the same partial fugacity of methanol in the bulk fluid phase.

Figure 19. CBMC simulations of adsorption of adsorption of pure ethanol with CBMC simulations of adsorption of mixtures containing ethanol. The comparisons are on the basis of the same partial fugacity of ethanol in the bulk fluid phase.

Figure 20. CBMC simulations of adsorption of adsorption of pure 1-propanol with CBMC simulations of adsorption of mixtures containing 1-propanol. The comparisons are on the basis of the same partial fugacity of 1-propanol in the bulk fluid phase.

Figure 21. CBMC simulations of adsorption of adsorption of pure benzene with CBMC simulations of adsorption of mixtures containing benzene. The comparisons are on the basis of the same partial fugacity of benzene in the bulk fluid phase.

Figure 22. Comparison of CBMC simulations for equimolar (a) water/benzene, (b) methanol/benzene, (c) ethanol/benzene, (d) methanol/ethanol, (e) acetone/benzene, and (f) water/methanol/ethanol/benzene mixtures in CuBTC at 298 K with IAST calculations. In these plots the component loadings are represented on linear *y*-axes.

Figure 23. Comparison of CBMC simulations for equimolar (a) water/benzene, (b) methanol/benzene, (c) ethanol/benzene, (d) methanol/ethanol, (e) acetone/benzene, and (f) water/methanol/ethanol/benzene mixtures in CuBTC at 298 K with IAST calculations. In these plots the component loadings are represented on logarthmic *y*-axes.

Figure 24. Adsorption selectivties for equimolar water/benzene, methanol/benzene, ethanol/benzene, and methanol/ethanol, and acetone/benzene mixtures in CuBTC at 298 K determined from (a) CBMC mixture simulations, and (b) IAST calculations. (c) Comparison of selectivities obtained from CBMC with IAST calculations.

Figure 25. Comparison of CBMC simulations and IAST calculations of the enhancement of water ingress in CuBTC. The enhancement factor is defined as the loading of water in the mixture divided by the loadings of pure water, both compared at the same partial fugacity in the bulk fluid phase. The calculations are for (a) water/methanol, (b) water/ethanol, (c) water/1-propanol, (d) water/benzene, (e) water/methanol/ethanol/1-propanol, and (f) water/methanol/ethanol/benzene mixtures.

Figure 26. Adsorption selectivties for equimolar water/benzene, methanol/benzene, ethanol/benzene, and methanol/ethanol, and acetone/benzene mixtures in TetZB at 298 K determined from IAST calculations using the pure component isotherm data fit parameters presented in Table 5.

Figure 27. (a, b, c) Comparing the RDFs for $H_{benzene}$-$O_{molecule}$ and $H_{molecule}$-$O_{molecule}$ distances for (a) water/benzene, (b) methanol/benzene, and (c) ethanol/benzene mixtures in CuBTC at 298 K and total fluid fugacity of 1000 Pa. (d) Comparing the RDFs for $H_{molecule}$-$O_{molecule}$ distances for quaternary watermethanol/ethanol/benzene mixtures in CuBTC at 298 K and total fluid fugacity of 1000 Pa.

Figure 28. Comparing the RDFs for $H_{benzene}$-$O_{molecule}$ distances for (a) water/benzene, (b) methanol/benzene, (c) ethanol/benzene, and (d) acetone/benzene mixtures in CuBTC at 298 K and five different total fluid fugacity values.

Figure 29. Comparison of RDF of $H_{molecule}$-$O_{molecule}$ distances for (a) water, (b) methanol, and (c) ethanol at 300 K in ZIF-8, LTA, FAU, DDR, and MFI. These data are from Krishna and van Baten.[17]

Figure 30. (a) Comparison of the CBMC simulation data for component loading, q_1, of ethanol in ethanol/benzene mixture with dual-Langmuir fits using the parameters specified in Table 6. (b) Comparison of the CBMC simulation data for total mixture loading, q_t, with dual-Langmuir fits using the parameters specified in Table 6.

Figure 31. Activity coefficients of the components in the adsorbed phase for equimolar (a) water/benzene, (b) methanol/benzene, (c) ethanol/benzene, and (d) methanol/ethanol, and (e) acetone/benzene mixtures in CuBTC at 298 K.

Figure 32. Correction factor $\left(1-\exp\left(-C\frac{\pi A}{RT}\right)\right)$ for ethanol/benzene mixture adsorption in CuBTC at 298 K. These calculations are based on the equation (22) taking Λ_{12} = 1; Λ_{21}= 3.6; C = 0.12 kg mol^{-1}.

Figure 33. (a, b) Comparison of CBMC simulations for equimolar (a) ethanol/benzene, and (b) methanol/ethanol mixtures in CuBTC at 298 K with RAST calculations. (c, d) RAST calculations of the activity coefficients for equimolar (a) ethanol/benzene, and (b) methanol/ethanol mixtures in CuBTC at 298 K.

Figure 34. CBMC simulations of pure component adsorption isotherms for water, methanol, and ethanol in all-silica FAU zeolite at 300 K. The CBMC data are from Krishna and van Baten.[17] The continuous solid lines are the Dual-Langmuir-Freundlich fits using the parameters specified in Table **7**.

Figure 35. (a) CBMC simulations for adsorption of equimolar (f_1=f_2) water/methanol mixture in FAU zeolite at 300 K. The continuous solid lines are the IAST calculations using the pure component fits in Table **7**. (b, c) CBMC simulations of the enhancement of (b) water, and (c) methanol ingress in FAU, compared with IAST calculations. The enhancement factor is defined as the loading the mixture divided by the loadings of pure component determined at the same partial fugacity in the bulk fluid phase. (d) Activity coefficients γ_i, for water and methanol.

Figure 36. (a) CBMC simulations for adsorption of water/methanol mixtures in FAU zeolite at 300 K at a constant total fugacity of 1000 Pa. The continuous solid lines are the IAST calculations using the pure component fits in Table **7**. (b, c) CBMC simulations of the enhancement of (b) water, and (c) methanol

ingress in FAU, compared with IAST calculations. The enhancement factor is defined as the loading the mixture divided by the loadings of pure component determined at the same partial fugacity in the bulk fluid phase. (d) Activity coefficients γ_i, for water and methanol as a function of mole fraction of water in the bulk fluid phase.

Figure 37. (a) CBMC simulations for adsorption of equimolar (f_1=f_2) water/ethanol mixture in FAU zeolite at 300 K. The continuous solid lines are the IAST calculations using the pure component fits in Table **7**. (b, c) CBMC simulations of the enhancement of (c) water, and (b) ethanol ingress in FAU, compared with IAST calculations. The enhancement factor is defined as the loading the mixture divided by the loadings of pure component determined at the same partial fugacity in the bulk fluid phase. (d) Activity coefficients γ_i, for water and ethanol.

Figure 38. CBMC simulations of pure component adsorption isotherms for water, methanol, and ethanol in all-silica DDR zeolite at 300 K. The CBMC data are from Krishna and van Baten.[17] The continuous solid lines are the Dual-Langmuir-Freundlich fits using the parameters specified in Table **8**.

Figure 39. (a) CBMC simulations for adsorption of equimolar (partial fugacities f_1=f_2) water/methanol mixture in DDR zeolite at 300 K. The continuous solid lines are the IAST calculations using the pure component fits in Table 8. (b, c) CBMC simulations of the enhancement of (b) water, and (c) methanol ingress in DDR, compared with IAST calculations. The enhancement factor is defined as the loading the mixture divided by the loadings of pure component determined at the same partial fugacity in the bulk fluid phase. (d) Activity coefficients γ_i, for water and methanol.

Figure 40. (a) CBMC simulations for adsorption of equimolar (partial fugacities f_1=f_2) water/ethanol mixture in DDR zeolite at 300 K. The continuous solid lines are the IAST calculations using the pure component fits in Table 8. (b, c) CBMC simulations of the enhancement of (c) water, and (b) ethanol ingress in DDR, compared with IAST calculations. The enhancement factor is defined as the loading the mixture divided by the loadings of pure component determined at the same partial fugacity in the bulk fluid phase. (d) Activity coefficients γ_i, for water and ethanol.

Figure 41. CBMC simulations of pure component adsorption isotherms for water, methanol, and ethanol in all-silica MFI zeolite at 300 K. The CBMC data are from Krishna and van Baten.[17] The continuous solid lines are the Dual-Langmuir-Freundlich fits using the parameters specified in Table **9**.

Figure 42. (a) CBMC simulations for adsorption of equimolar (partial fugacities f_1=f_2) water/methanol mixture in MFI zeolite at 300 K. The continuous solid lines are the IAST calculations using the pure component fits in Table **9**. (b, c) CBMC simulations of the enhancement of (b) water, and (c) methanol ingress in MFI, compared with IAST calculations. The enhancement factor is defined as the loading the mixture divided by the loadings of pure component determined at the same partial fugacity in the bulk fluid phase.

Figure 43. (a) CBMC simulations for adsorption of equimolar (partial fugacities f_1=f_2) water/ethanol mixture in MFI zeolite at 300 K. The continuous solid lines are the IAST calculations using the pure component fits in Table **9**. (b, c) CBMC simulations of the enhancement of (c) water, and (b) ethanol ingress in MFI, compared with IAST calculations. The enhancement factor is defined as the loading the

mixture divided by the loadings of pure component determined at the same partial fugacity in the bulk fluid phase.

Figure 44. Experimental data of Farzaneh et al.[30] for (a) butanol/water, and (b) water/butanol selectivities in all-silica MFI zeolite at 308 K. Also shown are the IAST calculations using the unary isotherm fit parameters reported in Table 10. The plotted data points are summarized in Table 11.

Figure 45. (a) CBMC simulations[31] of pure component adsorption isotherms for water, and 1-alcohols in CHA at 300 K. Table **12** provides the pure component isotherm fit parameters. (b) Saturation capacities for adsorption of 1-alcohols in CHA at 300 K. (c) Snapshots showing the conformations of 1-alcohols in CHA at saturation conditions.

Figure 46. (a) CBMC simulations for adsorption of equimolar (partial fugacities f_1=f_2) methanol/ethanol mixture in CHA zeolite at 300 K. The continuous solid lines are the IAST calculations using the pure component fits in Table **12**. (b, c) CBMC simulations of the enhancement of (b) water, and (c) methanol ingress in CHA, compared with IAST calculations. The enhancement factor is defined as the loading the mixture divided by the loadings of pure component determined at the same partial fugacity in the bulk fluid phase. (d) Activity coefficients γ_i, for methanol and ethanol.

Figure 47. CBMC mixture simulations for (a) ethanol - 1-propanol, (b) ethanol -1-hexanol mixtures in CHA at 300 K. The partial fugacities in the bulk fluid phase are taken to be equal, i.e. f_1=f_2. The continuous solid lines represent calculations of the Ideal Adsorbed Solution Theory (IAST)[24] using

dual-Langmuir-Freundlich fits of pure component isotherms. Table **12** provides the pure component isotherm fit parameters. (c, d) Activity coefficients for (c) ethanol - 1-propanol, (d) ethanol -1-hexanol mixtures.

Figure 48. Mean-square-deviations for diffusion of water in CuBTC at 298 K, averaged over the x, y, and z directions. The values of the loadings are expressed per unit cell of CuBTC.

Figure 49. Mean-square-deviations for diffusion of methanol in CuBTC at 298 K, averaged over the x, y, and z directions. The values of the loadings are expressed per unit cell of CuBTC.

Figure 50. Mean-square-deviations for diffusion of ethanol in CuBTC at 298 K, averaged over the x, y, and z directions. The values of the loadings are expressed per unit cell of CuBTC.

Figure 51. Mean-square-deviations for diffusion of benzene in CuBTC at 298 K, averaged over the x, y, and z directions. The values of the loadings are expressed per unit cell of CuBTC.

Figure 52. (a) MD simulations of the self-diffusivities $D_{i,self}$ of water in CuBTC at 298 K as a function of the component loading q_i. (b) MD simulations of the self-diffusivities $D_{i,self}$ of water, methanol, ethanol, and benzene as a function of the fractional pore occupancy, θ_i.

Figure 53. Loading dependence of the Maxwell-Stefan diffusivity $Đ_i$, and the inverse thermodynamic factor $1/\Gamma_i$ in CuBTC of (a) n-butane (nC4), (b) iso-butane (iC4), (c) 2,2-dimethylpropane (= neopentane = neoP), and (d) 2-methylbutane (=2MB). The symbols represent $Đ_i$ values backed out from

IRM experiments, and the continuous solid lines are derived from IRM isotherm fits. These data are re-plotted using the information contained in Chmelik et al.[33]

Figure 54. (a) Pore landscape of CuBTC showing the adsorbed neopentane (neo-P) molecules. (b) Snapshot showing the location of neo-pentane lodged within a tetrahedral pocket.

Figure 55. MD simulations of the self-diffusivities $D_{i,self}$, and the inverse thermodynamic factor $1/\Gamma_i$ in CuBTC of (a) water, (b) methanol, (c) ethanol, and (d) benzene as a function of the component loading q_i.

Figure 56. MD simulations of the self-diffusivities $D_{i,self}$, and the inverse thermodynamic factor $1/\Gamma_i$ in CuBTC of (a) water, (b) methanol, (c) ethanol, and (d) benzene as a function of the fractional pore occupancy, θ_i.

Figure 57. (a) Transient desorption profiles for methanol in CuBTC at 298 K. Experimental data of Tsotsalas et al.[22] (b) Comparison of the experimental transient desorption profile with the loading dependence of the self-diffusivity.

Figure ESI 1

CuBTC: atomic structure

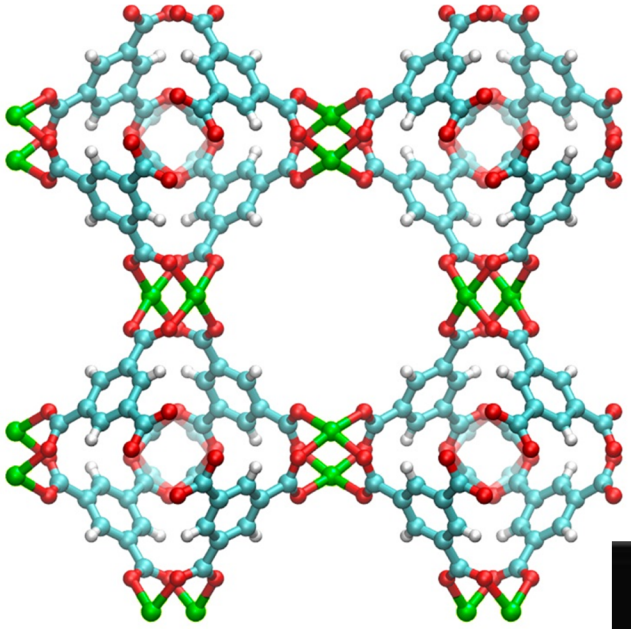

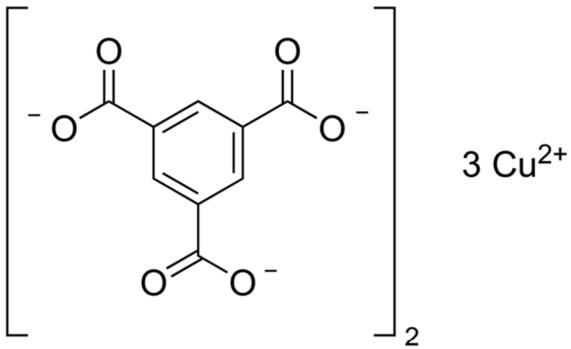

3 Cu^{2+}

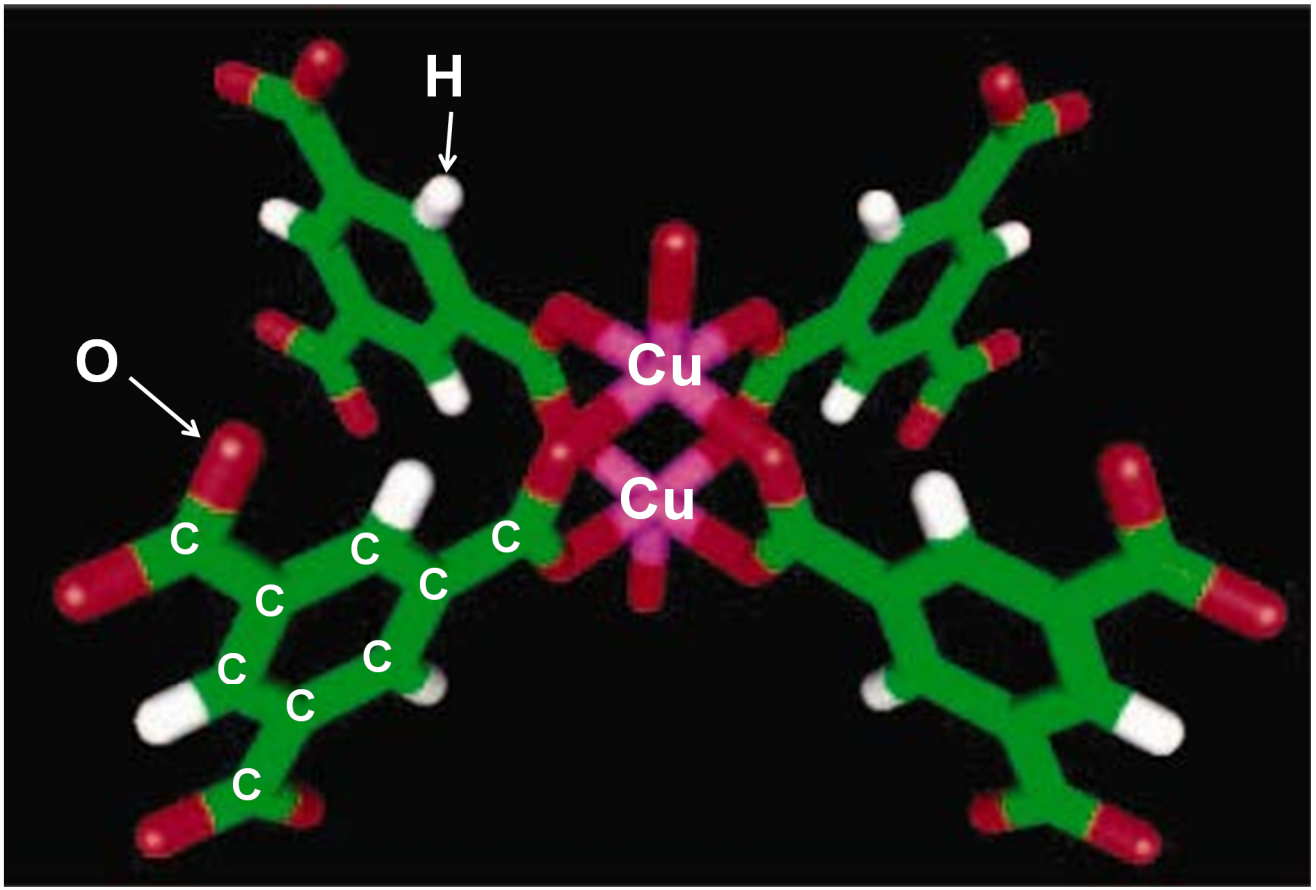

Figure ESI 2

CuBTC framework

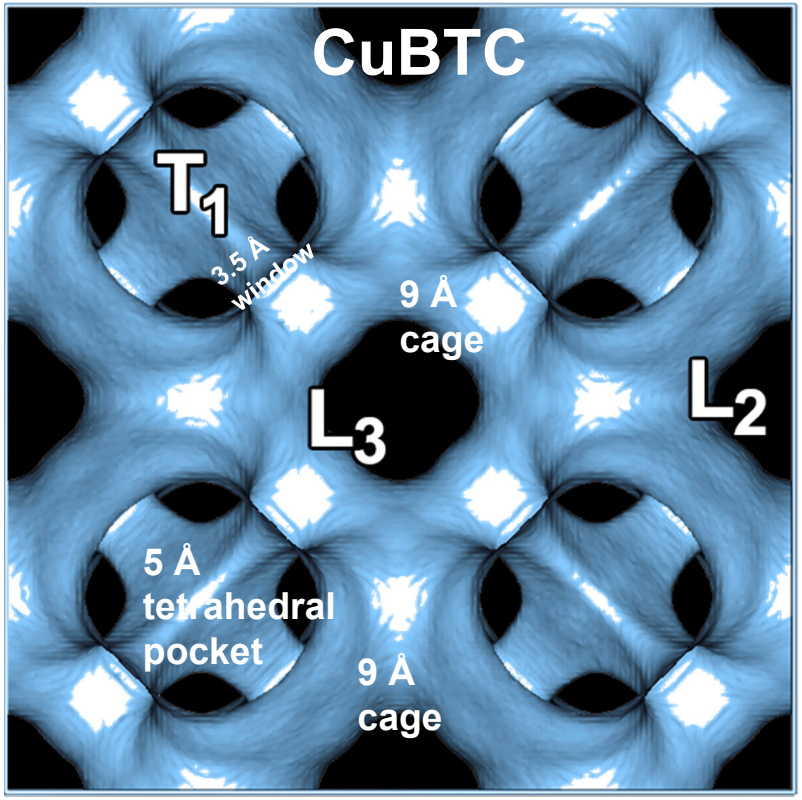

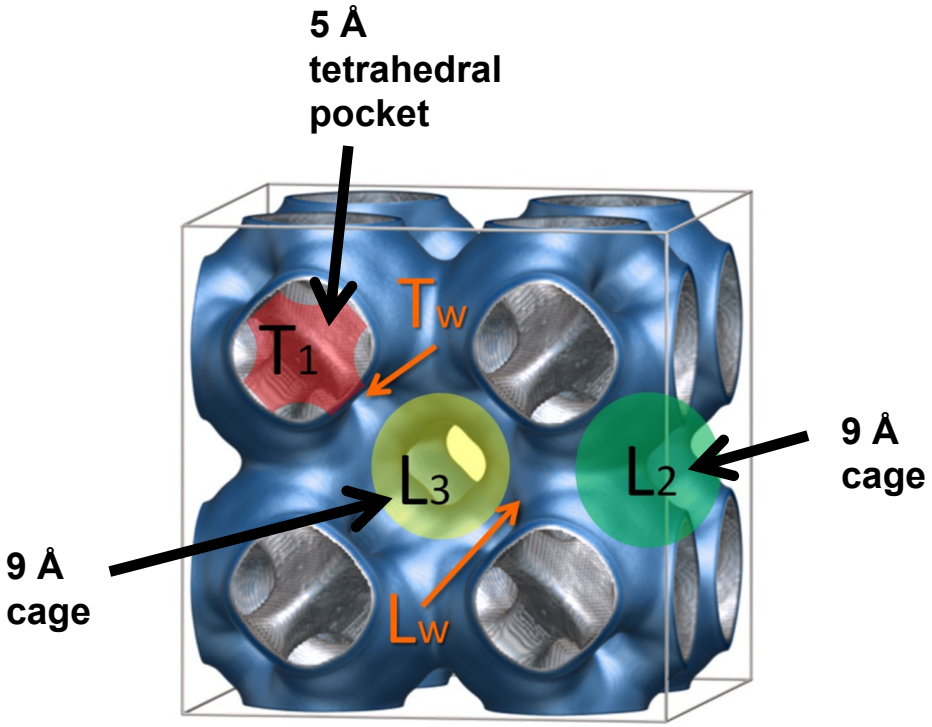

Figure ESI 3

Molar densities of fluids

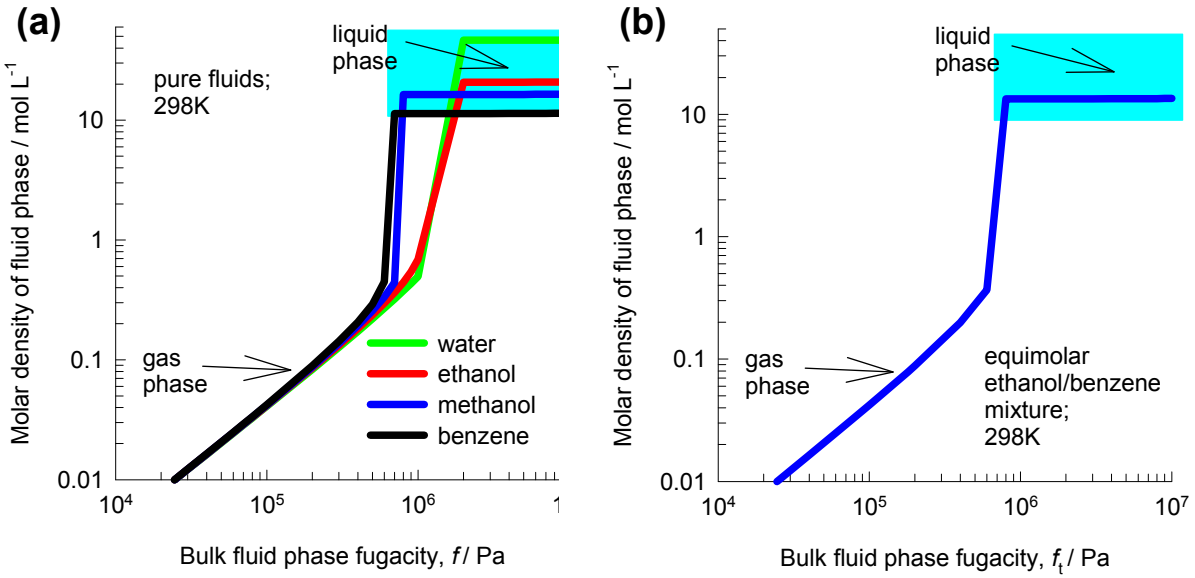

Figure ESI 4

Adsorption of water in CuBTC: validation

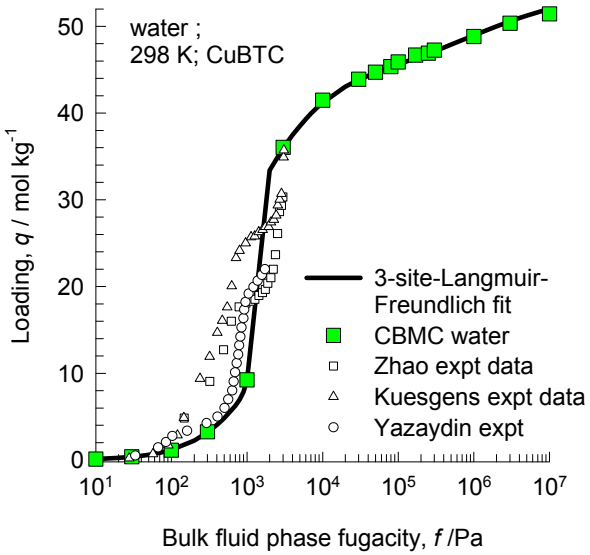

Unary isotherms: water, alcohols, acetone, and benzene in CuBTC

Figure ESI 5

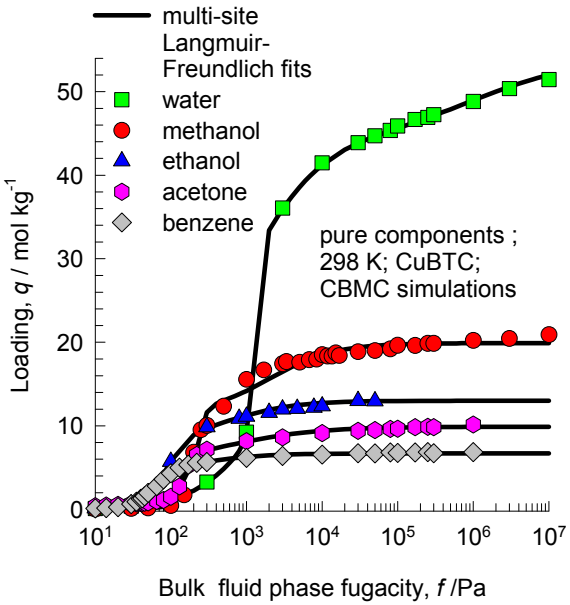

Figure ESI 6

Fractional pore occupancies

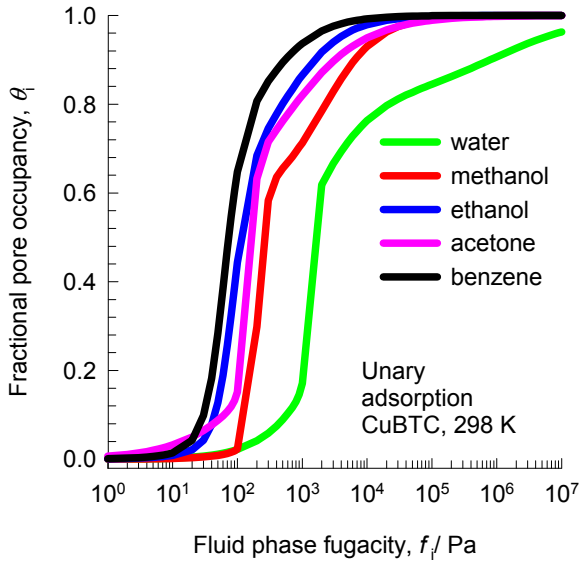

Figure ESI 7

Inverse Thermodynamic Factor

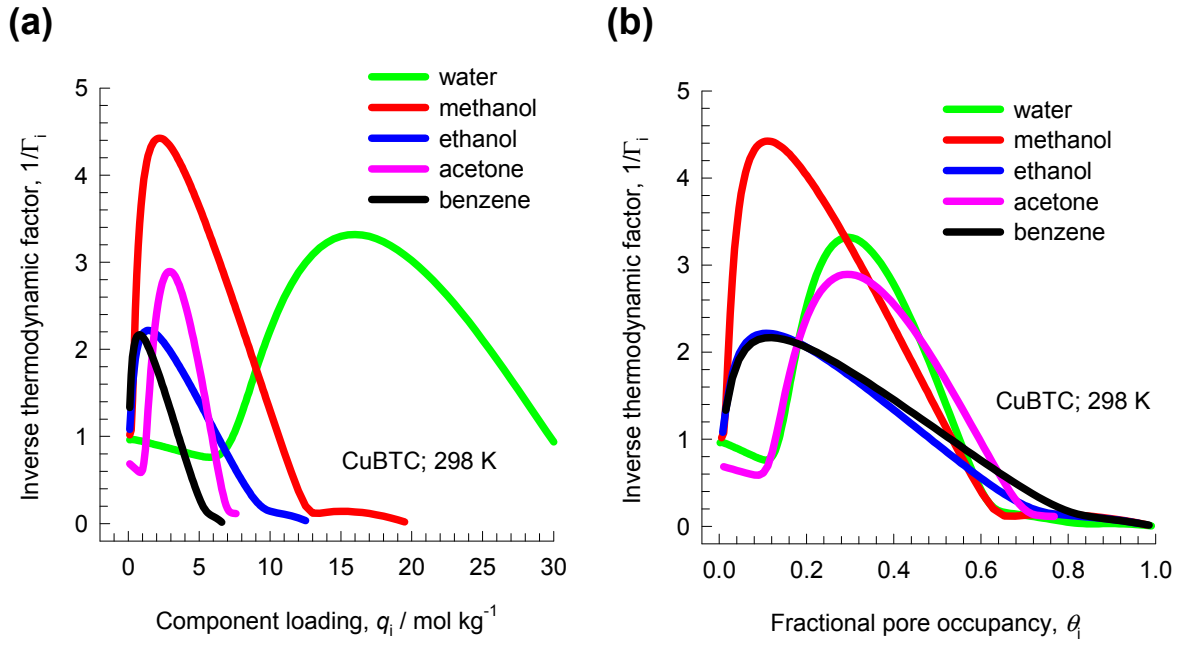

Figure ESI 8

Inverse Thermodynamic Factor: Methanol

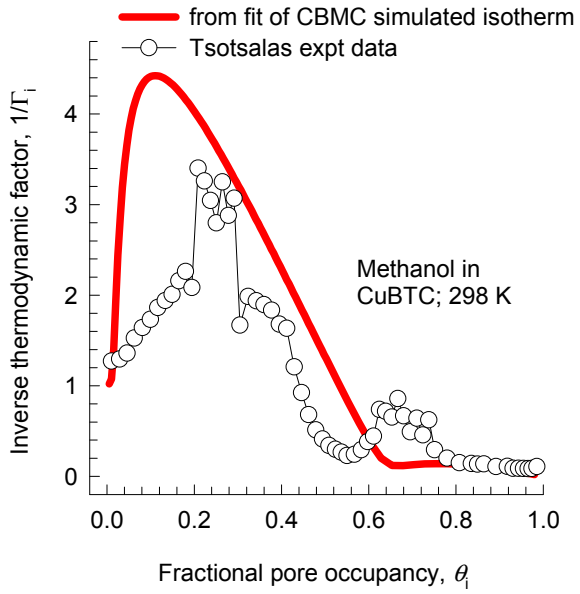

CBMC binary mixture simulations

Figure ESI 9

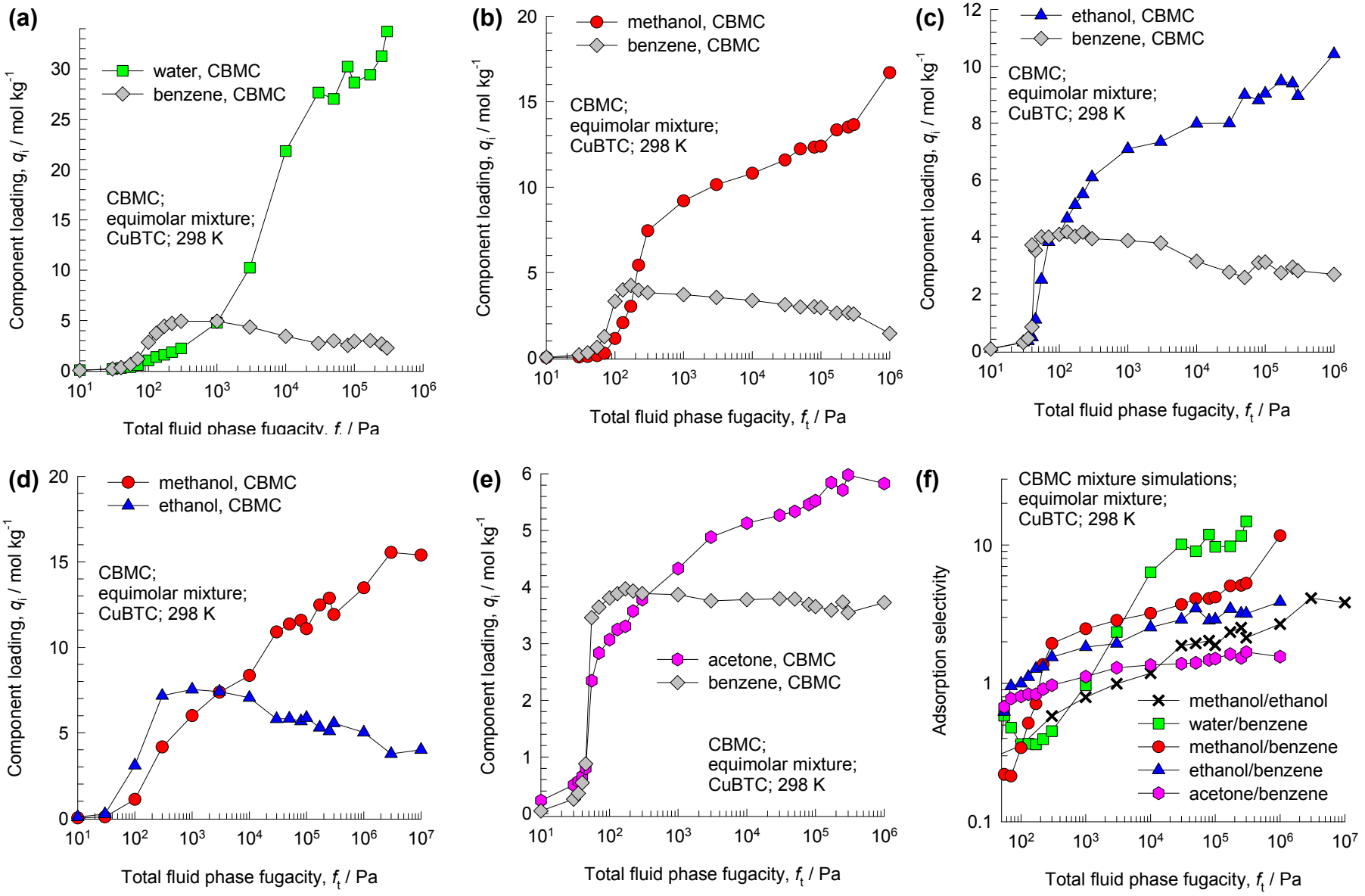

Figure ESI 10

Fractional pore occupancies

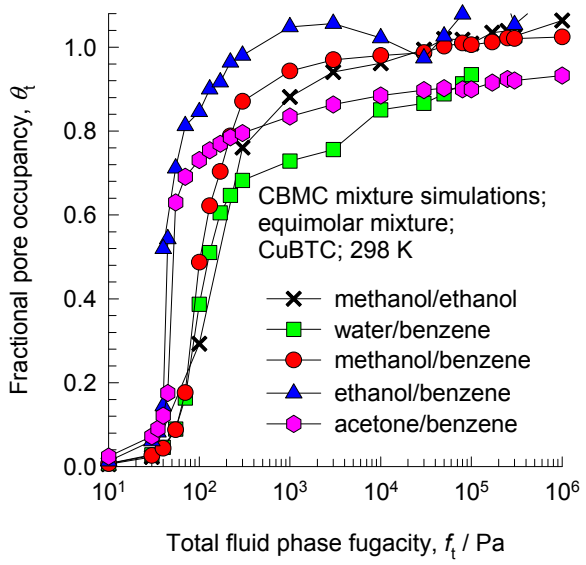

CBMC quaternary mixture simulations

Figure ESI 11

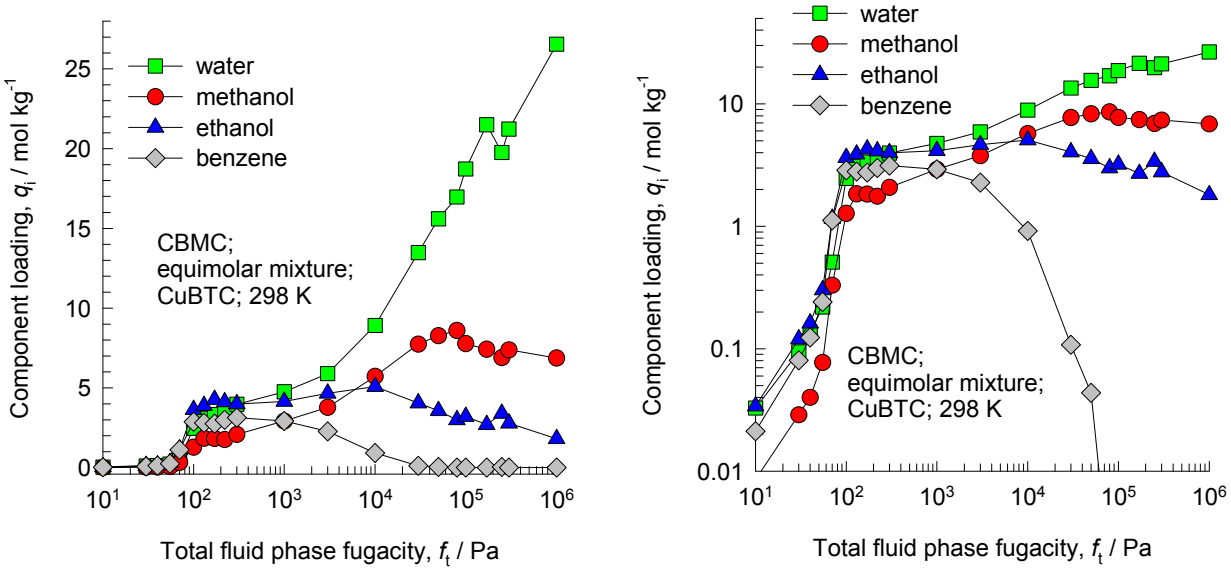

Figure ESI 12

snaps

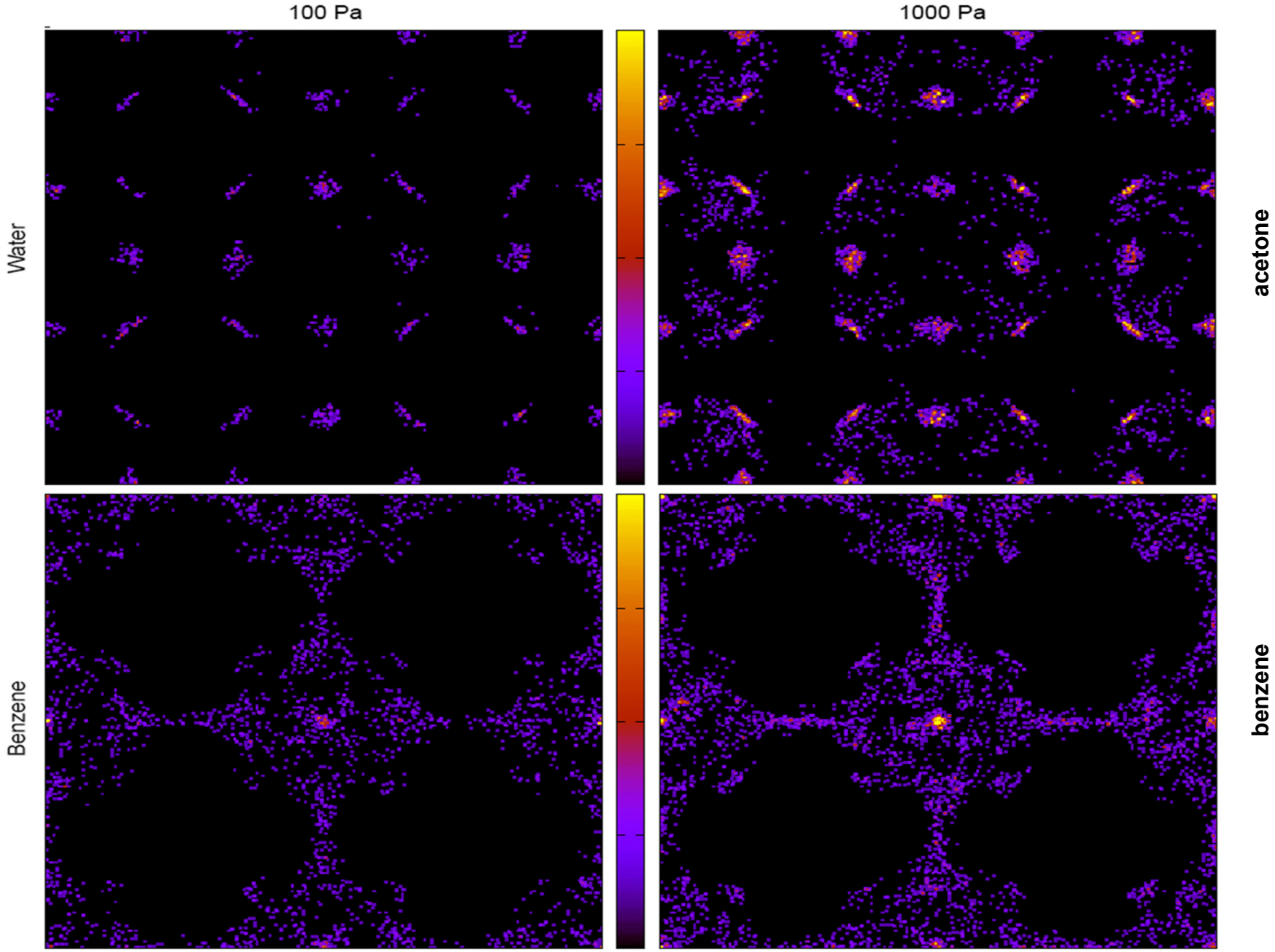

Figure ESI 13

snaps

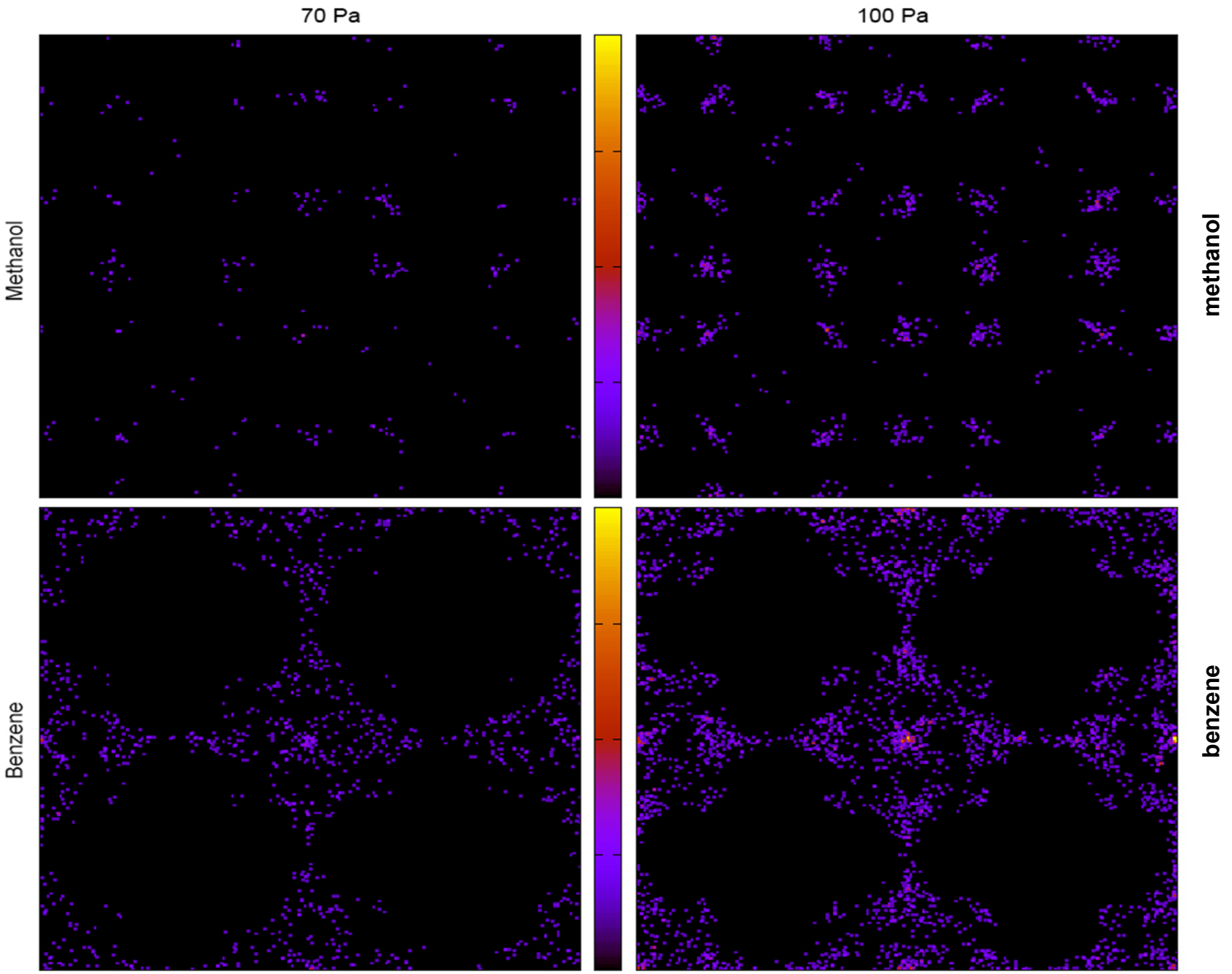

Figure ESI 14

snaps

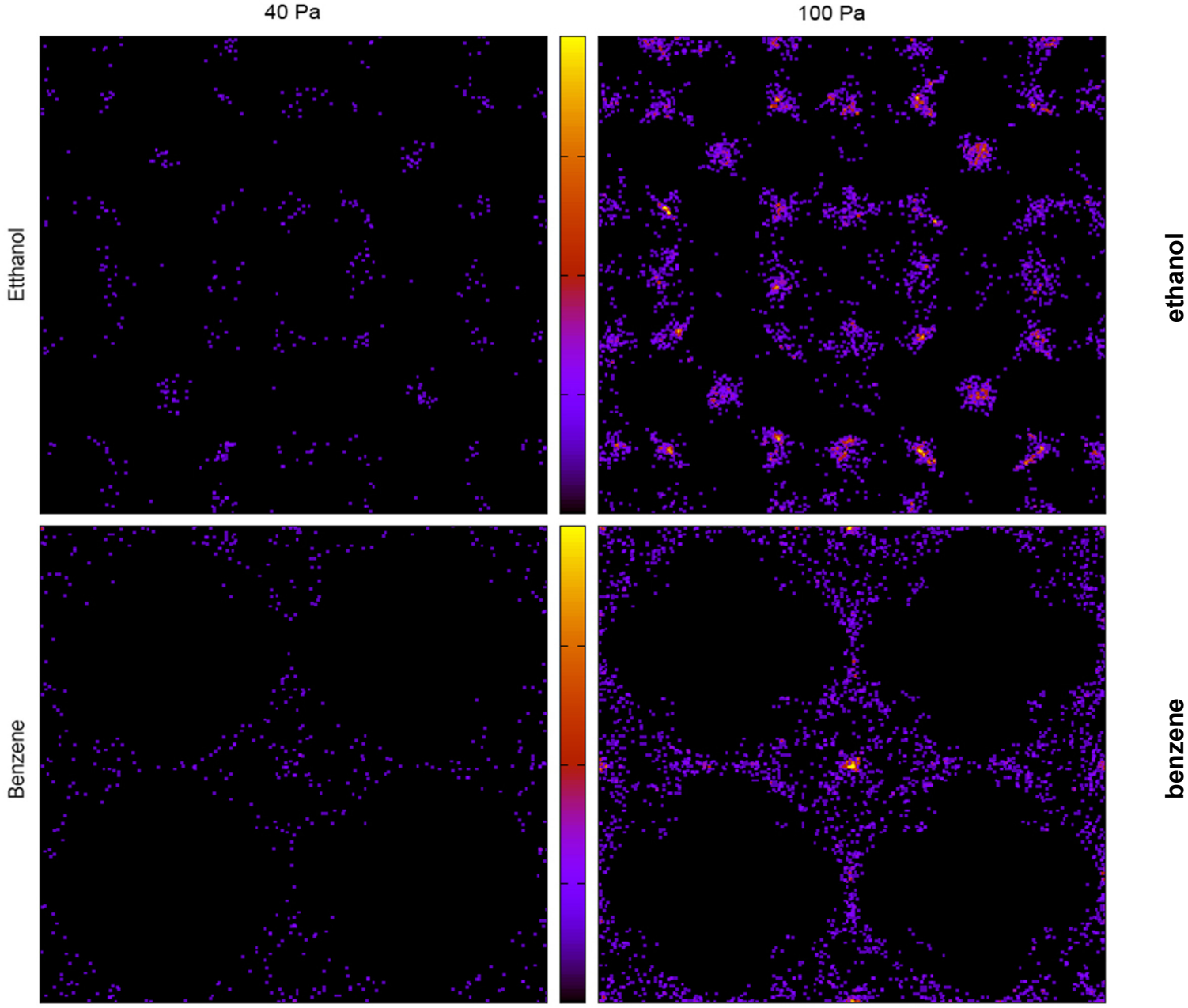

Figure ESI 15

snaps

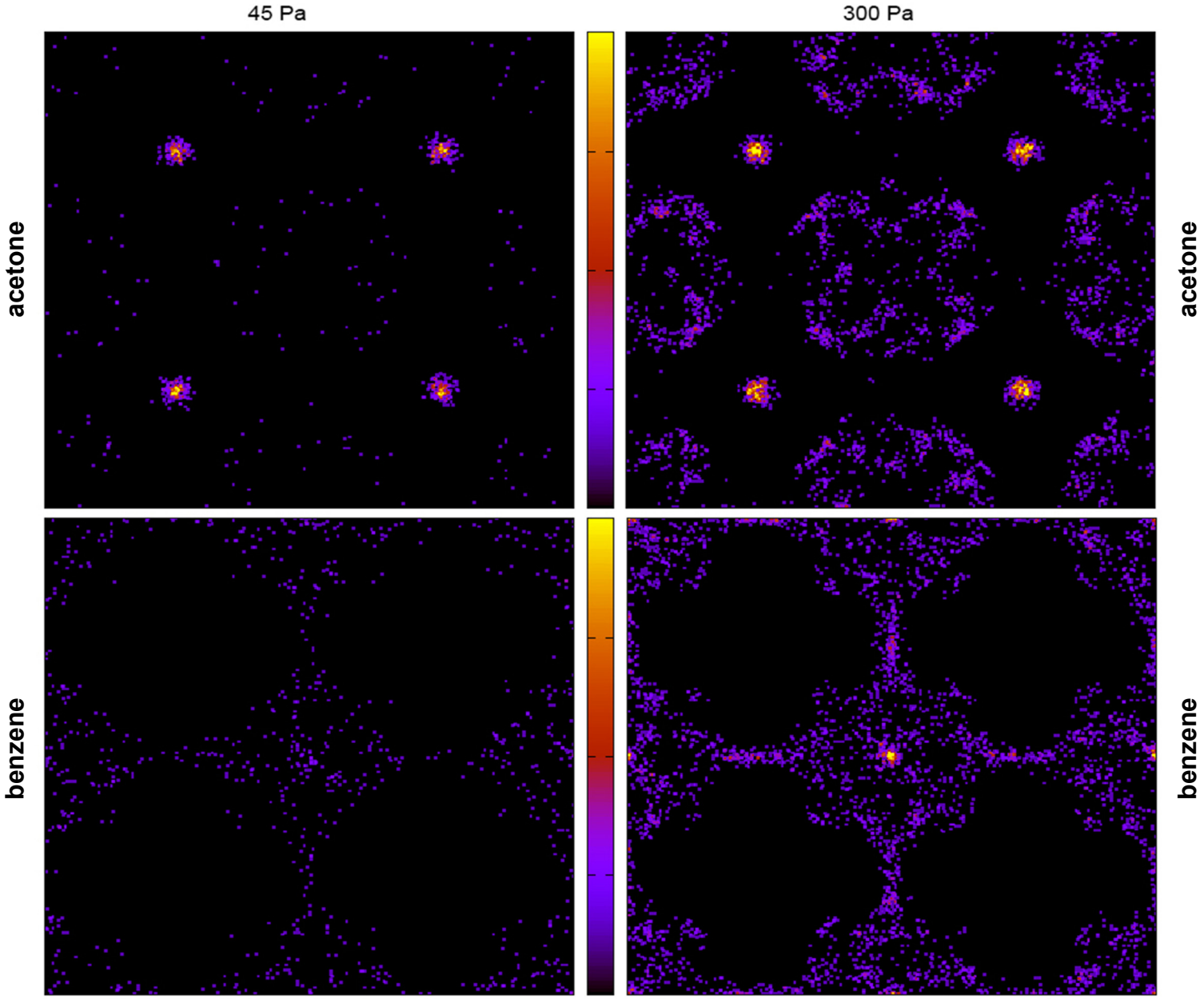

Figure ESI 16

snaps

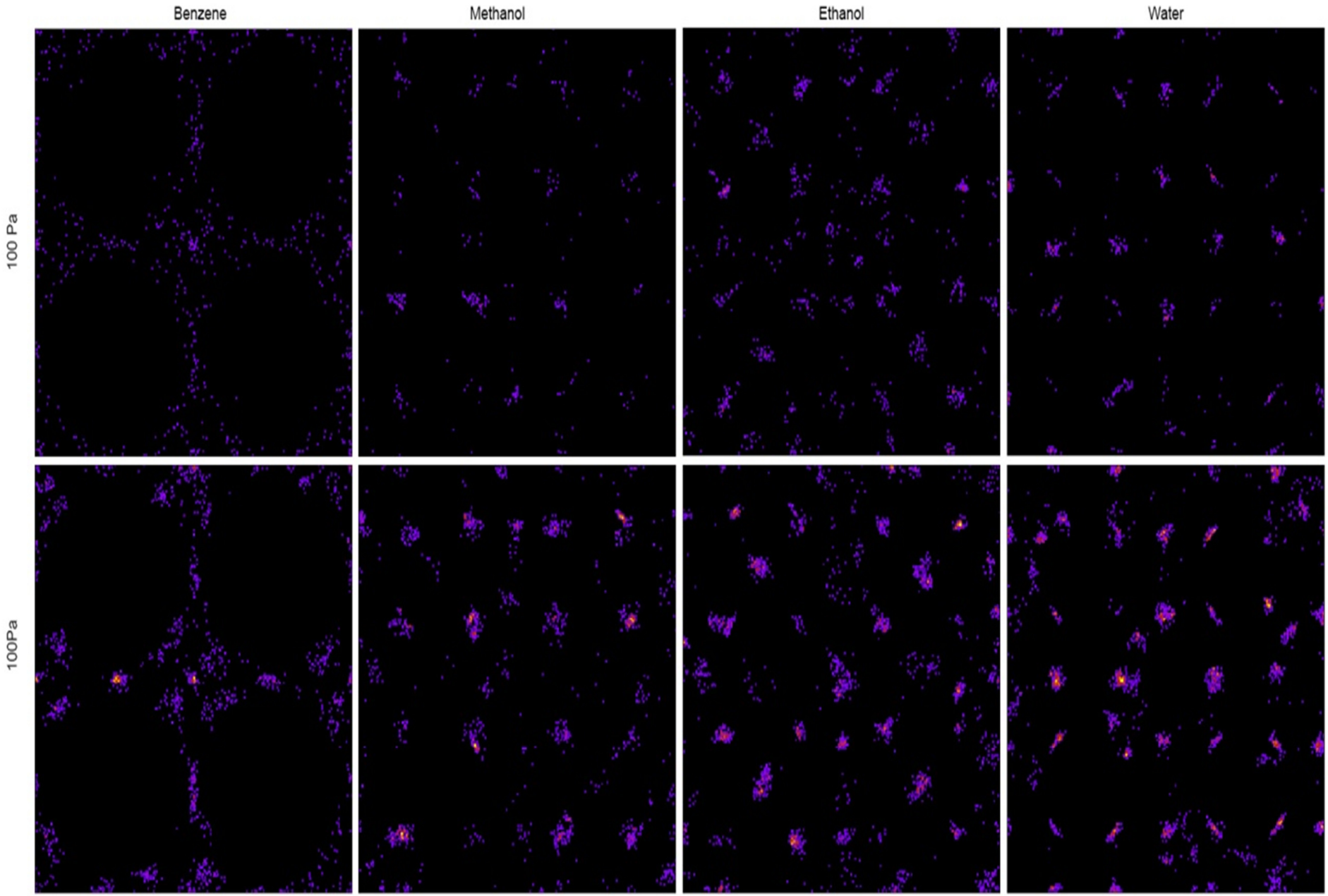

Entropy effects: water adsorption in mixtures

Figure ESI 17

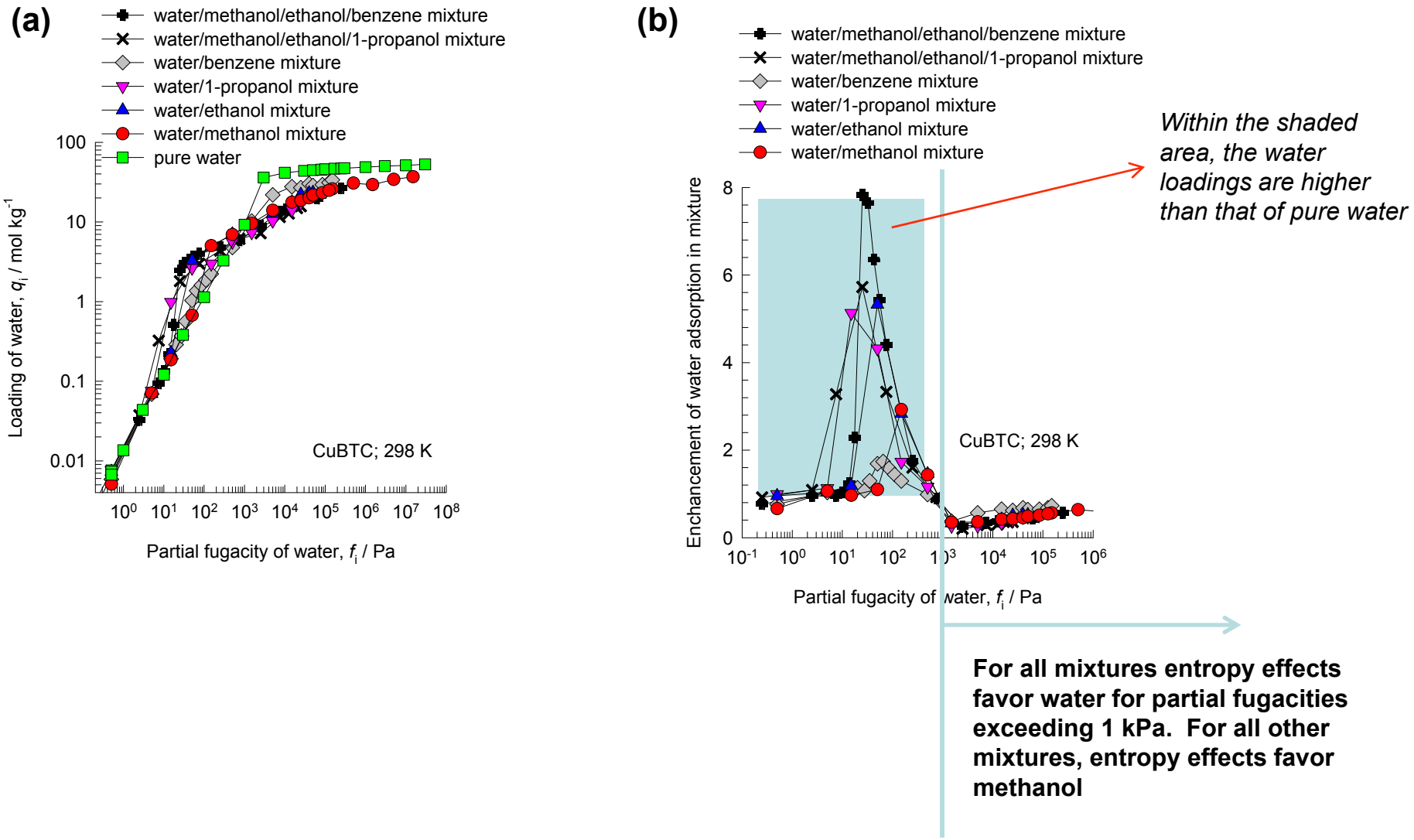

Entropy effects: methanol adsorption in mixtures

Figure ESI 18

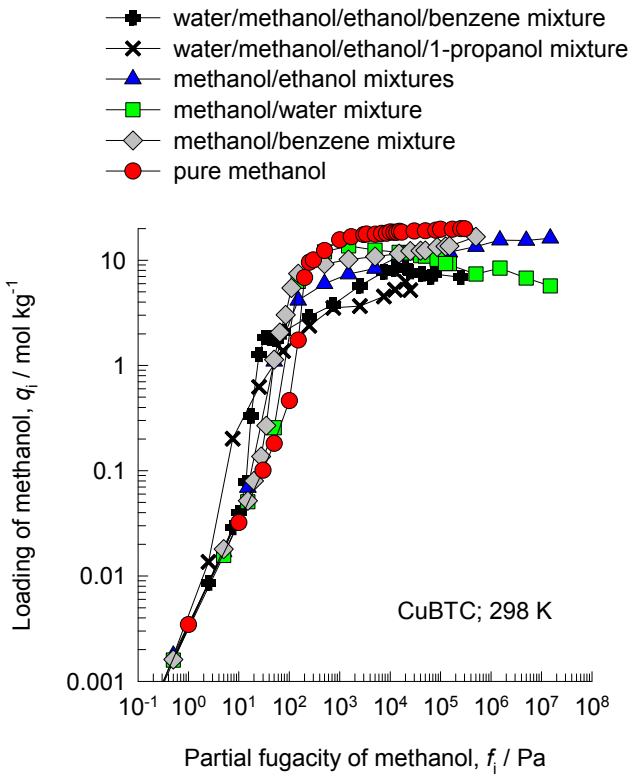

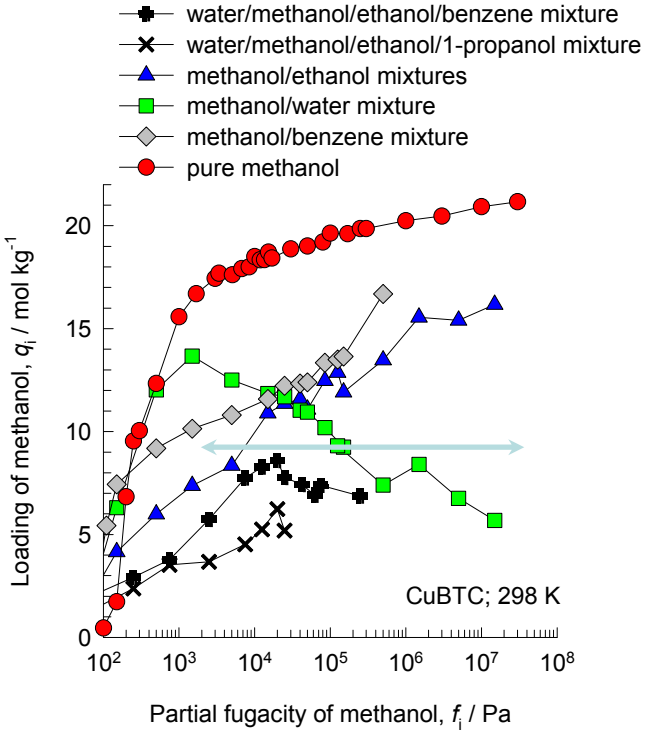

For water/methanol mixtures entropy effects favor water. For all other mixtures, entropy effects favor methanol

Entropy effects: ethanol adsorption in mixtures

Figure ESI 19

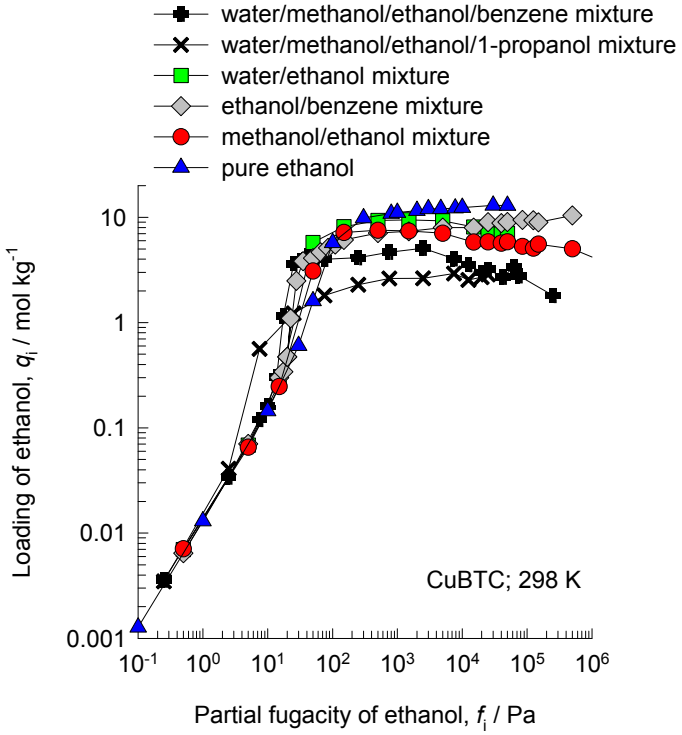

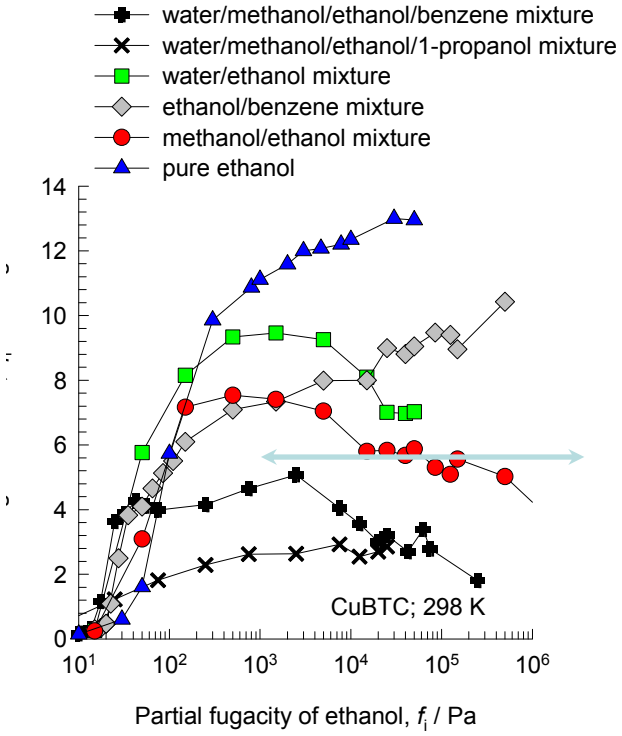

Except for ethanol/benzene mixtures, in this range of partial fugacities, entropy effects cause the ethanol loading in the mixture to reduce in favor of partner molecules

Entropy effects: 1-propanol adsorption in mixtures

Figure ESI 20

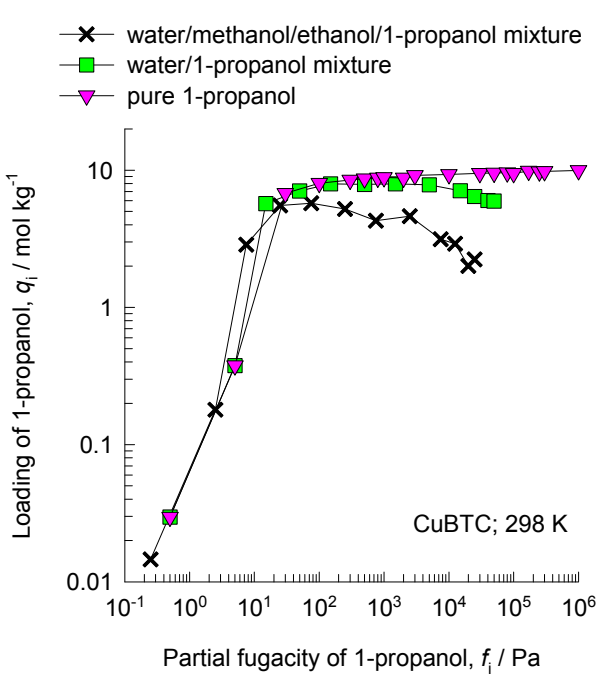

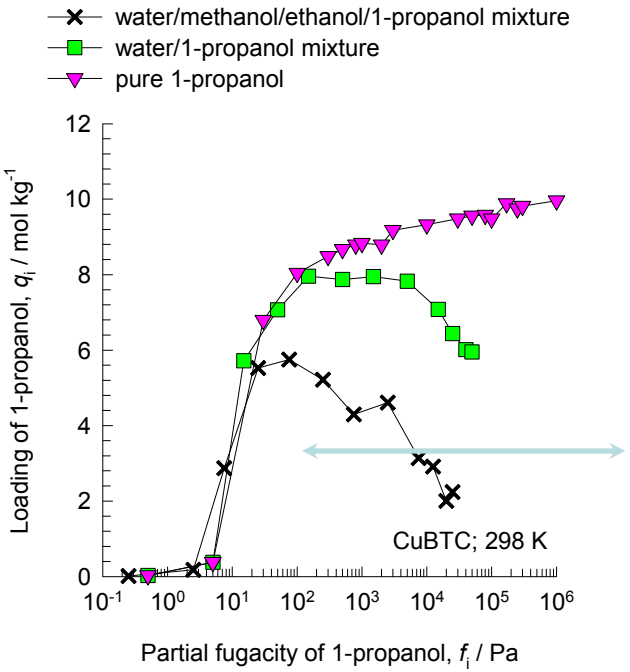

In this range of partial fugacities, entropy effects cause the 1-propanol loading in the mixture to reduce in favor of partner molecules

Entropy effects: benzene adsorption in mixtures

Figure ESI 21

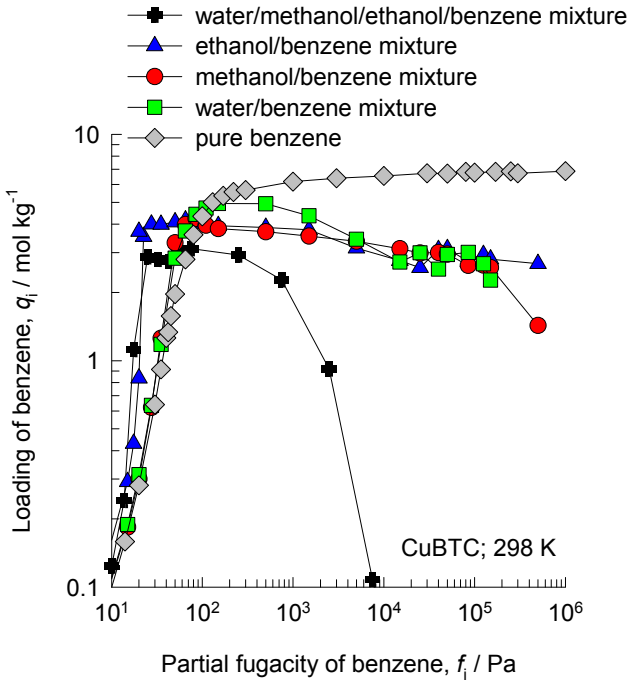

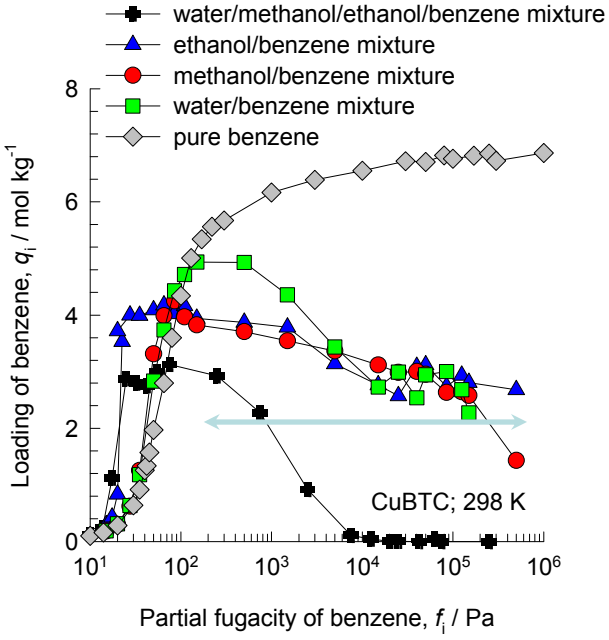

In this range of partial fugacities, entropy effects cause the benzene loading in the mixture to reduce in favor of partner molecules

IAST vs CBMC mixture

Figure ESI 22

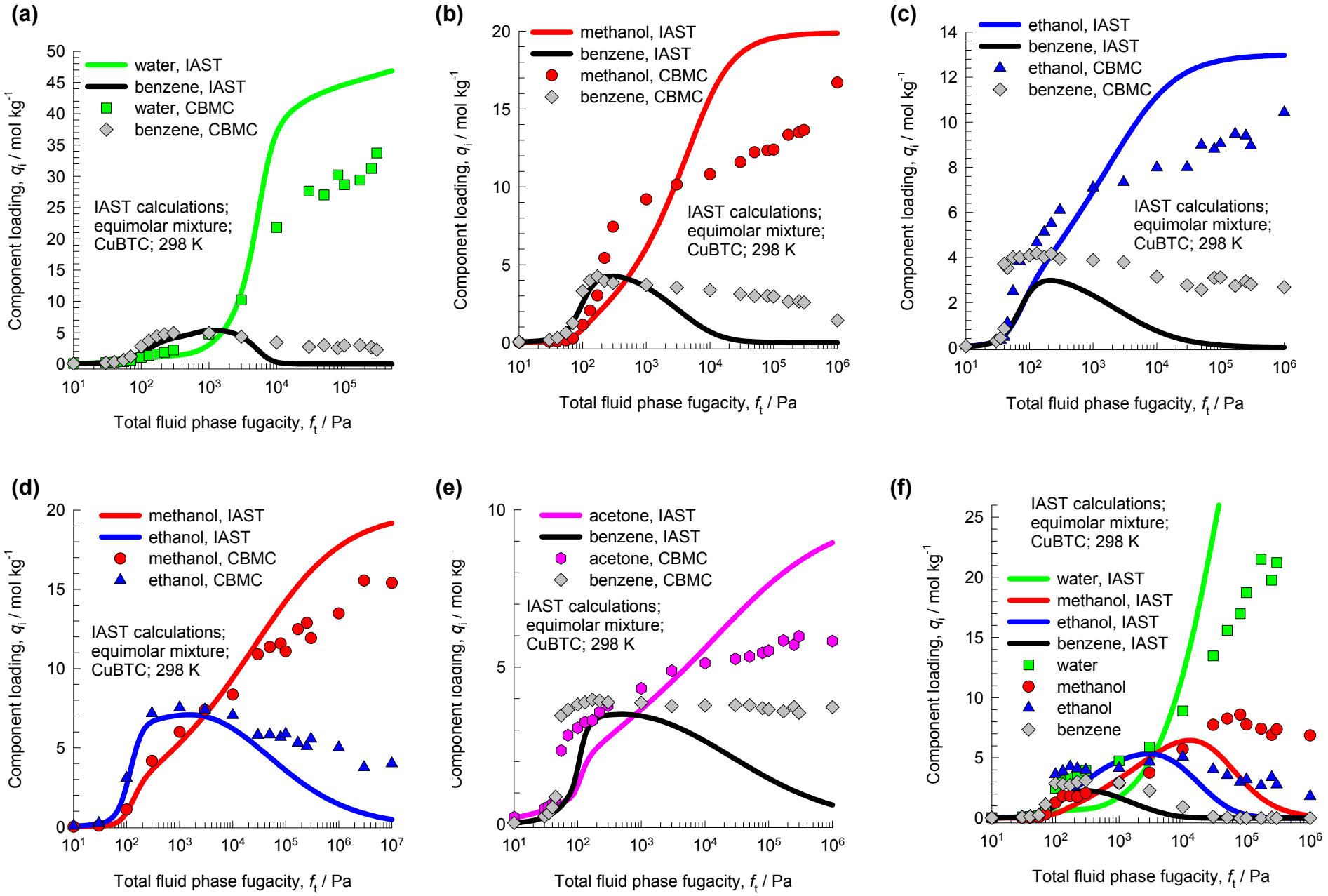

Figure ESI 23

IAST vs CBMC mixture

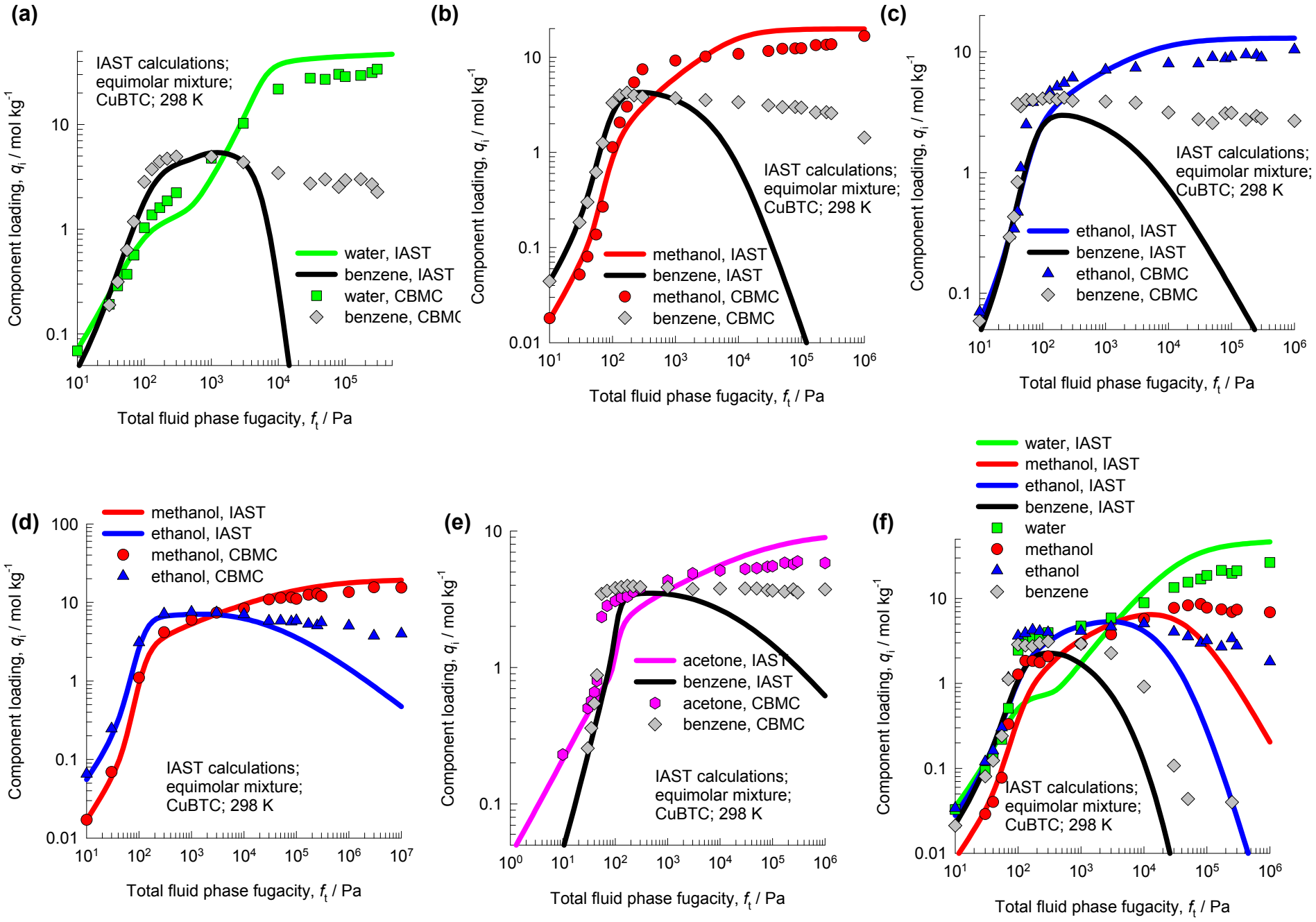

IAST vs CBMC mixture

Figure ESI 24

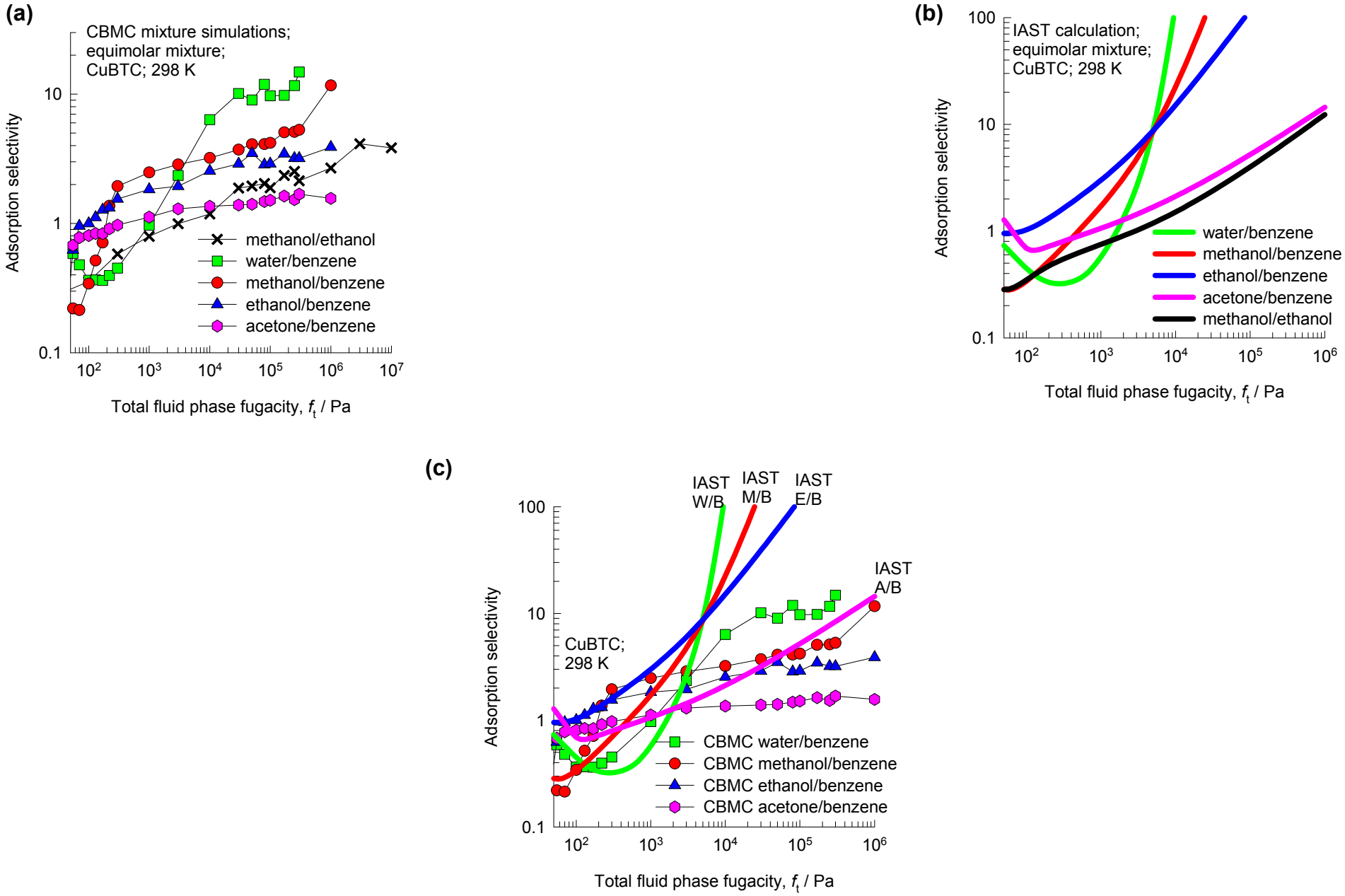

Figure ESI 25

IAST vs CBMC mixture

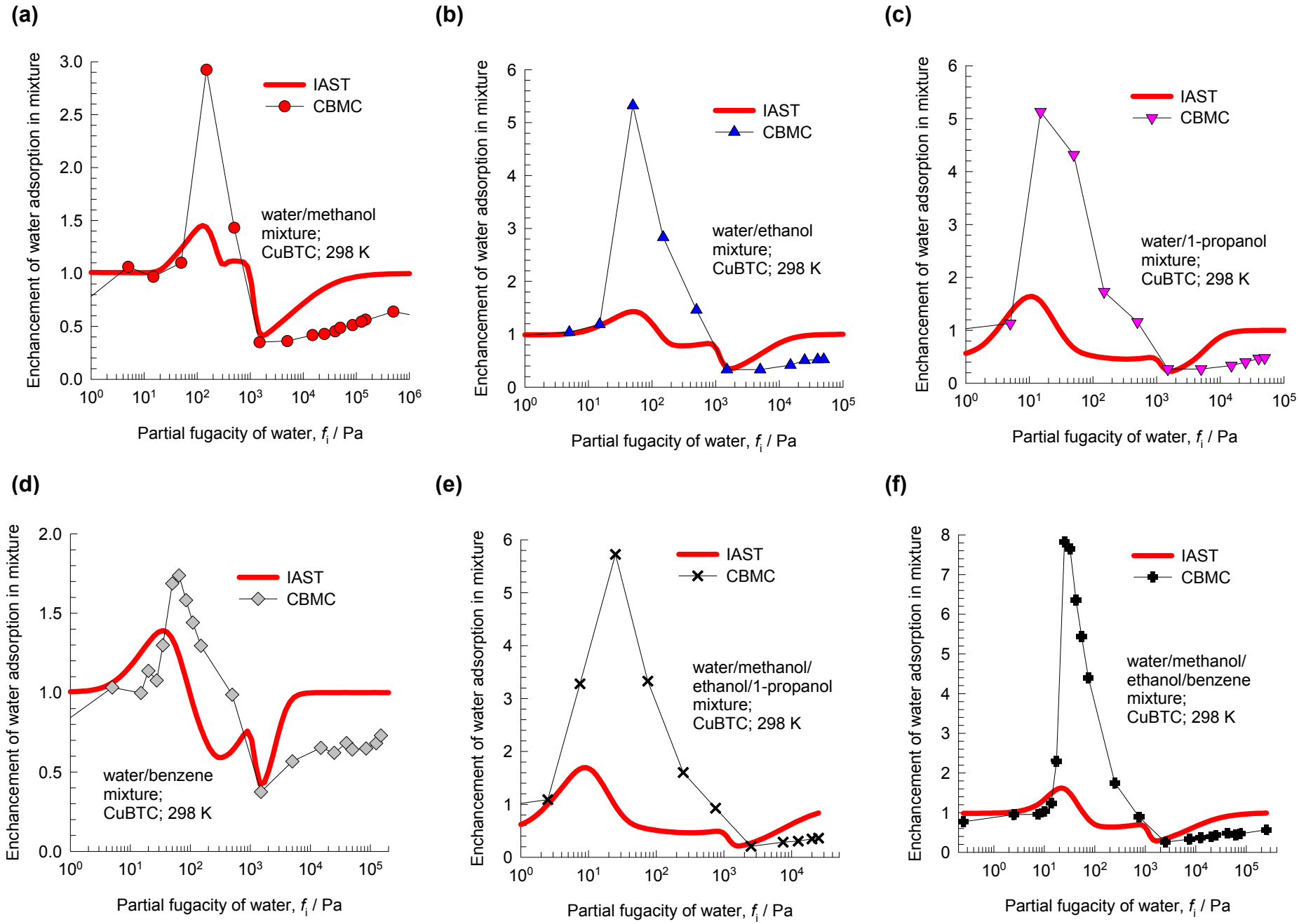

Figure ESI 26

Adsorption selectivities with TetZB

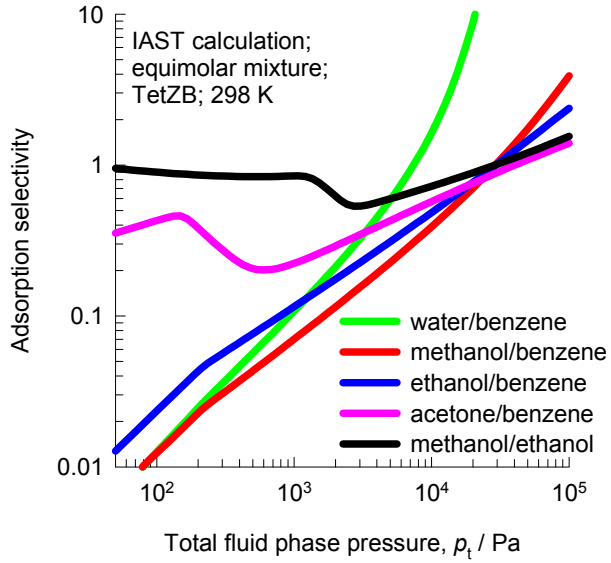

Figure ESI 27

RDF

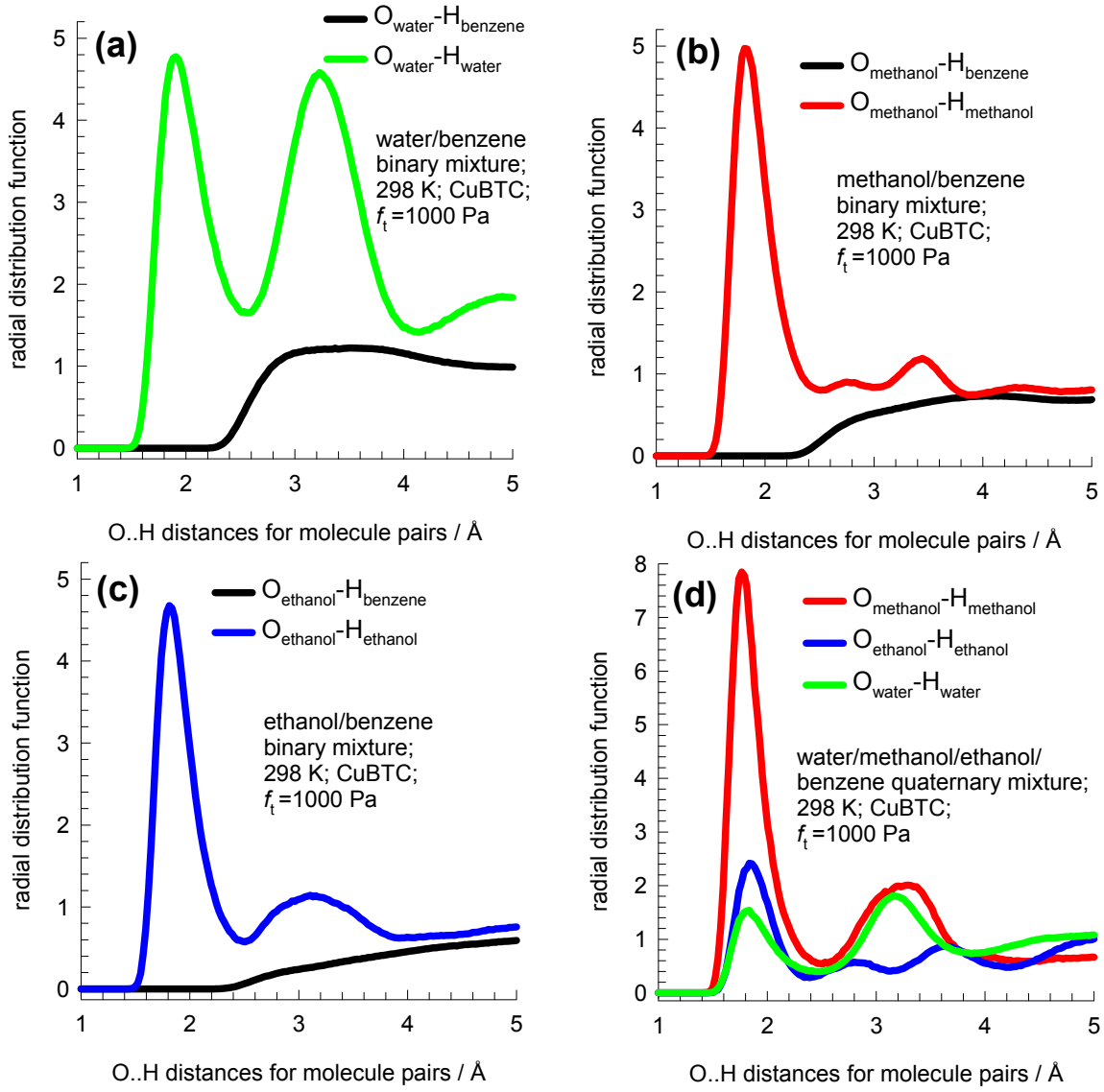

Figure ESI 28

RDF

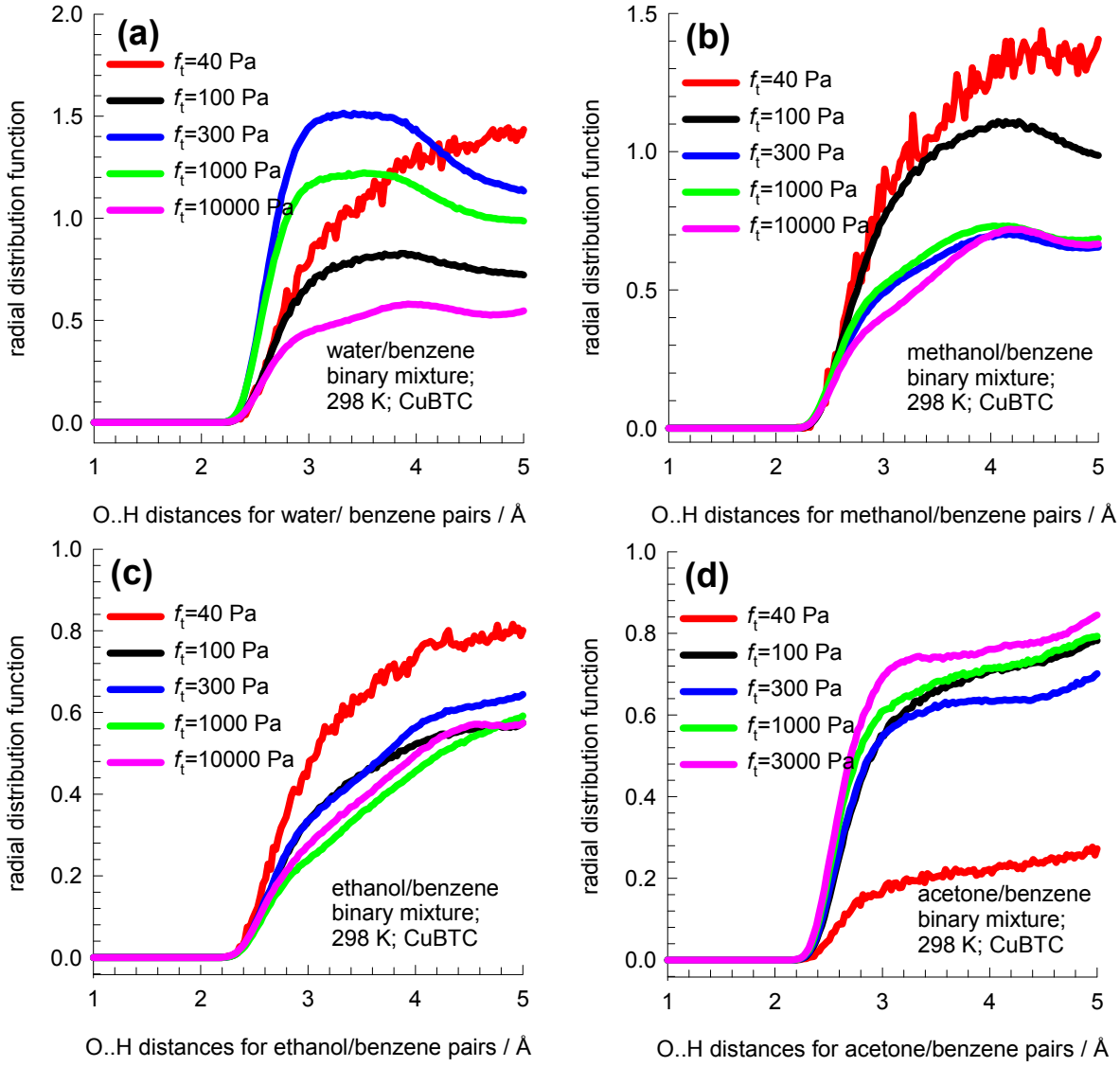

RDF

Figure ESI 29

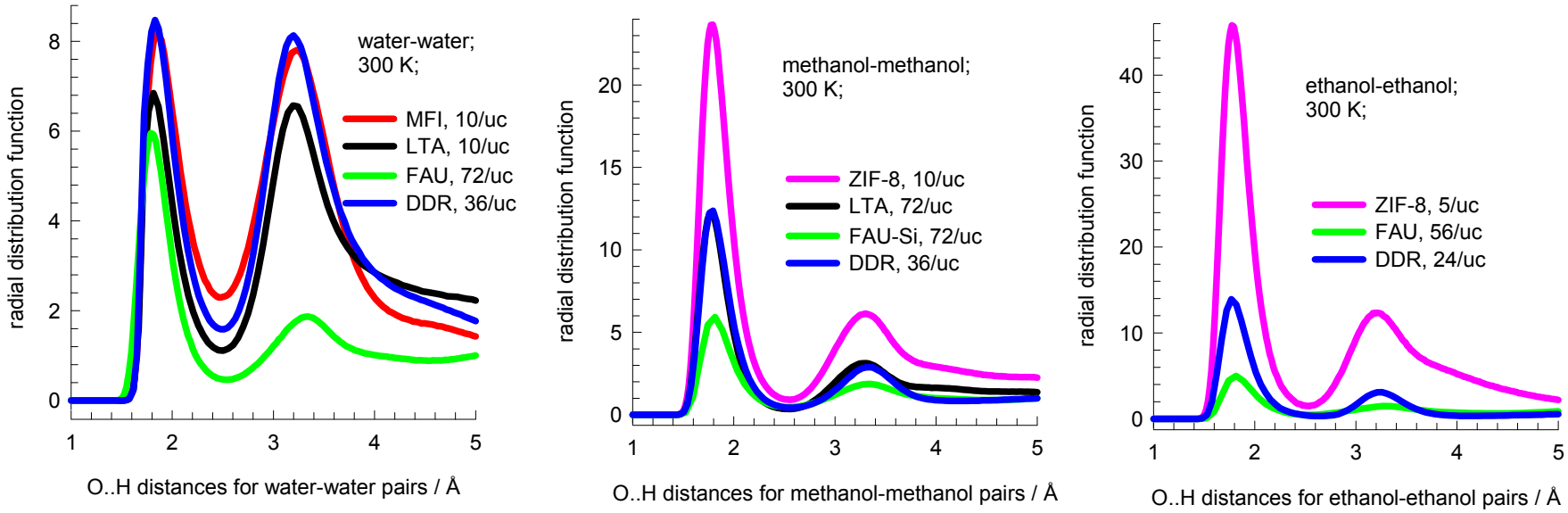

Fitting of CBMC mixture simulation data

Figure ESI 30

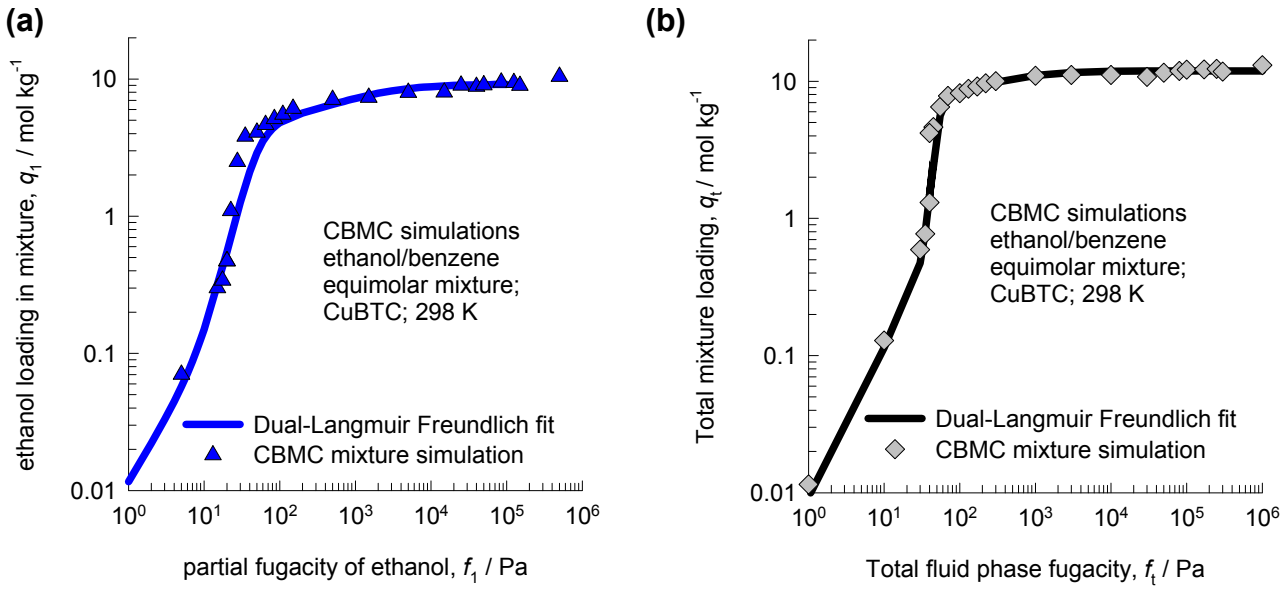

Activity coefficients: Numerical calculations

Figure ESI 31

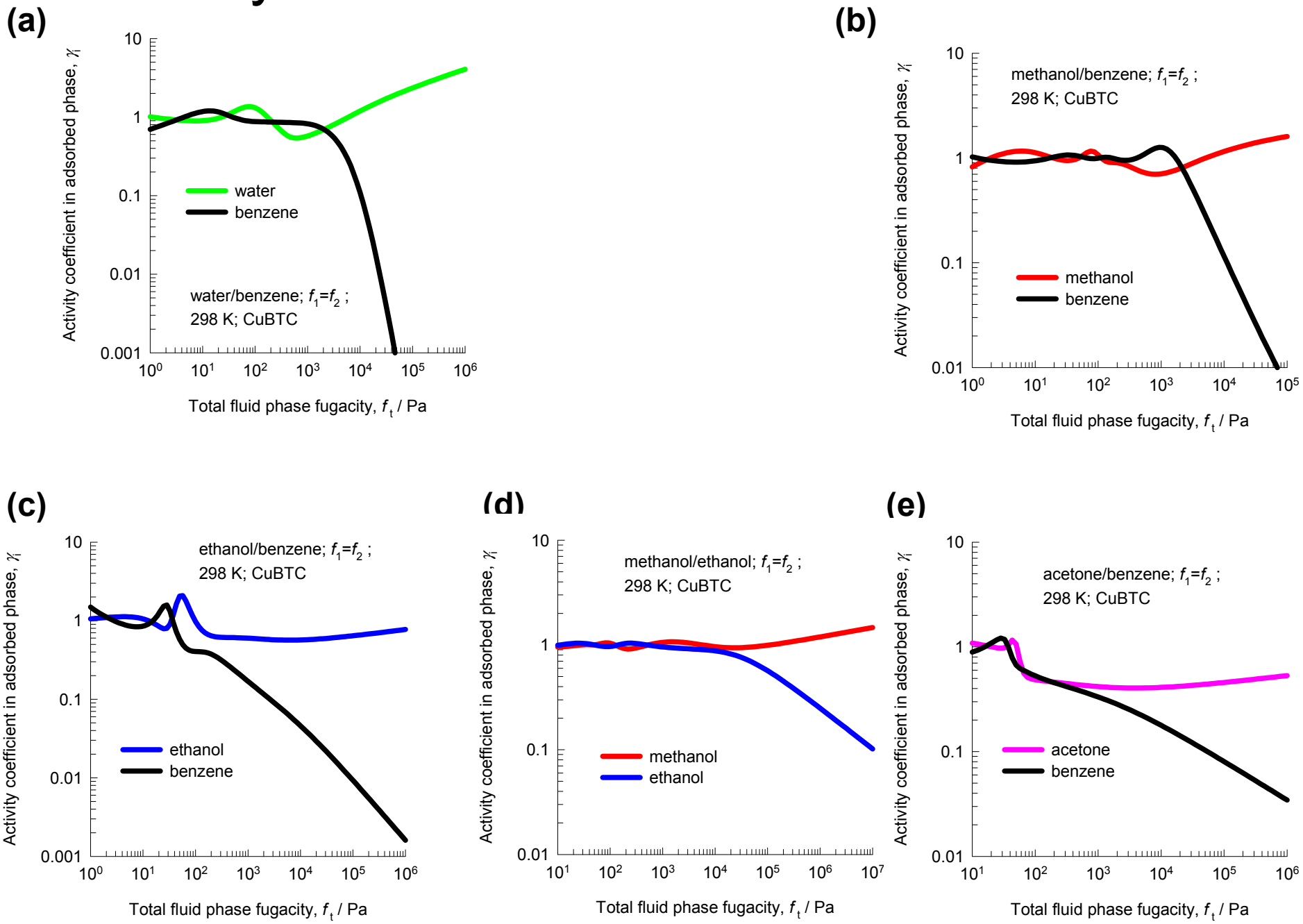

Figure ESI 32

Correction factor

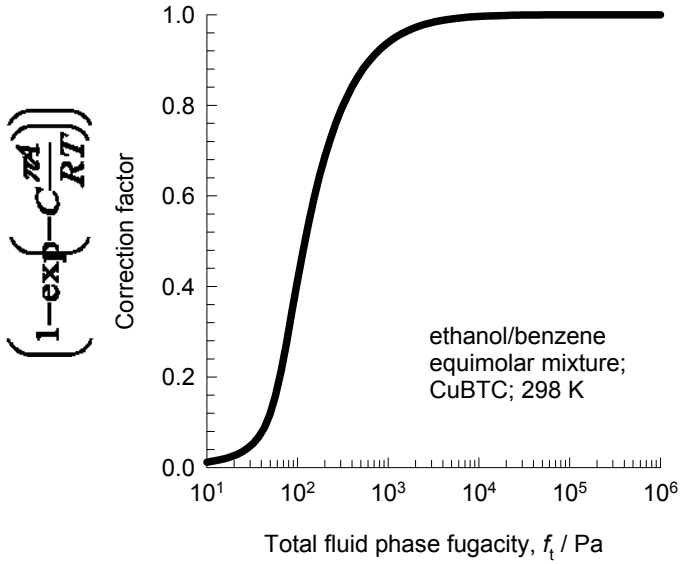

Figure ESI 33

RAST vs CBMC mixture

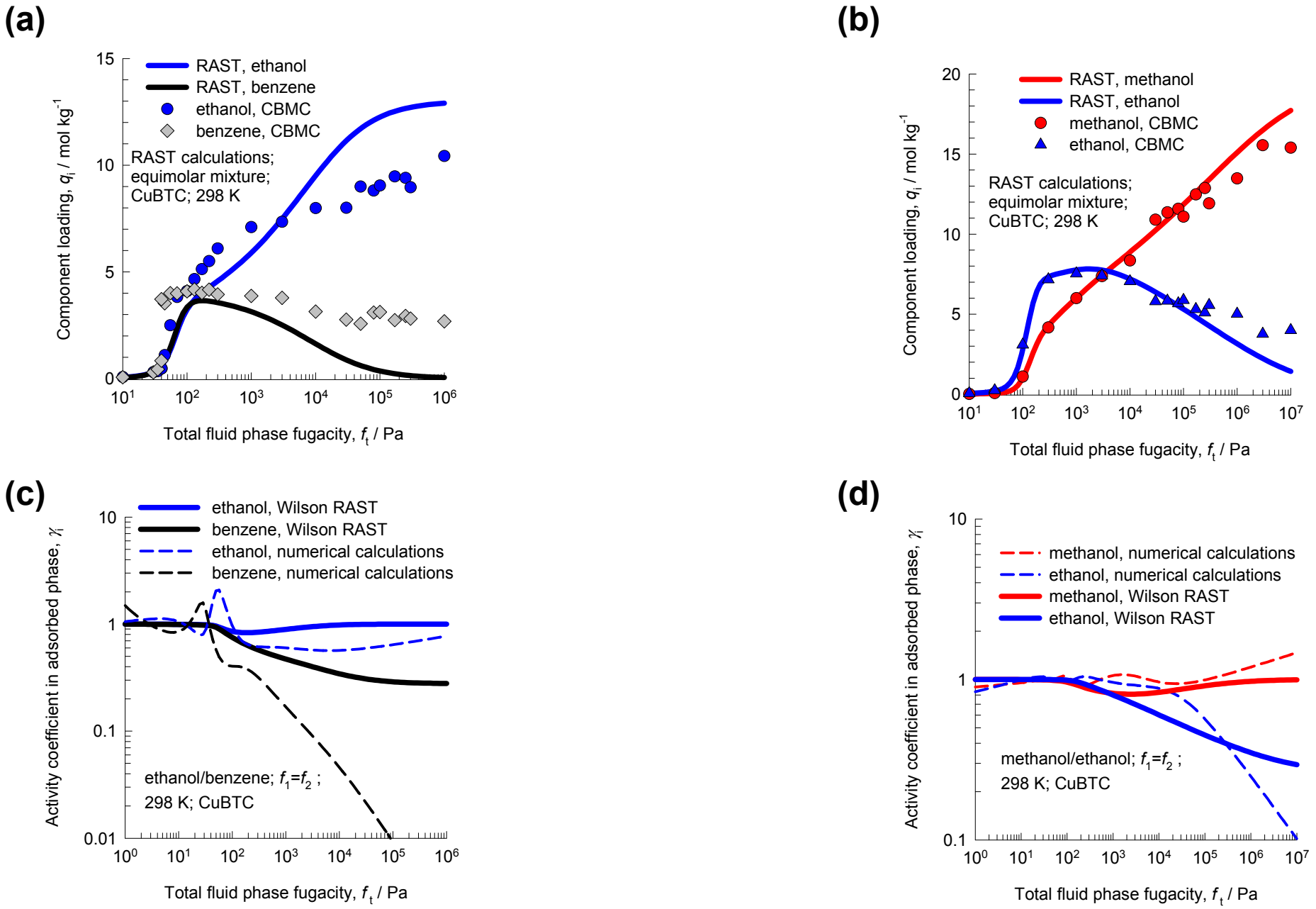

Water, methanol, ethanol unary isotherms in FAU

Figure ESI 34

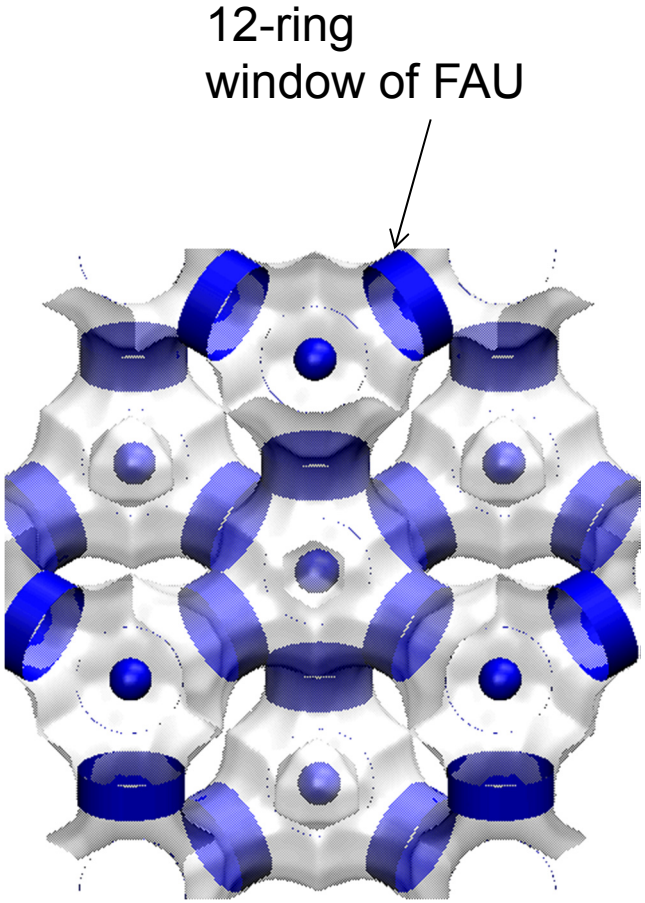

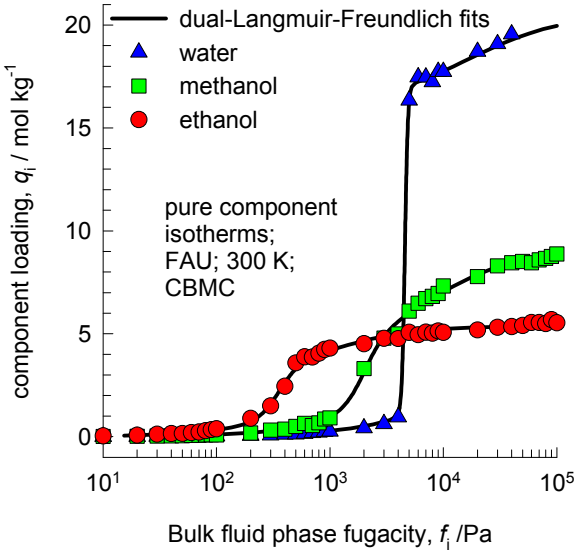

There are 8 cages per unit cell. The volume of one FAU cage is 786 Å^3, larger in size than that of CHA (316.4 Å^3) and DDR (278 Å^3).

Water/methanol mixture adsorption in FAU

Figure ESI 35

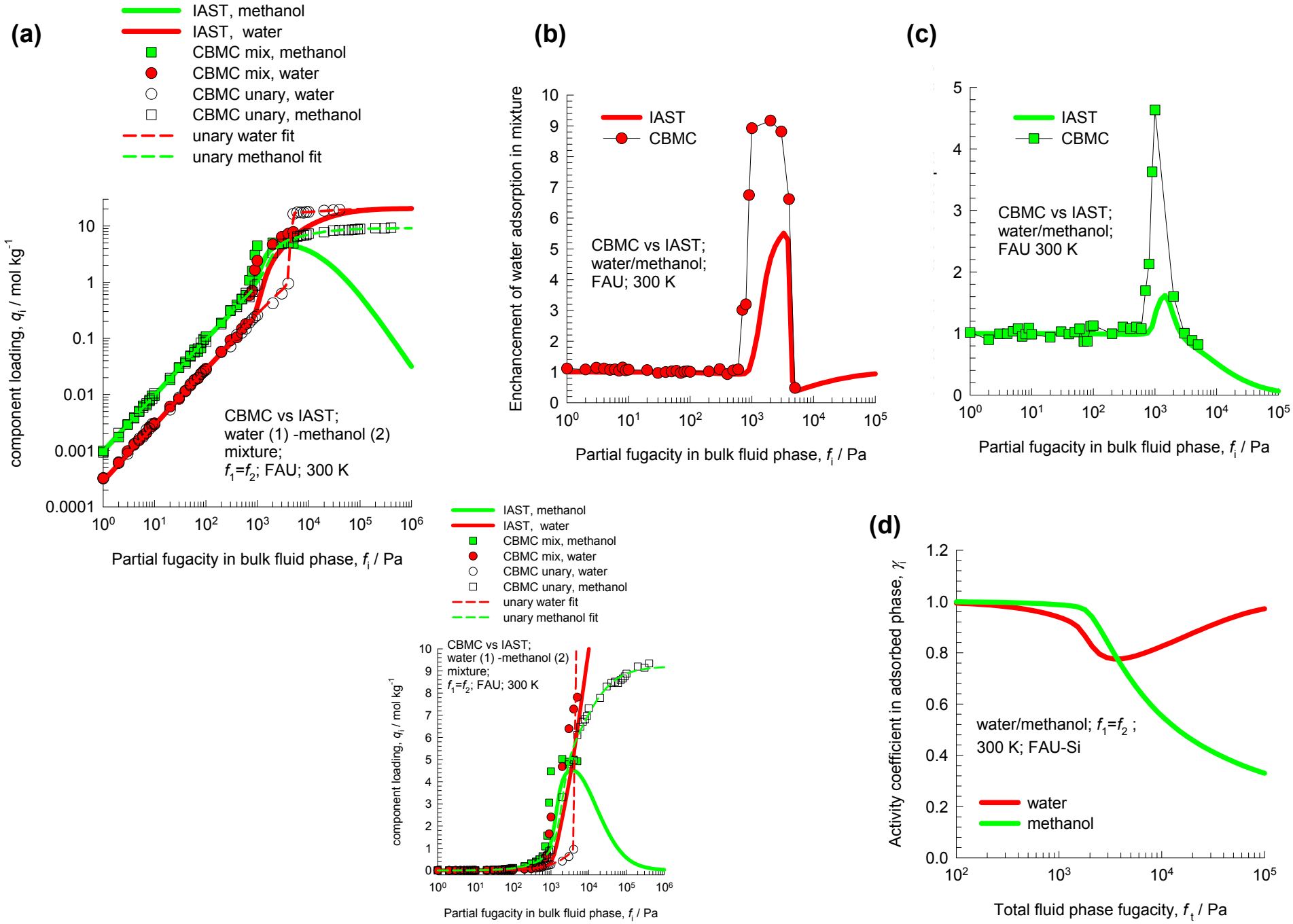

Water/methanol mixture adsorption in FAU

Figure ESI 36

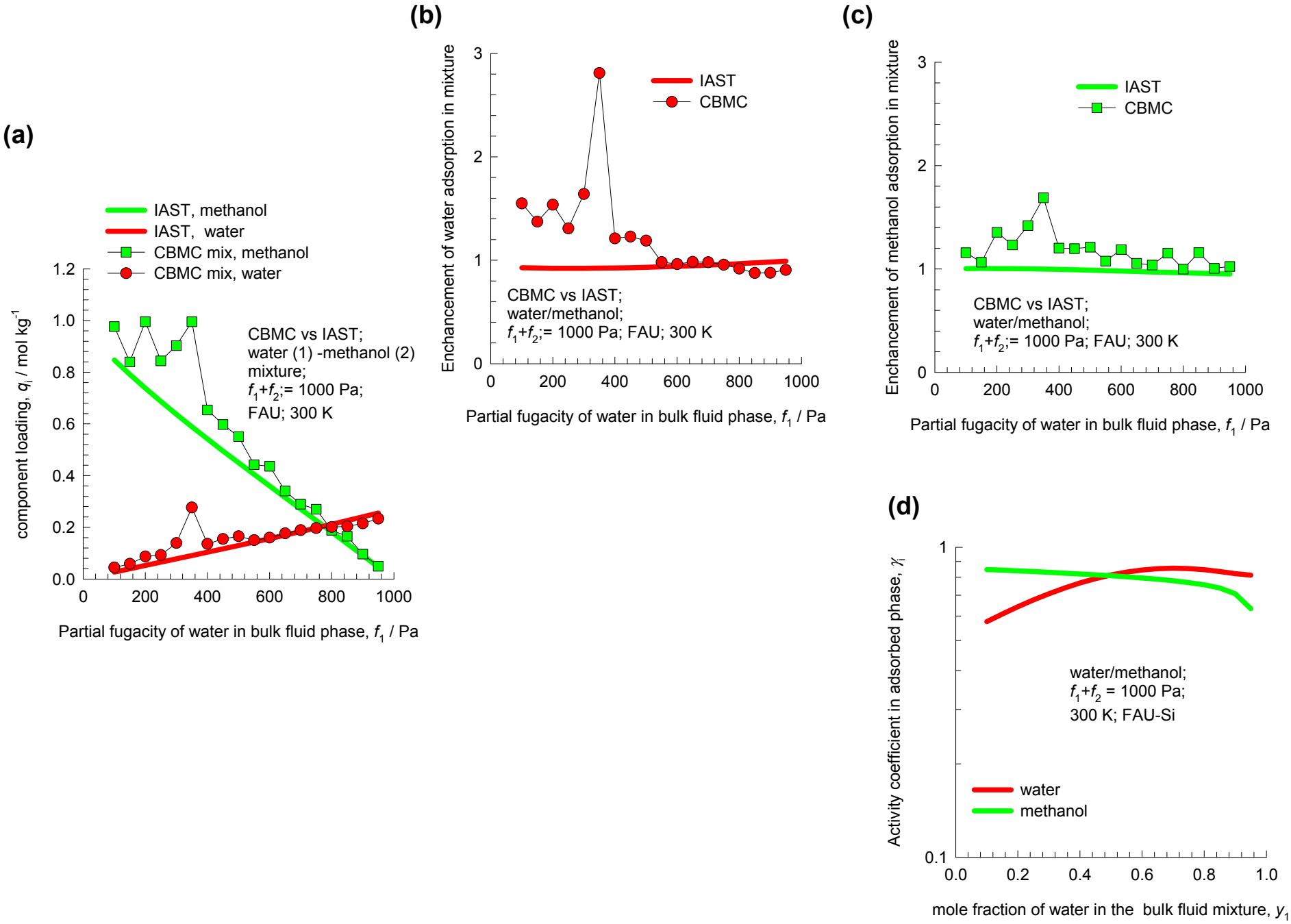

Water/ethanol mixture adsorption in FAU

Figure ESI 37

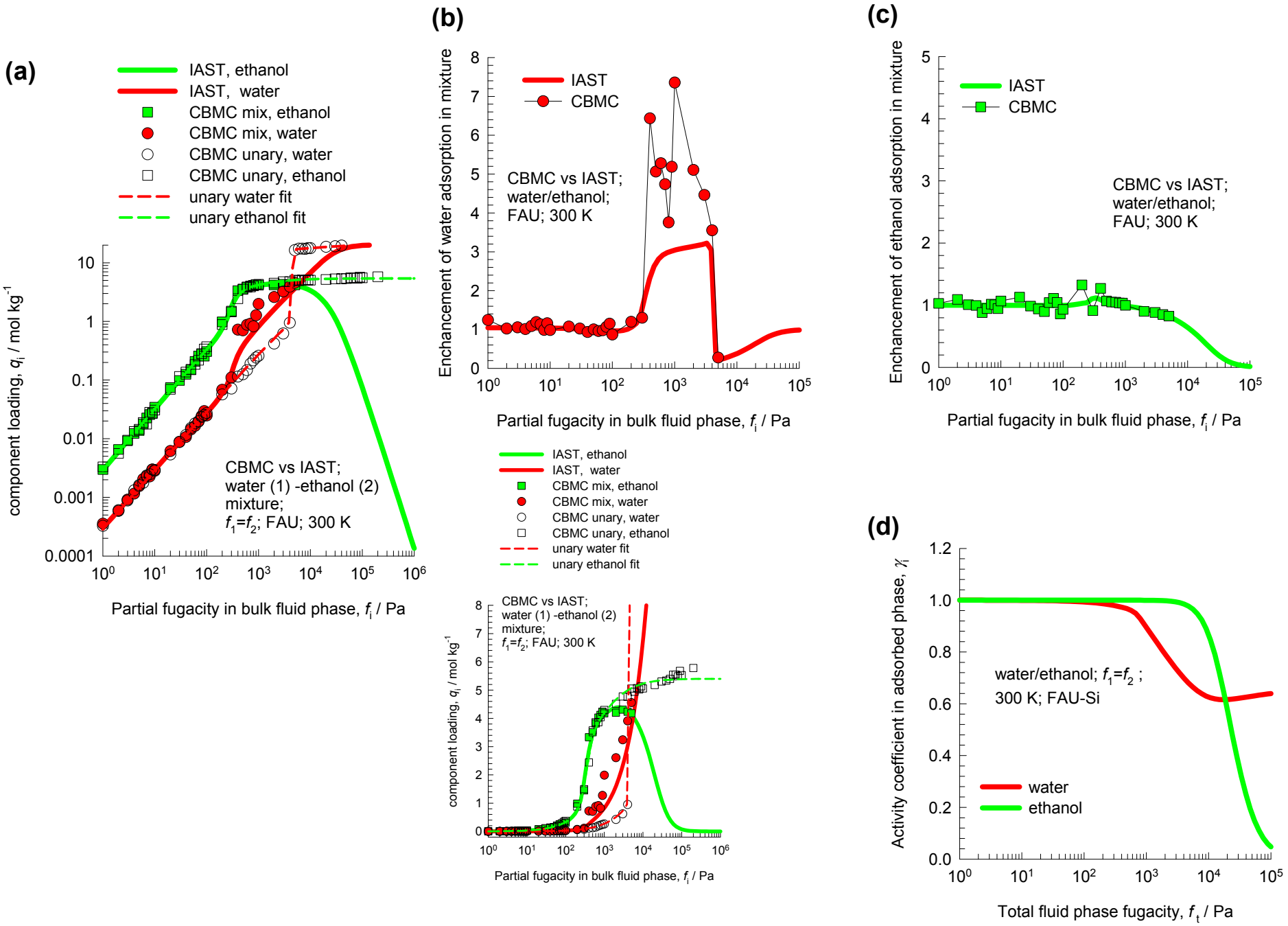

Water, methanol, ethanol unary isotherms in DDR

Figure ESI 38

There are 12 cages per unit cell. The volume of one DDR cage is 278 Å^3, significantly smaller than that of a single cage of FAU (786 Å^3), or ZIF-8 (1168 Å^3).

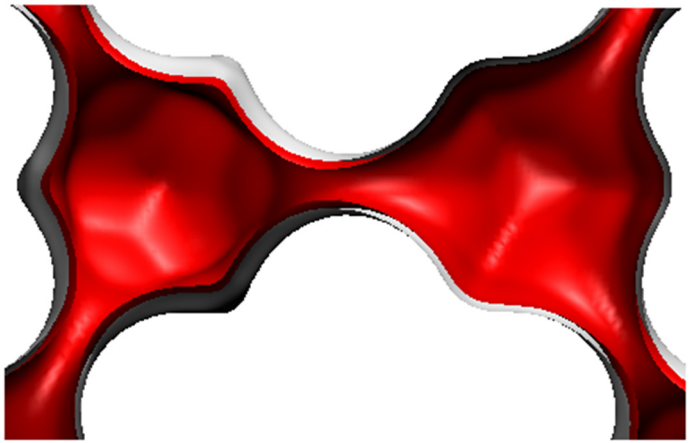

The volume of one DDR cage is 278 Å^3, significantly smaller than that of a single cage of FAU (786 Å^3), or ZIF-8 (1168 Å^3).

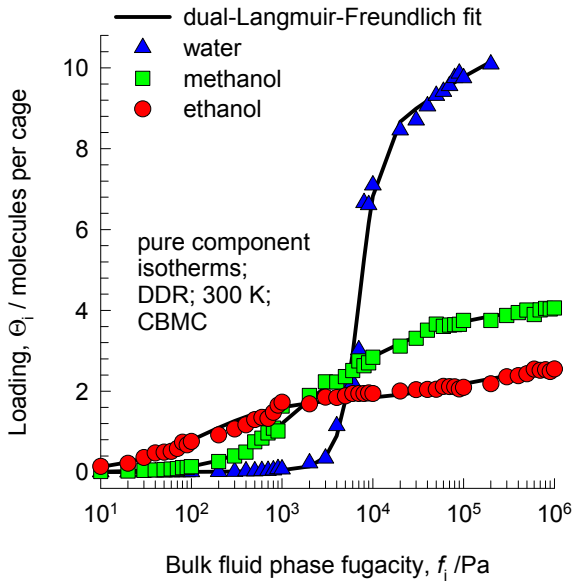

Water/methanol mixture adsorption in DDR

Figure ESI 39

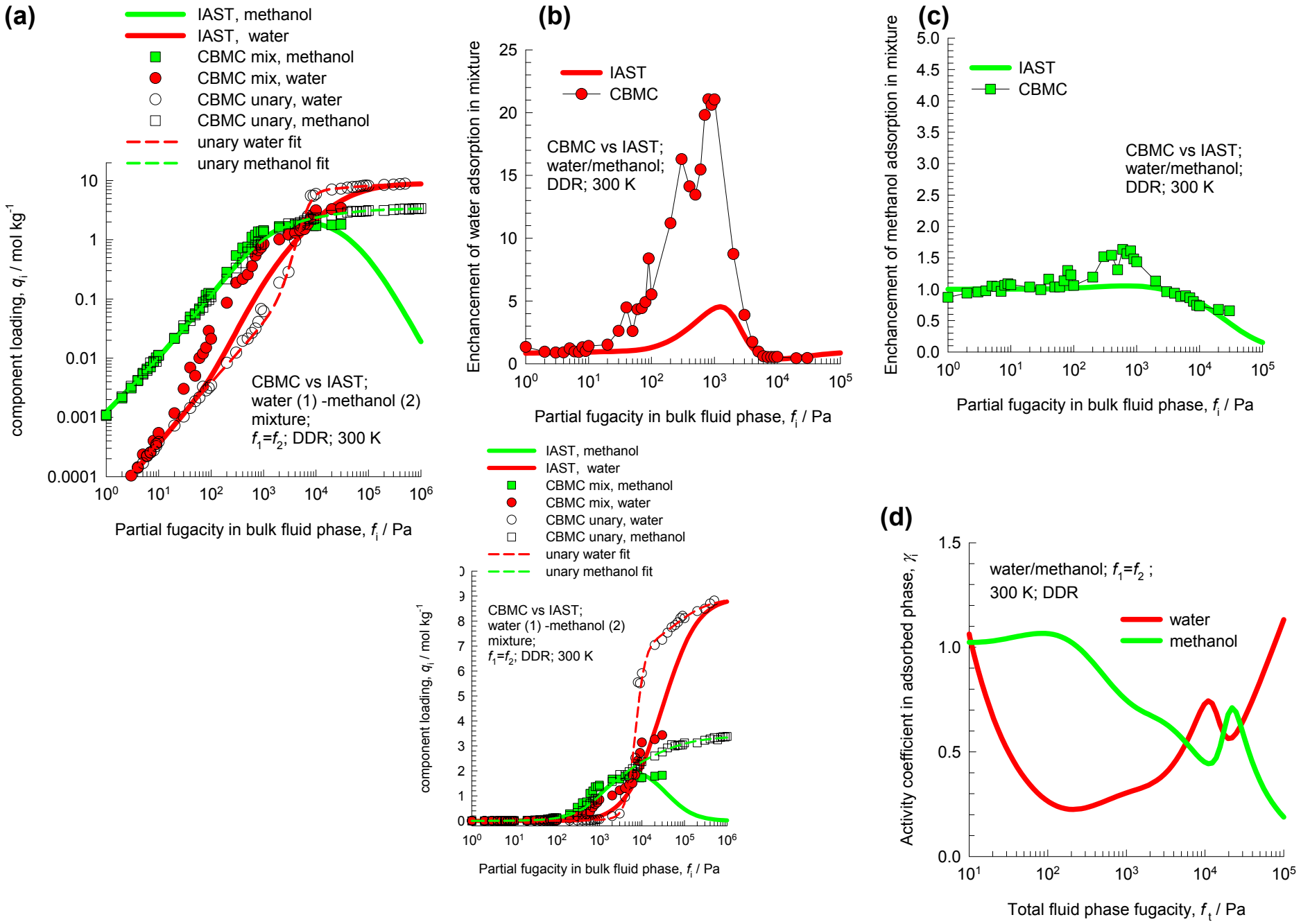

Water/ethanol mixture adsorption in DDR

Figure ESI 40

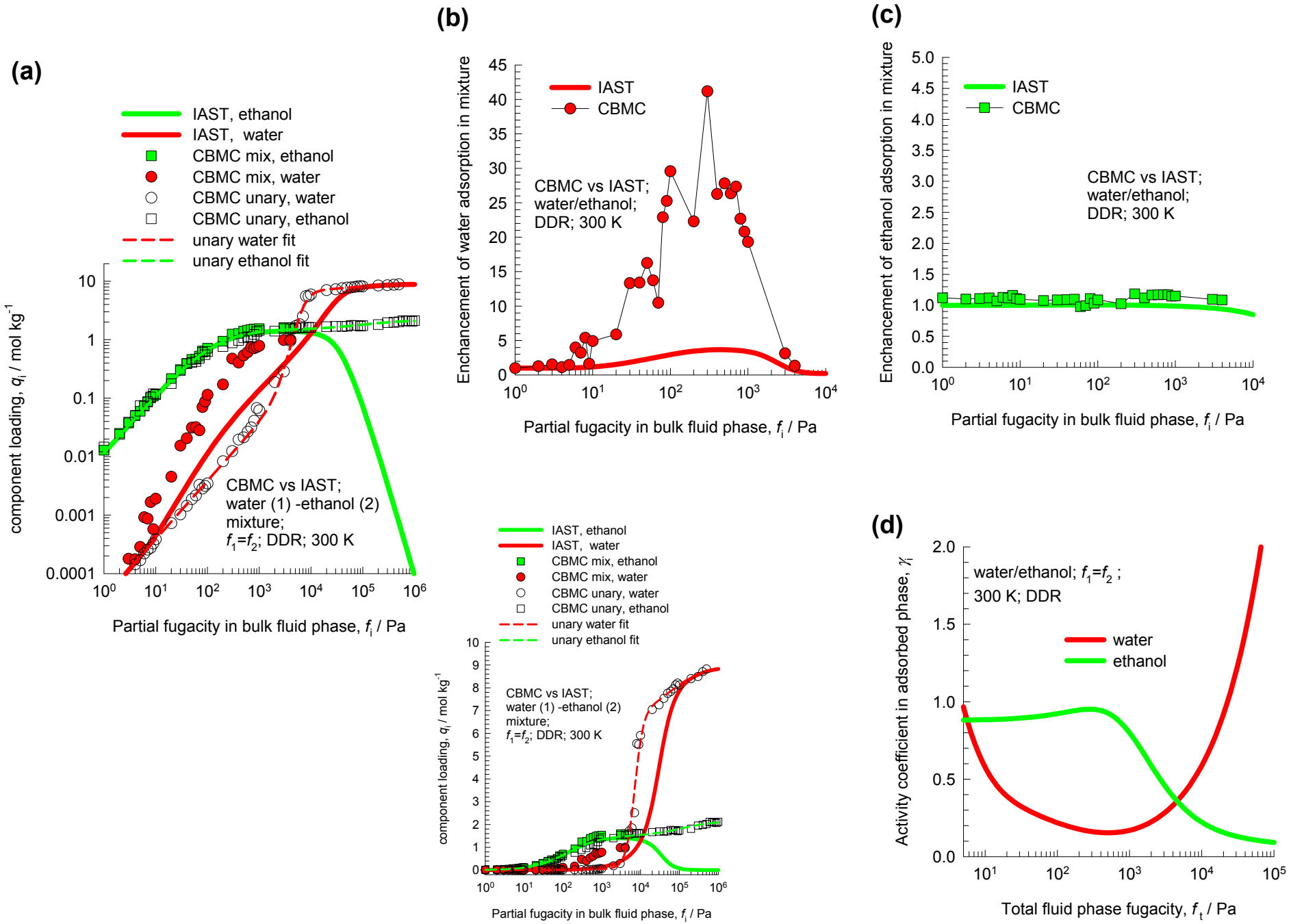

Water, methanol, ethanol isotherms in MFI

Figure ESI 41

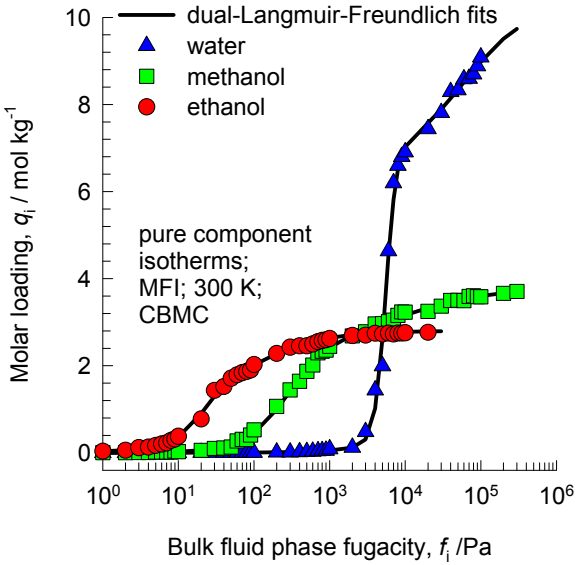

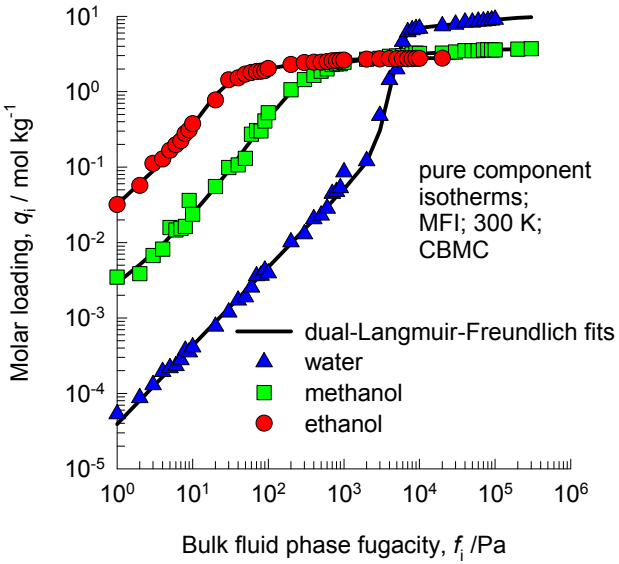

water

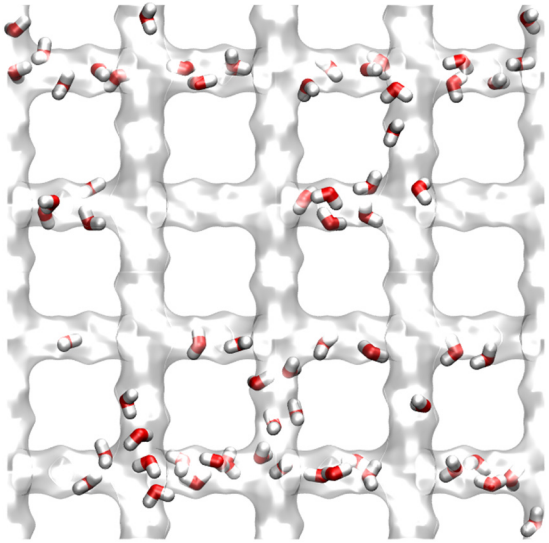

methanol

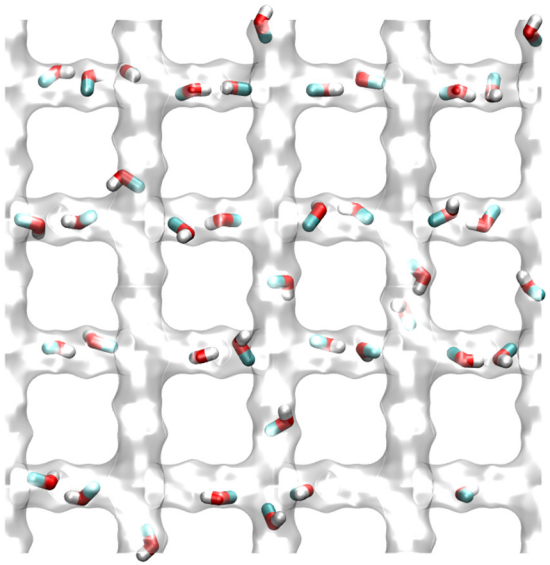

ethanol

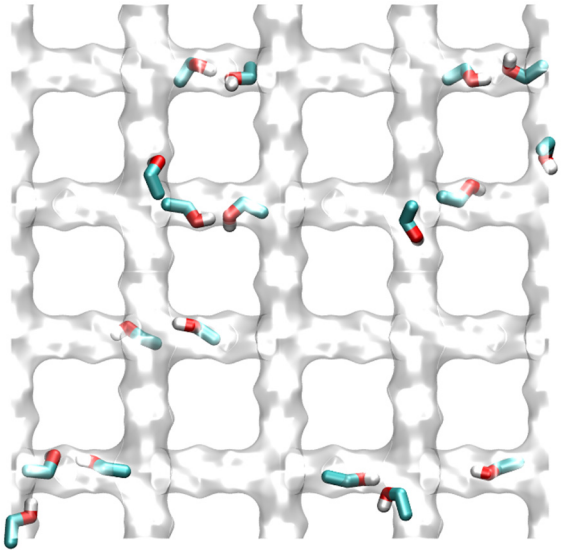

Water/methanol mixture adsorption in MFI

Figure ESI 42

(a)

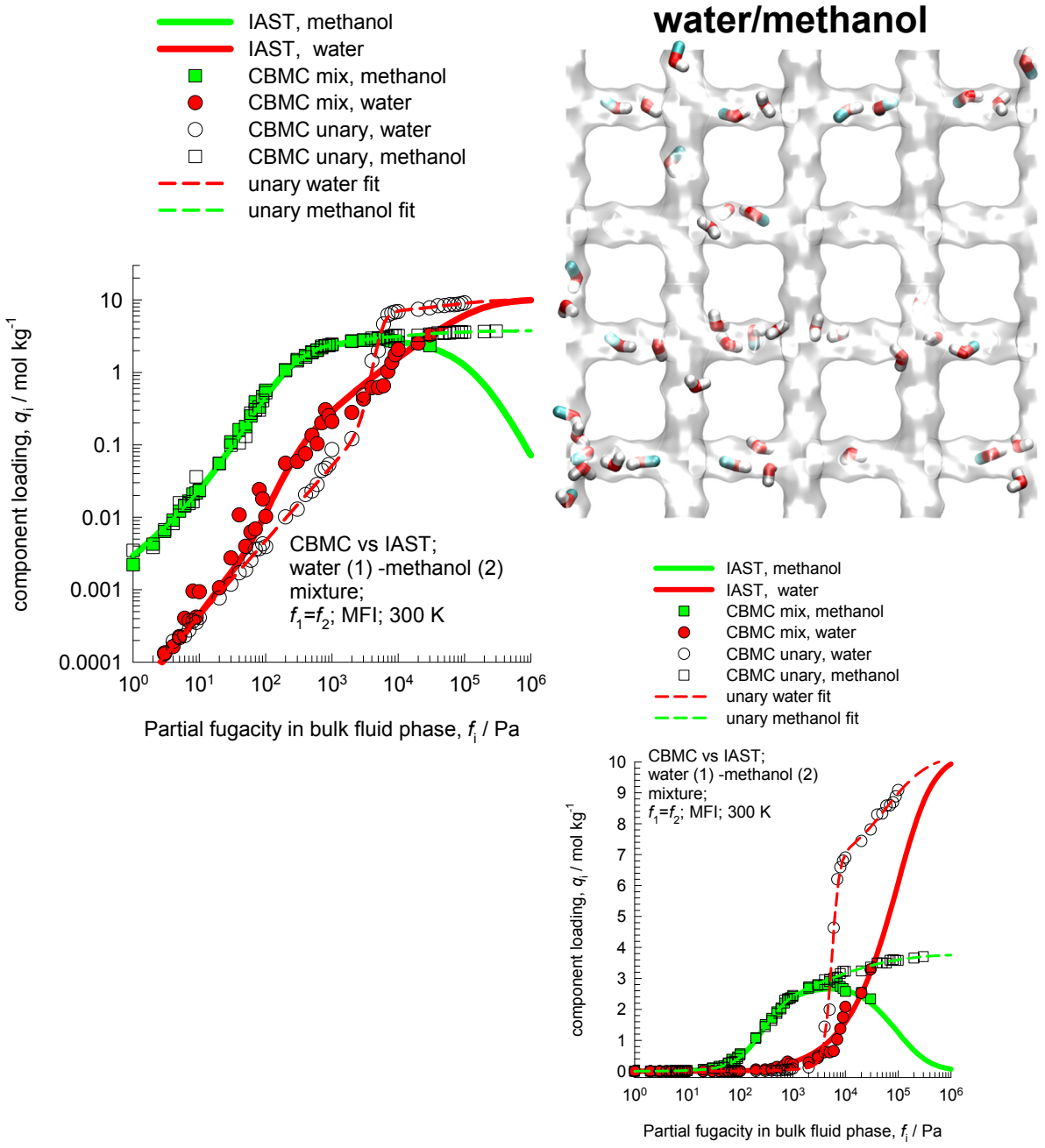

(b)

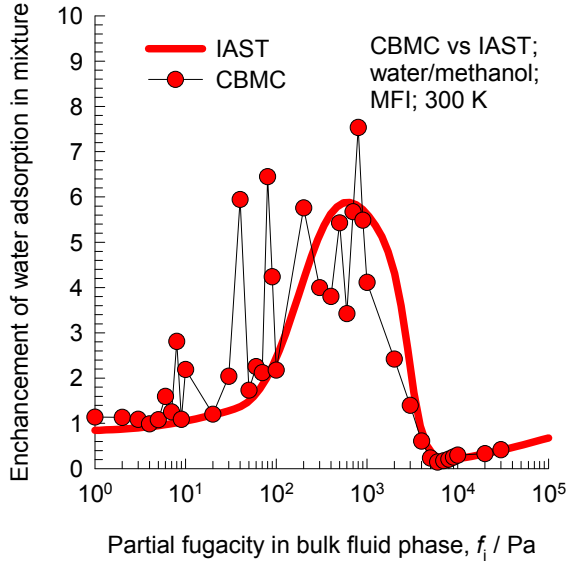

(c)

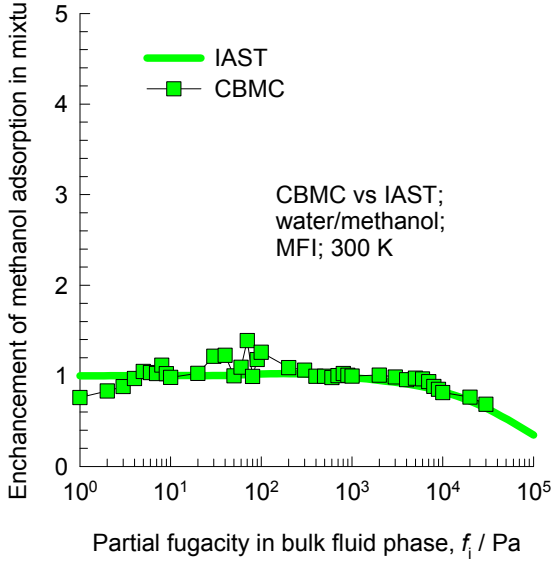

Water/ethanol mixture adsorption in MFI

Figure ESI 43

(a)

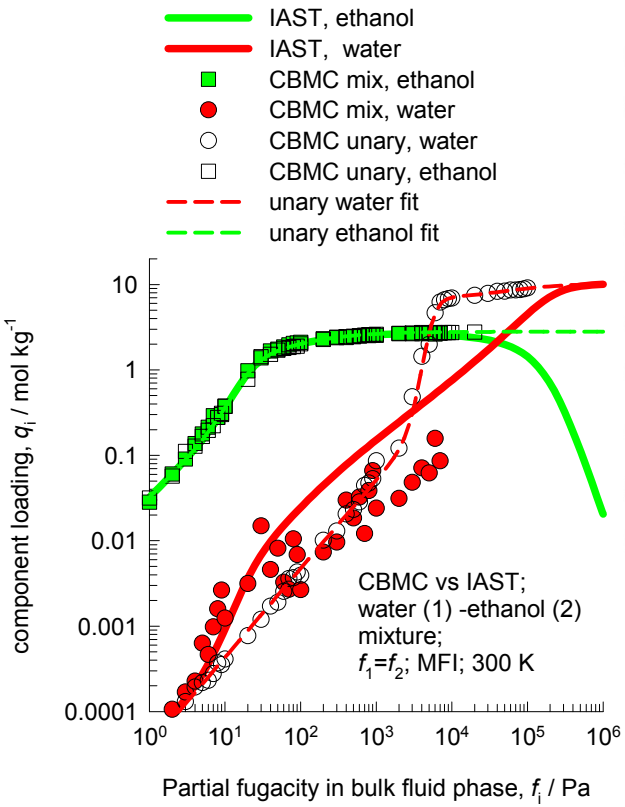

water/ethanol

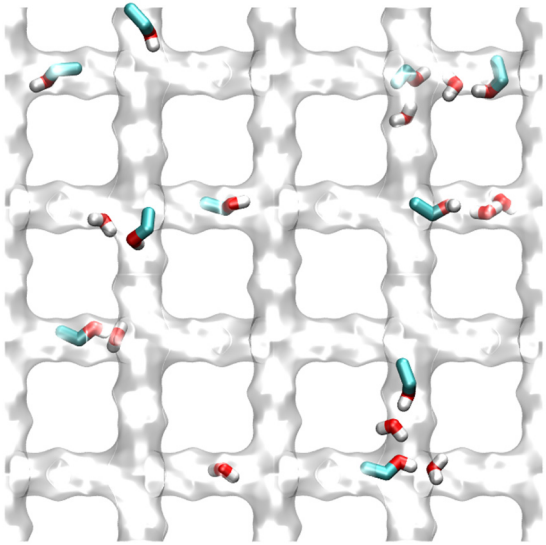

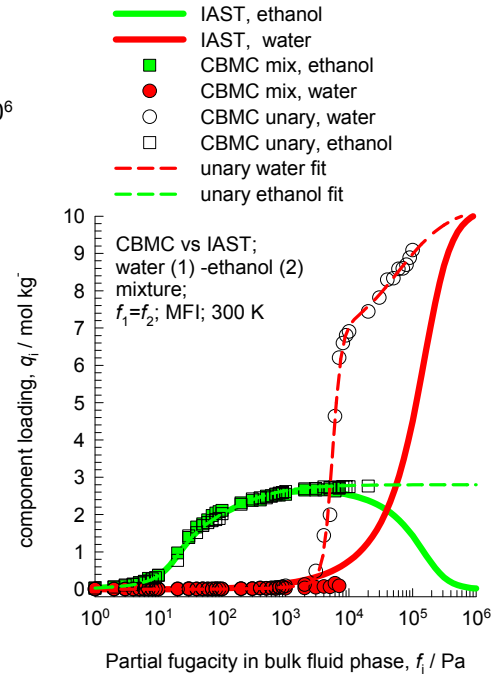

(b)

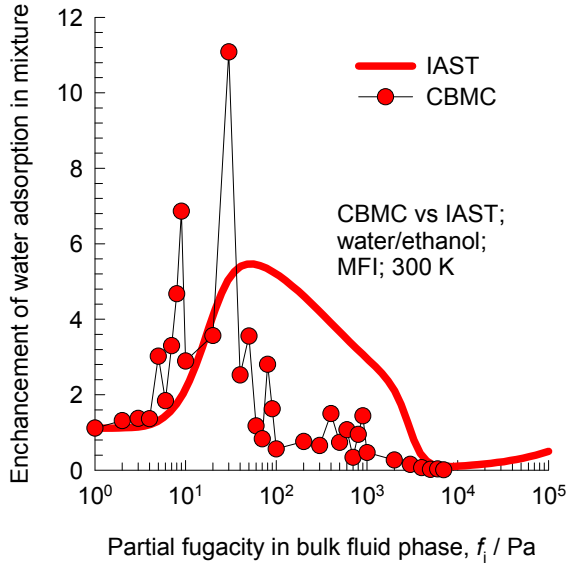

(c)

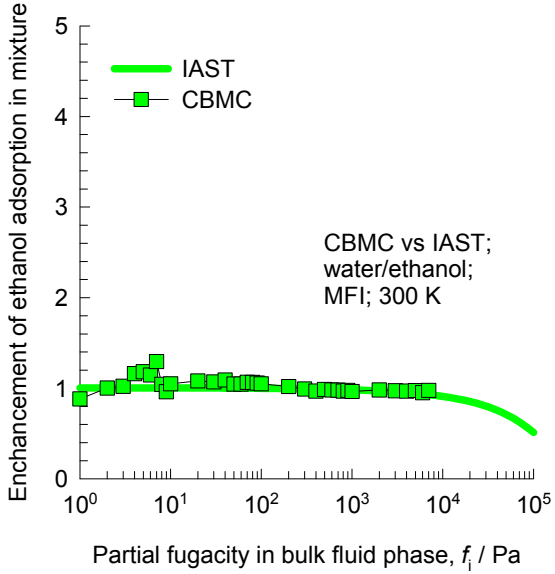

Water/butanol mixture adsorption in MFI; expt data of Farzaneh

Figure ESI 44

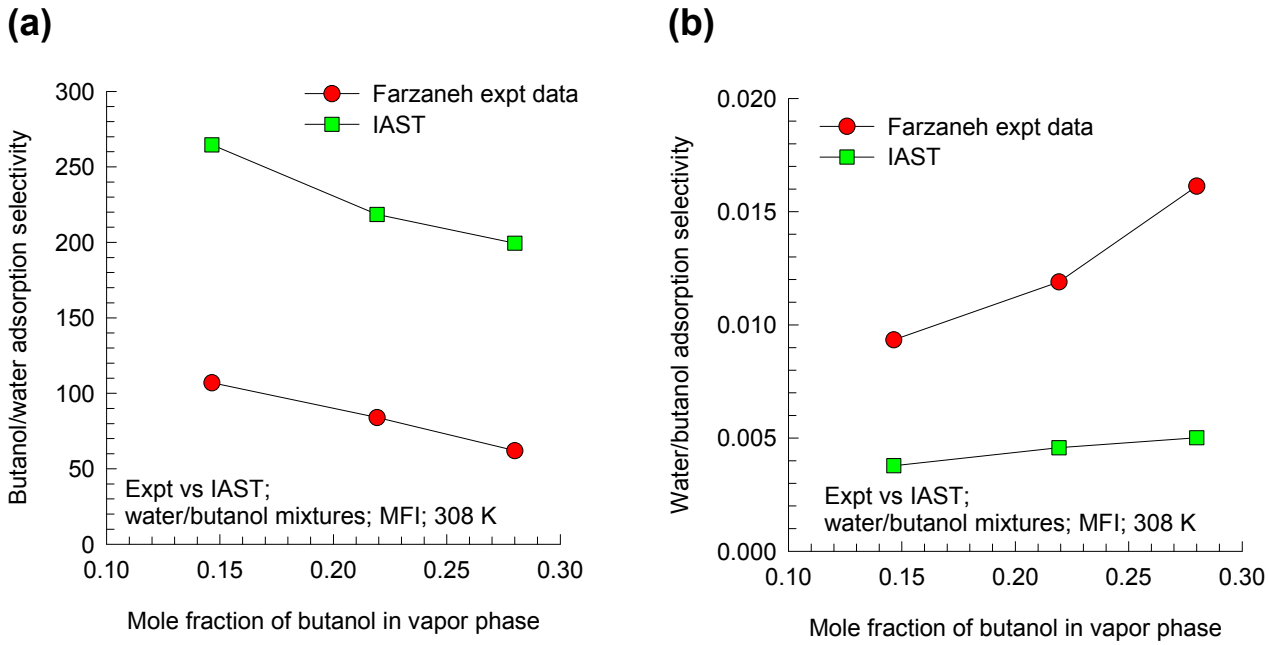

1-alcohols unary isotherms in CHA zeolite

Figure ESI 45

There are 6 cages per unit cell.
The volume of one CHA cage is 316.4 Å^3, slightly larger than that of a single cage of DDR (278 Å^3), but significantly lower than FAU (786 Å^3).

(a)

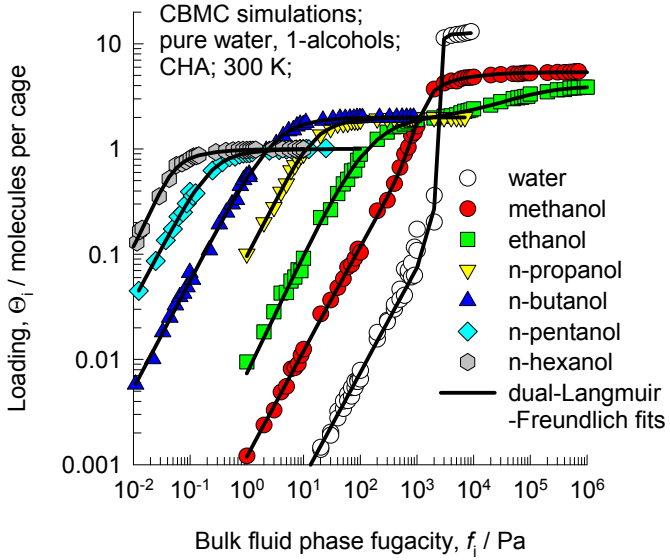

(b)

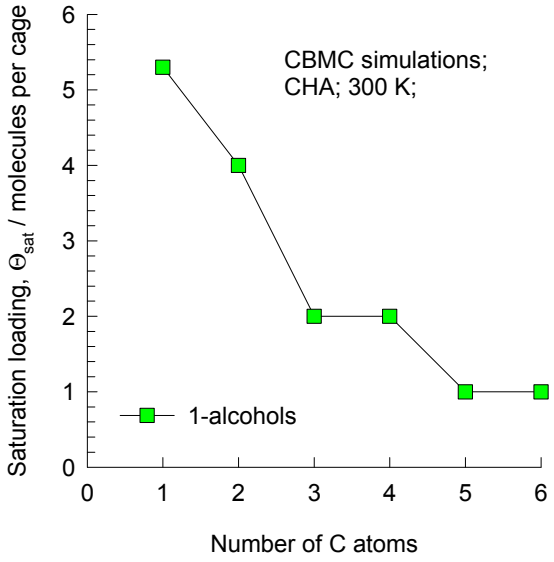

(c)

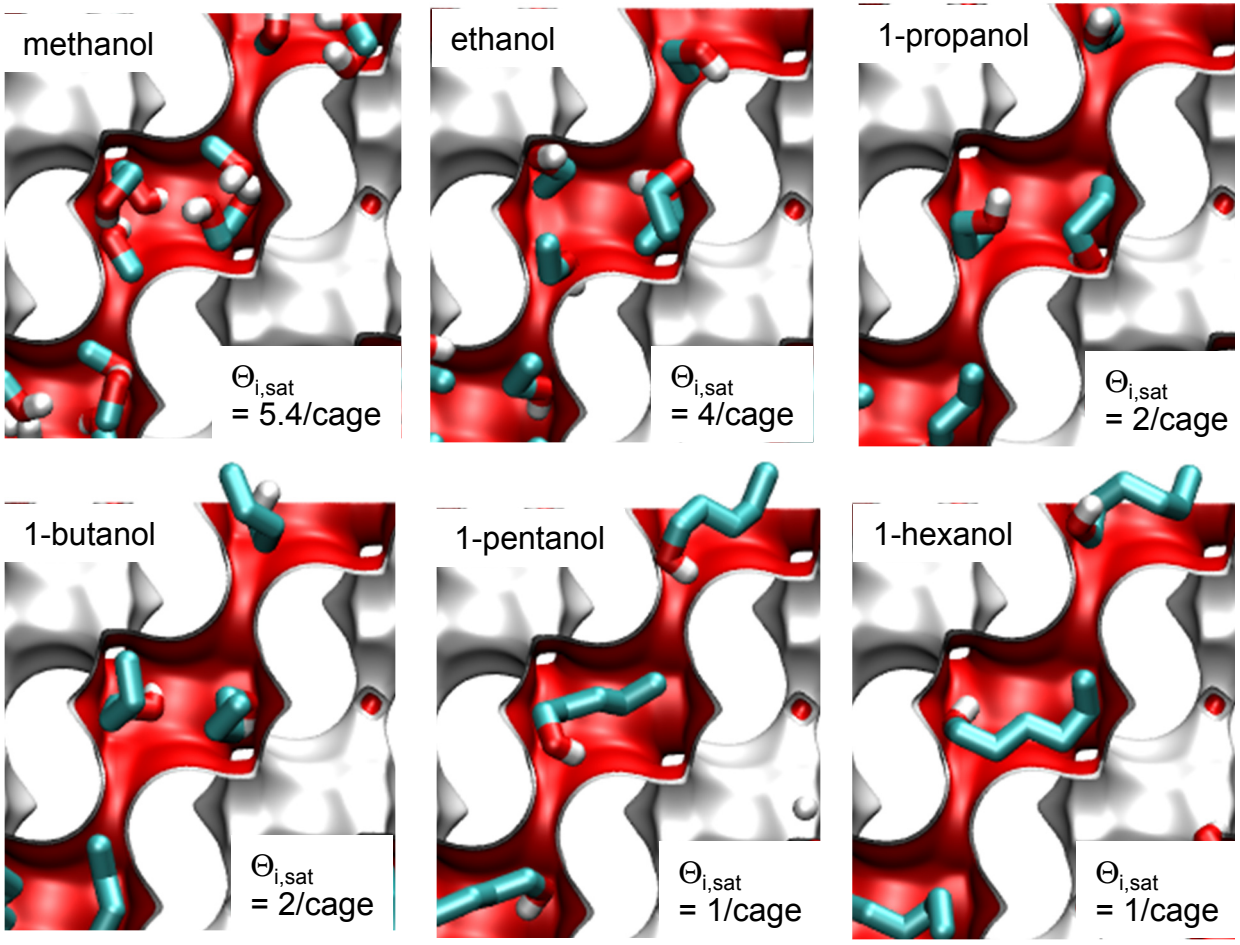

1-alcohols mixture adsorption in CHA zeolite

Figure ESI 46

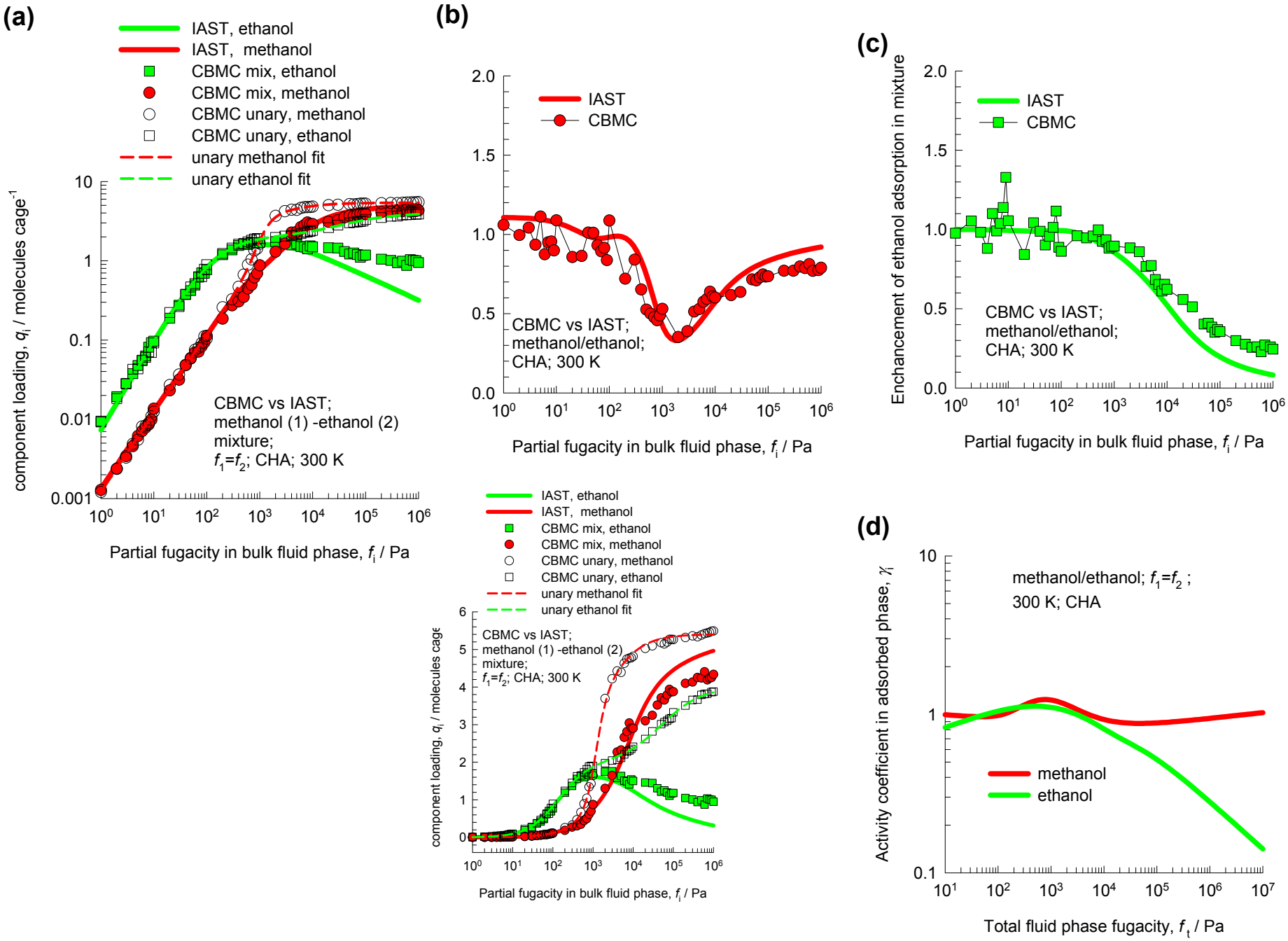

1-alcohols mixture adsorption in CHA zeolite

Figure ESI 47

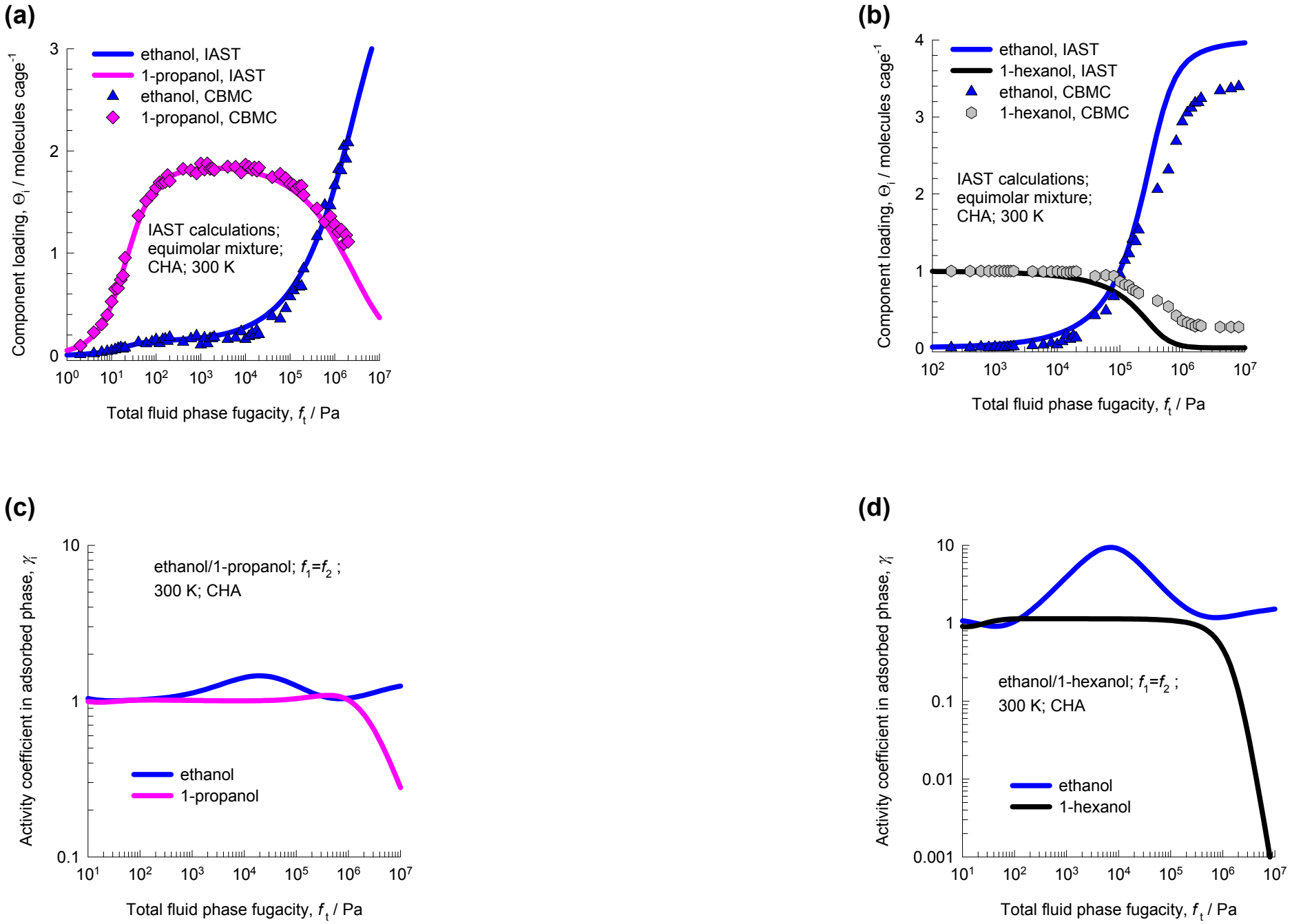

Figure ESI 48

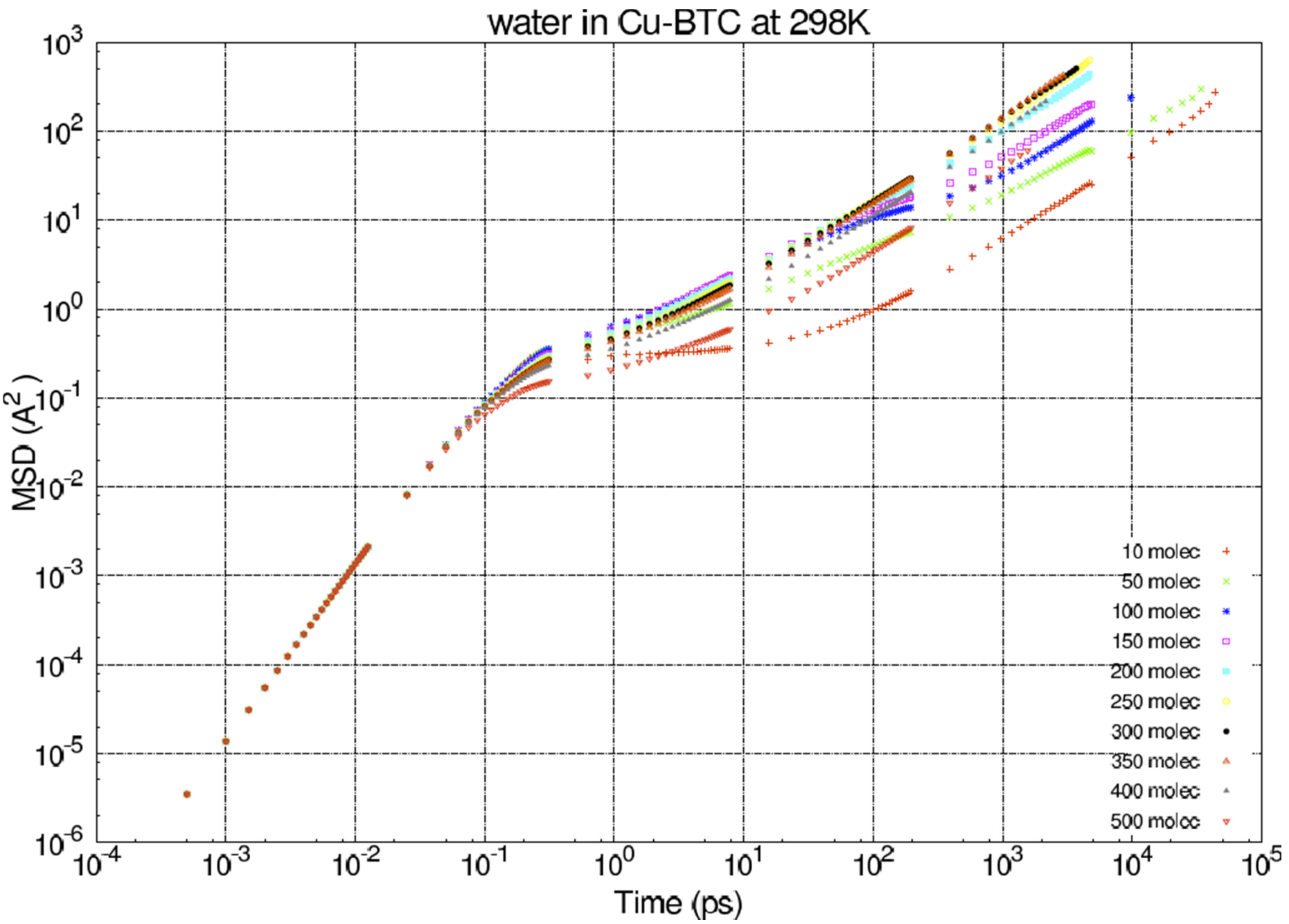

Figure ESI 49

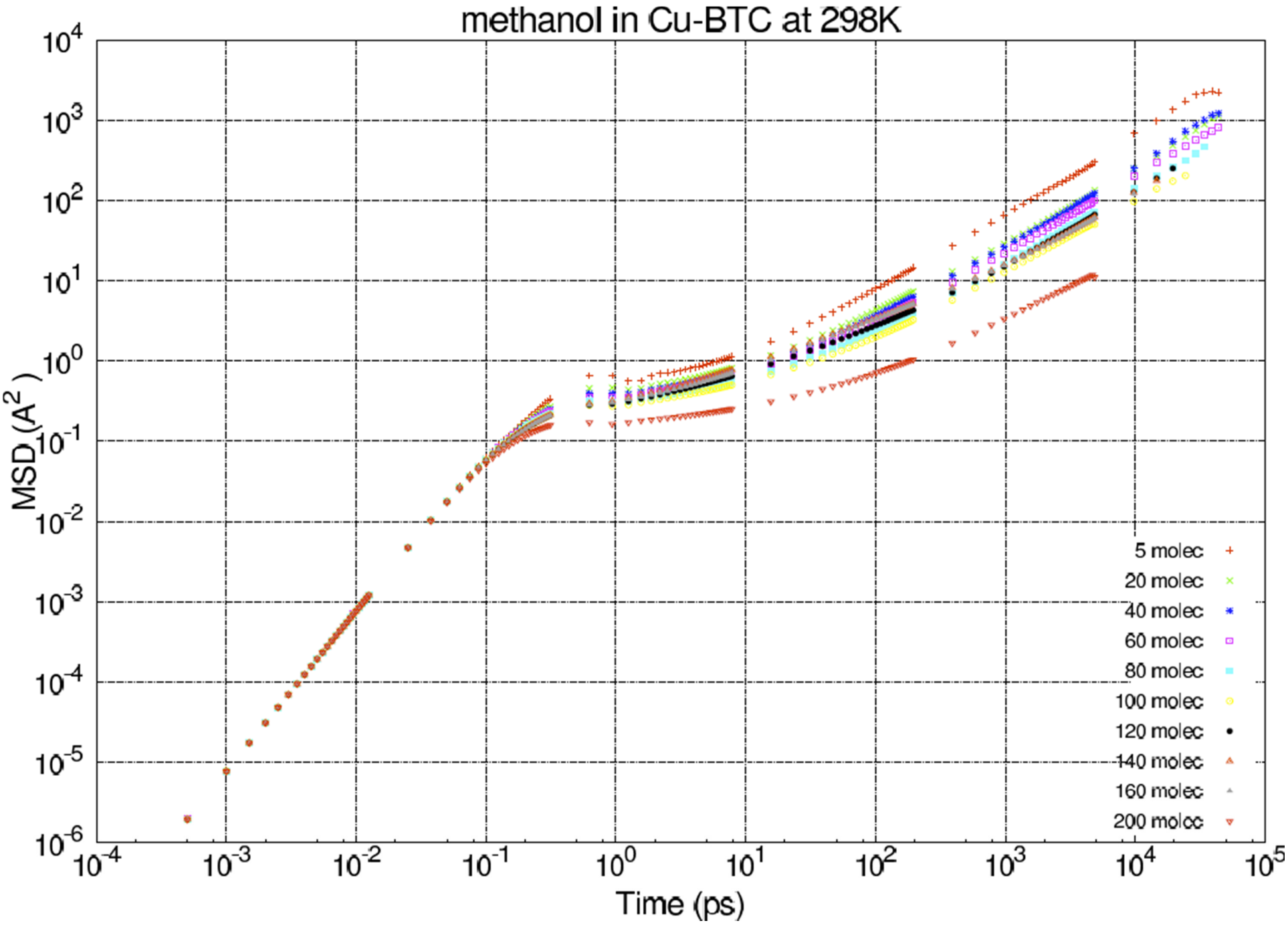

Figure ESI 50

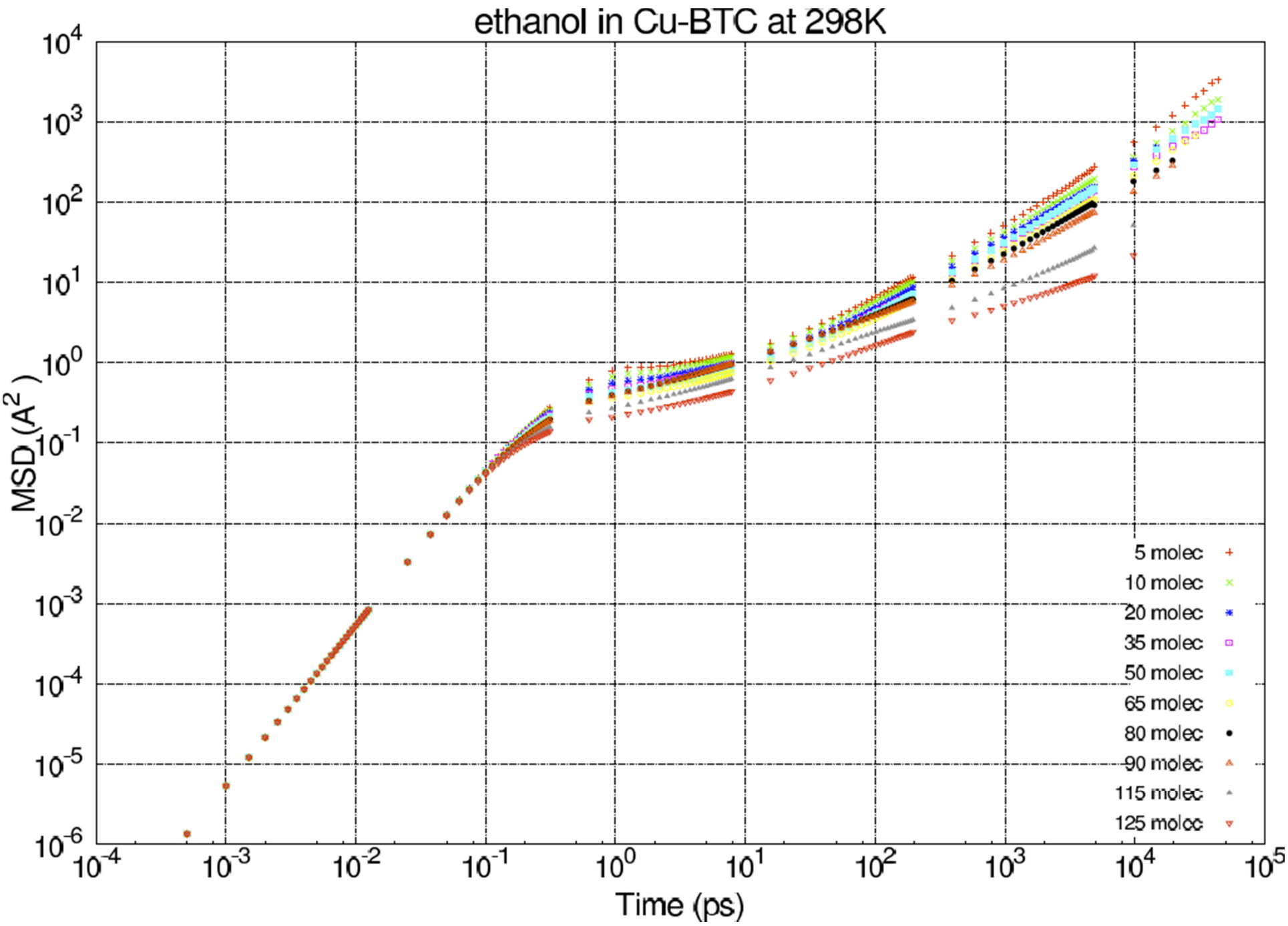

Figure ESI 51

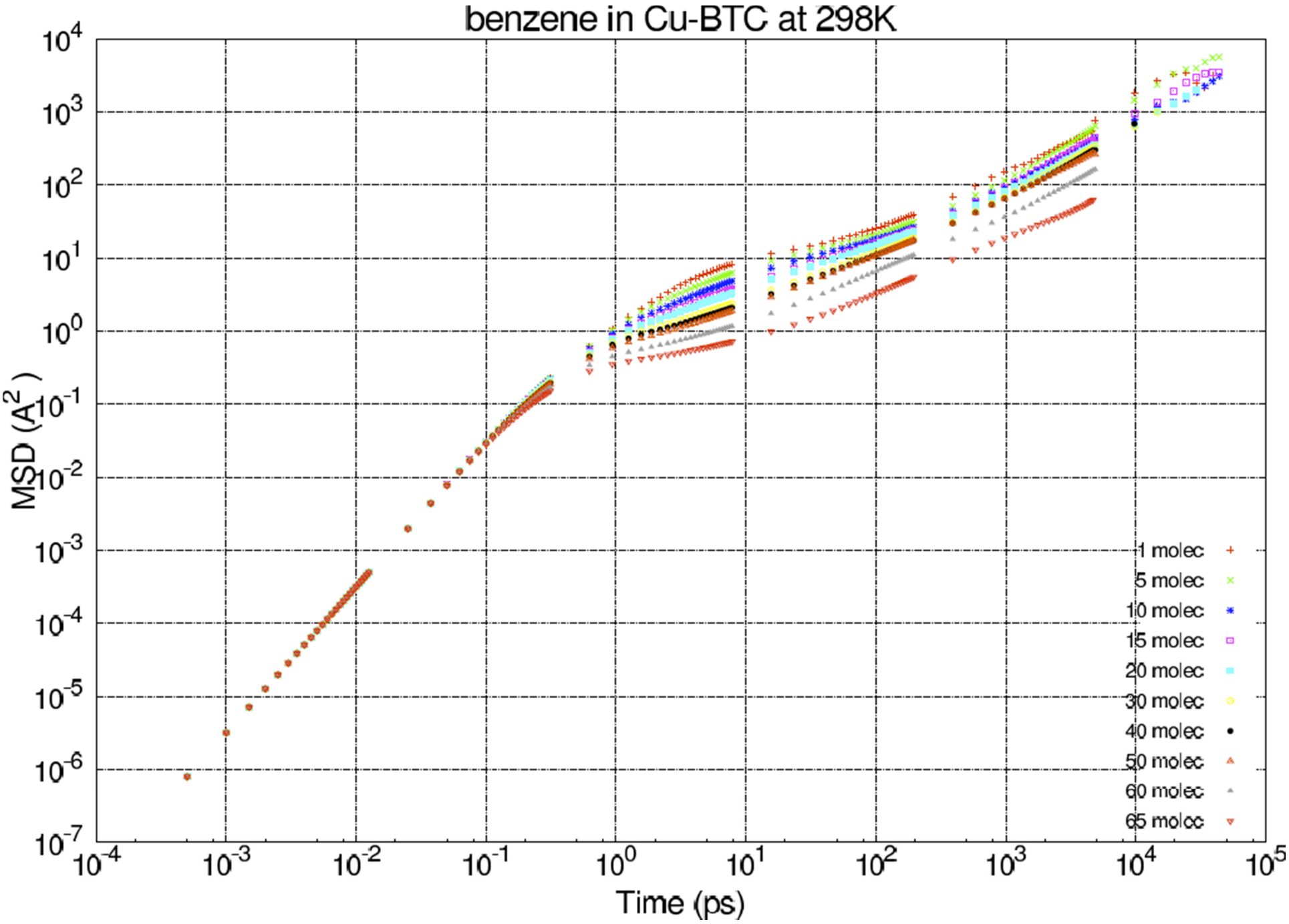

Figure ESI 52

$D_{i,self}$ vs q_i ; $D_{i,self}$ vs θ_i

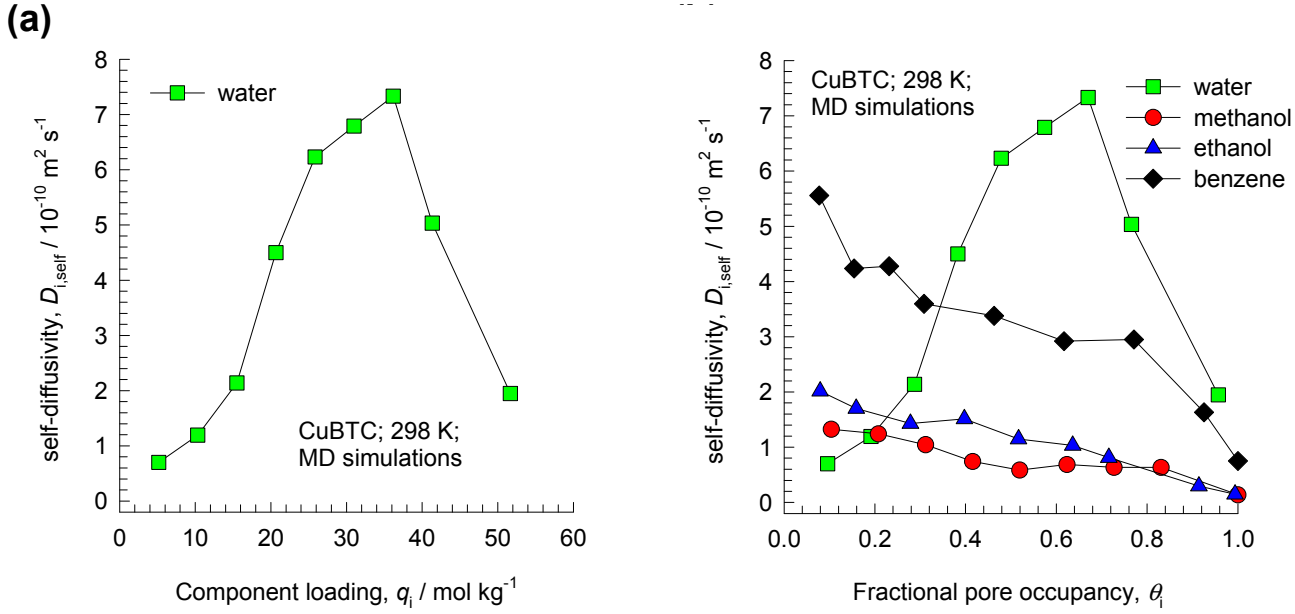

Figure ESI 53

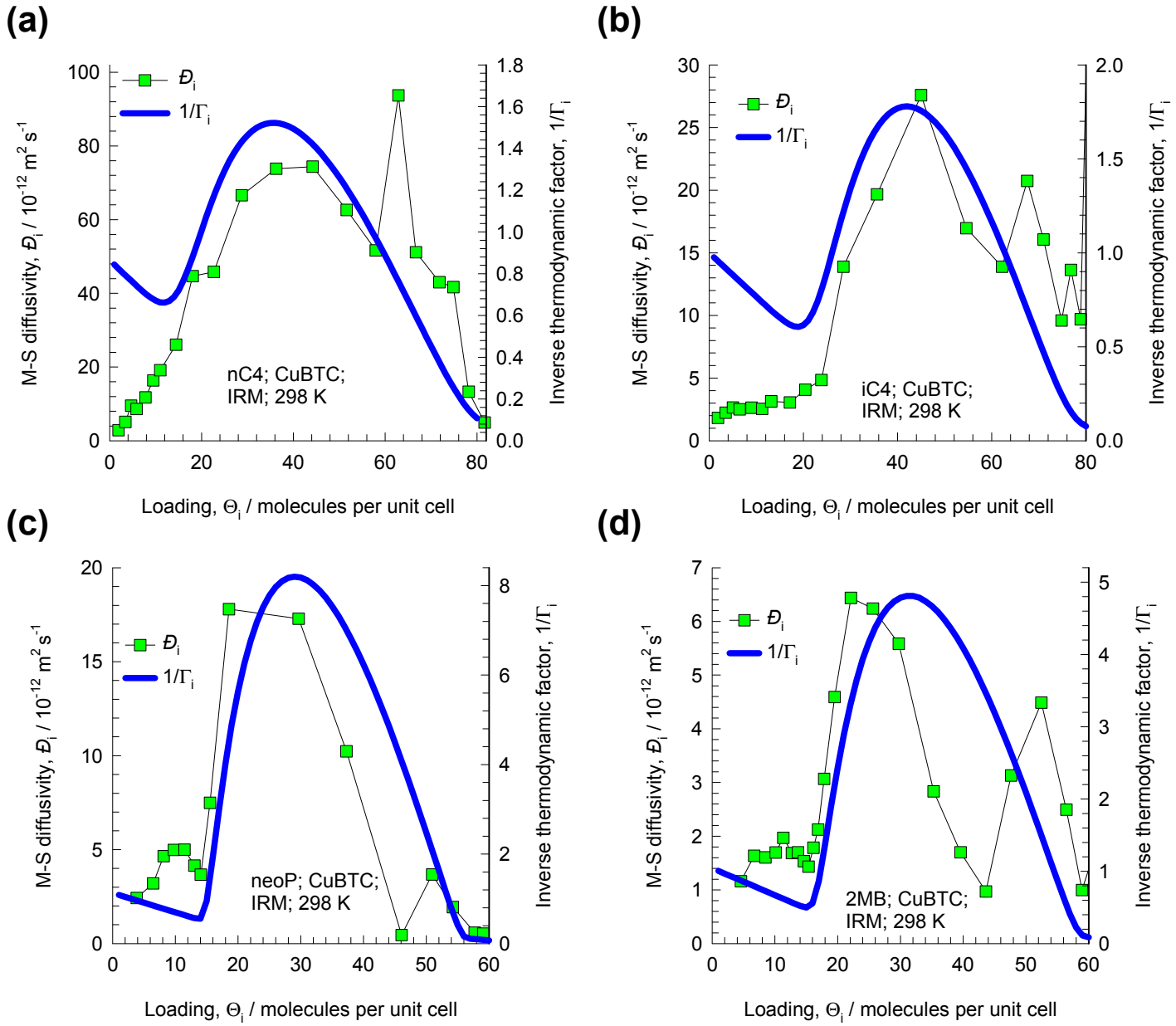

Figure ESI 54

(a)

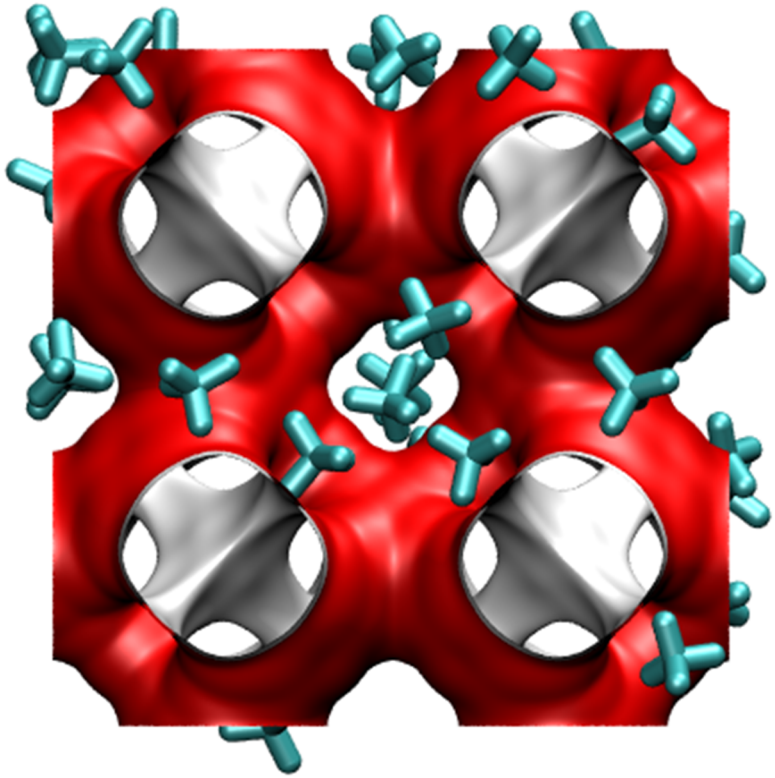

(b)

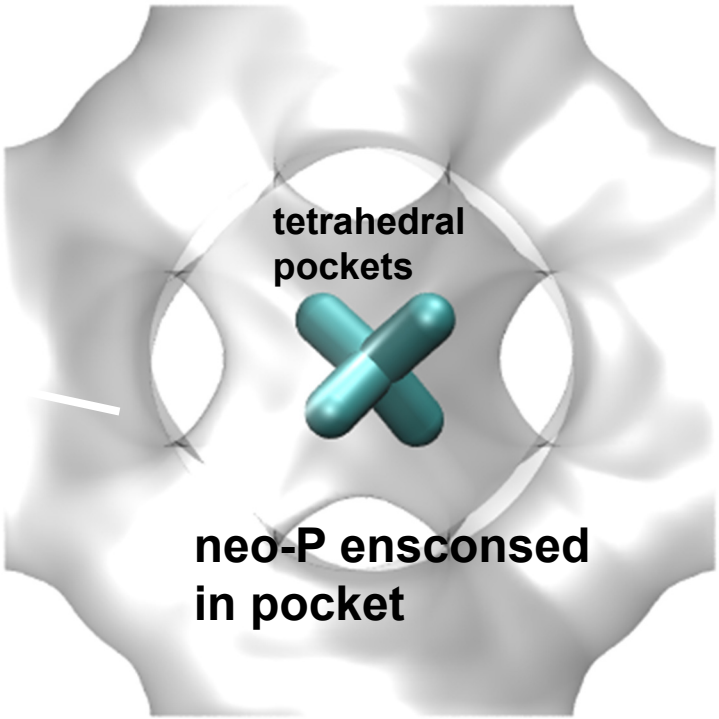

Figure ESI 55

$D_{i,self}$ vs q_i versus $1/\Gamma_i$ vs q_i

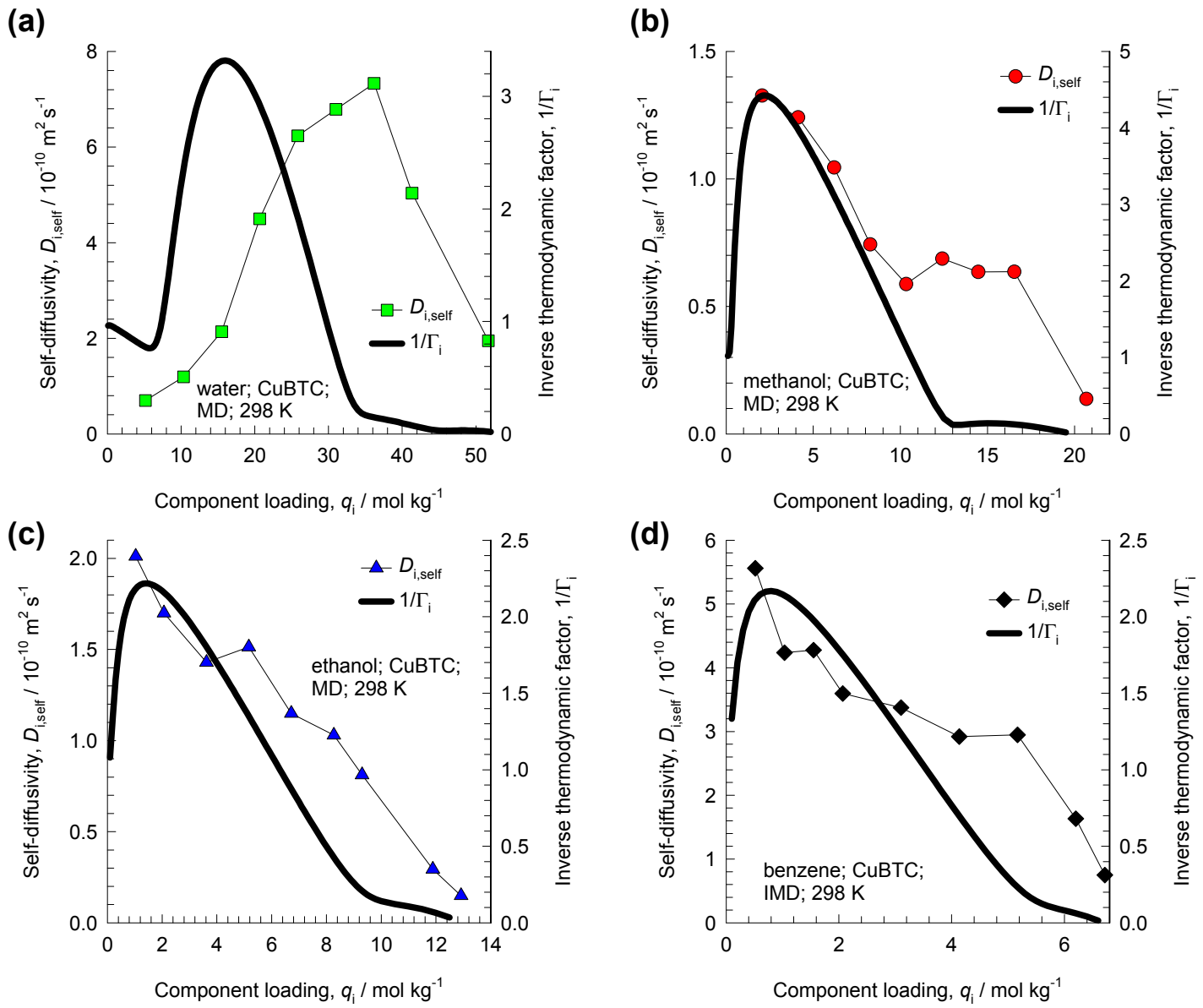

Figure ESI 56

$D_{i,self}$ vs θ_i versus $1/\Gamma_i$ vs θ_i

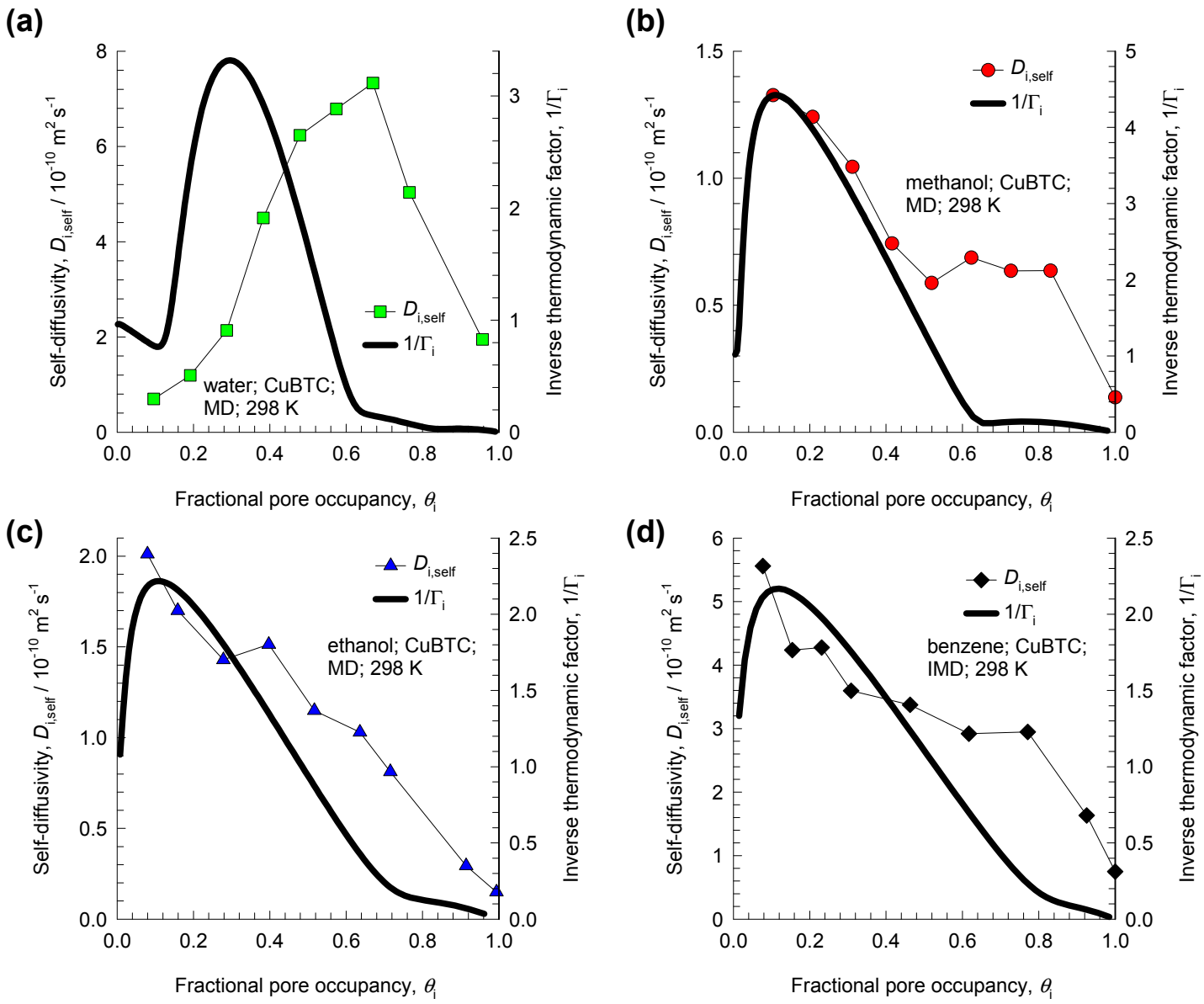

Figure ESI 57

Transient Desorption of Methanol